Manganese Enrichments in Matthews Ridge, Guyana

Master Thesis Project, Earth Life and Climate Master's Program.

Supervisor: Dr.Paul Mason, Stacey Amattaram MSc

Yiannis Maris (9890181)
UTRERCHT UNIVERSITY

Acknowledgments

For this Master's thesis, I would like to thank my friends and family for their continuous and positive support throughout the project. Special thanks to Harilaos Tsikos for his valuable help, feedback during the interpretation of results, and advice throughout the project. Also special thanks to Salomon Kroonenberg for his feedback and his valuable advice and ideas. Lastly and most of all, I would like to thank the two supervisors of this project. Dr. Paul Mason and Stacey Amattaram, MSc., from Utrecht University for their valuable help, guidance, and meaningful cooperation.

Abstract

The Matthews Ridge manganese Mineralisation is part of the Barama Mazaruni Trans-Amazonian Greenschist Belt in the Guyana Shield, northern South America. The Matthews Ridge Formation is composed of two major units. The lower unit is made up of mafic volcanic and metavolcanic rocks and the upper rock unit consists of clastic metasediments and intermediate metavolcanics that are intercalated with chemical sediments. The deposit was accumulated in the Early Proterozoic when the ocean and atmosphere had a substantial amount of oxygen, up to 10% of present-day levels. Manganese was deposited at this time in significant amounts. in contrast to the Archean where Fe deposition dominated. The Fe redox cycle has been studied extensively throughout Earth's history while the Mn redox cycle has received less attention. Little is known about the processes that led to Mn enrichment in the Matthews Ridge Formation and most of the knowledge about the mineralization comes from an unpublished mining report. In contrast to this mineralization, other Mn deposits of similar, Early Proterozoic age have been studied thoroughly, e.g. Nsuta (West Africa) and Serra do Navio Brazil. These deposits are places where Fe-rich minerals are found in minimal proportions and as secondary minerals, thus making it a unique location to study the Mn redox behaviour and deposition mechanisms. For this study, the major oxide and REE components of the sediments were explored using XRF and ICP-MS data and focusing on the similar redox properties of Manganese and Cerium to identify the conditions under which the sediments were accumulated. By combining the data with petrographic observations and Micro Probe data the Mathews Ridge sediments were deposited in a shallow marine environment under oxidative conditions following the weathering of the mafic and ultramafic rocks. The sediments were later metamorphosed to greenschist facies and subjugated to tectonic overprinting and tropical weathering resulting in lateritism.

Table of Contents

1 Introduction

1.1 Mn Geochemical behaviour in the Marine Environment and Mineralization types.

In the marine environment, manganese enrichments are typically supplied by either an endogenic hydrothermal source or related to exogenic processes that lead to concentration in coastal and continental areas (Roy,2006a). From observations in modern marine basins (e.g. Black Sea, Baltic Sea), coupled with thermodynamic calculations that mimic natural conditions, it has been proven that the main factor that drives the Mn deposition is Eh-ph variations in the inorganic aqueous system (Krauskopf, 1957). In addition, the presence of organic matter HCO^{3-}, SO_4^{2-} and HPO_4^{2-} also affects the behaviour of manganese in exogenic conditions (Hem, 1972, 1978; W. Stumm und J. J. Morgan, 1973). The initial precipitation of Mn oxyhydroxides by oxidation of aqueous Mn^{2+} leads to a metastable state that undergoes fast changes into stable species. Mn_3O_4 and γ-MnOOH were shown as the solid phases in equilibrium with seawater (Grill, 1982; Landing & Bruland, 1980). Experimental oxidation of Mn^{2+} has been shown to produce Mn_3O_4 and β-MnOOH (Stumm W & Giovanoli R, 1976), Mn_3O_4 (Murray et al., 1985), and γ-MnOOH (manganite) (Hem, 1978; Hem & Lind, 1983). Manganite is considered as the most stable species to be derived from Mn_3O_4 β-MnOOH by aging and in all these phases the oxidation number does not exceed +3. By contrast, the primary phases (todorokite, δ-MnOOH, birnessite) in modern Fe-Mn nodules the crusts approach the +4 oxidation number (Murray et al., 1984; Piper et al., 1984). This anomaly was explained by attributing kinematically controlled disproportionation reactions involving γ-MnOOH producing thermodynamically stable Mn^{4+} oxides (Hem, 1978; Hem & Lind, 1983; Lind, 1987) Owing to the transient nature of the Mn^{3+} phases in sedimentary conditions, the Mn^{2+}/Mn^{4+} redox couple effectively controls the precipitation of dissolved Mn^{2+} from solution (Roy, 2006) (Figure 1a).

The precipitation of Mn carbonate is controlled almost exclusively by high-level dissolved Mn^{2+} precipitation in pore waters, which in combination with dissolved bicarbonate, could exceed the solubility of Mn carbonate. (Roy,2006a). Such an extensive supply of dissolved Mn^{2+} is considered possible only in oxygen-stratified basins where Mn oxyhydroxides precipitated from overlying oxygenated seawater into the reduced zone below where they were buried and the dissolved Mn^{2+} could be in stable conditions (‘manganese pump’; Calvert & Pedersen, 1993, 1996). Mn carbonates (rhodochrosite, kutnohorite), which are hosted in black shales and carbonates-rich organic matter, are typically formed by the

diagenetic reaction of dissolved Mn^{2+} with organically derived dissolved HCO^{3-} in the anoxic zone. Such diagenetic Mn carbonates are depleted in ^{13}C indicating that the carbon originated, at least in part, from the organic matter. (Okita et al., 1988; P. M. Okita & Shanks III, 1992; Polgári et al., 1991). This high organic carbon flux to the anoxic zone of the stratified ocean can explained by enhanced plankton productivity in the continental margin setting, during transgression and followed by their decomposition and O_2 consumption during and after settling. (Roy, 2006). (Figure 1b).

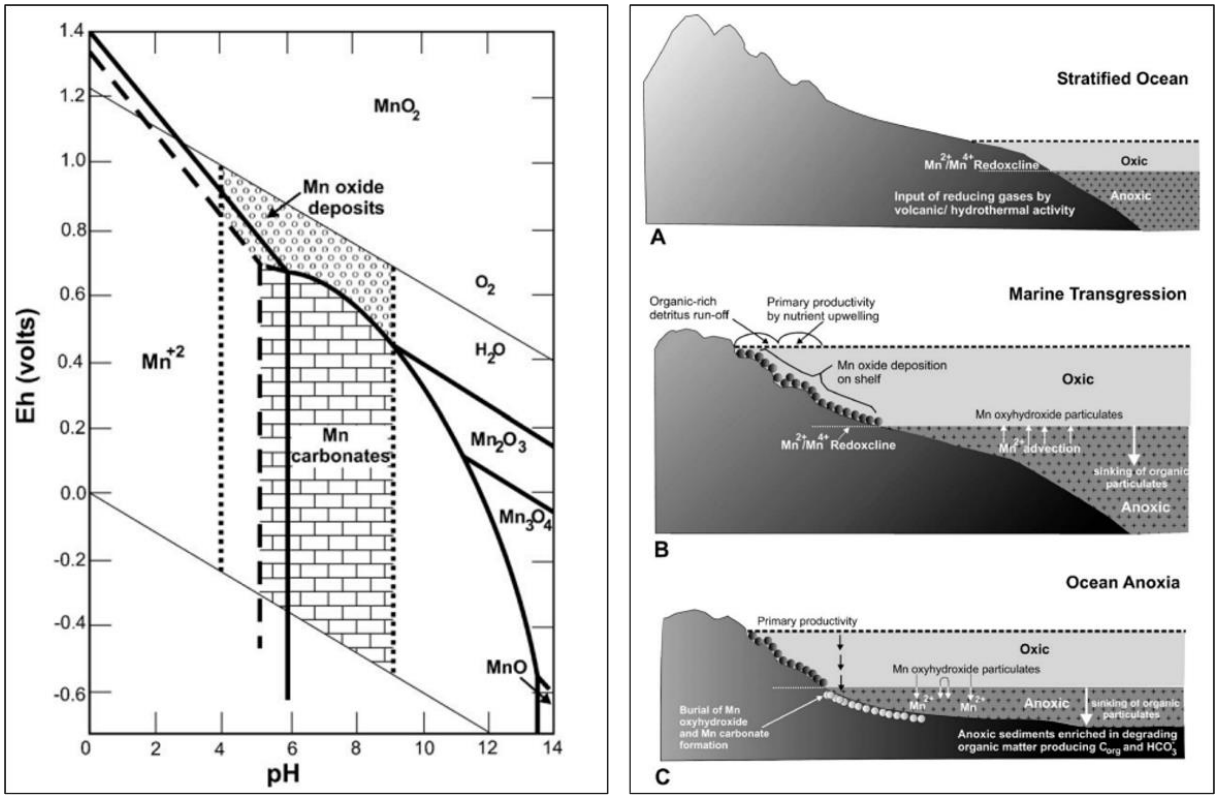

(a) (b)

Figure 1: (a) Stability of Mn oxides and carbonate deposits in natural water. The dashed bold lines represent 10-4 and 10-6 Mn^{2+}. The dotted lines represent the boundary of natural water (Krauskopf, 1957). (b) Mn deposition schematic related to sea level changes (Roy, 2006).

The processes regarding Mn deposition can be divided between those that are hydrothermal and those that occur at ambient temperature in a sedimentary environment. Both sets of processes can take place in a variety of tectonic and geochemical systems. Hydrothermal Mn deposits are found in smaller sizes in contrast to sedimentary ones. Sedimentary ones can be divided into two types, volcanogenic (or exhalative) and nonvolcanogenic (terrigenous), and are based on the presence or absence of volcanic rocks and their proximity in the sequence. Modern settings of sediment-hosted hydrothermal Mn deposits crusts, mounds, etc, are found

in either spreading centres or island arc types of environments, but they can be often confused with volcanogenic sedimentary deposits due to their similar attributes. Furthermore, the spatial association of volcanic rocks further induces uncertainty between the nature of Mn, hydrothermal or volcanic source, and only in certain locations, such as freshwater lakes and shallow seas can the terrigenous source of manganese be detected. In large open ocean basins, the Mn flux and the occurring deposits can have multiple sources. (Roy, 1992)

1.2 Sedimentary Manganese deposition during the Early Proterozoic Earth.

The Paleoproterozoic main characteristic was the ongoing evolution of large shallow sinking basins that acted as suitable repositories of sediments on a large scale intercalated with volcanic rocks (Roy,1988). In combination with the substantial free oxygen that was produced by photosynthetic prokaryotes plus the sufficiently oxygenated hydrosphere (and atmosphere) that could support significant biota, resulted in the deposition of both iron and manganese, in much greater amounts than was possible before this time. Iron formations peaked at the time of the Early Proterozoic while at the same time, Mn deposits started to develop on a substantially larger scale (Roy, 1988).

The oxygen production by cyanobacteria commenced at least ca. 2.75 Ga ago and no extensive rise in the O_2 content of the atmosphere-hydrosphere system was detectable until oxygen sinks (mainly reduced gases, organic matter, and Fe^{2+} in dissolved form) were overcome or removed. Organic matter burial was increased during periods of increased mountain building and could result in an increase in positive $\delta^{13}C$ values in certain pulses during ca. 2.4 Ga and ca.2.06 Ga (A. Karhu & Heinrich D. Holland, 1996; Buick et al., 1993; Melezhik et al., 1999; Melezhik & Fallick, 1994). The escape of hydrogen (reductant) to space following the photolysis of CH_4 might also have contributed to atmospheric oxygenation (Catling D.C. et al., 2001). This increase of oxygen in the atmosphere and interacting hydrosphere occurred at the same time as the deposition of large Mn deposits at the very early Proterozoic (Roy, 2006).

At the same time, the Late Archean supercontinents (Vaalbara/Zimvaalbara, Kenorland) were tectonically elevated and attenuated by the upwelling of the mantle, which could cause a geoid high before ultimate breakup (Michael Gurnis, 1988; Worsley et al., 1984). The continental areas were expanded and with the decrease of sea level, continental weathering at high rates was promoted, and as a result, massive areas of platform carbonates were formed

(e.g. Campbellrad subgroup, Postmasburg Supergroup) (Altermann & Nelson, 1998; Eriksson et al., 1998).

Some examples of Mn deposits during the Early Proterozoic include Mn deposition in the Transval Supergroup of the Kaapval craton, South Africa (ca. 2.5-2.4 Ga) where Mn beds of 1 m thickness are found intercalated with the Banded Iron Formation sequence (BIF). Mn deposition was linked with the transgression of Mn-rich deep anoxic waters of a stratified ocean (Beukes, 1993). The Kalahari manganese field in the ca. 2.4 Ga-old Hotatzel Formation consists of interbedded BIF (four distinct units) and three interlayered Mn ores that correspond to repeat transgression-regression cycles (Tsikos & Moone, 1997). The Paleoproterozoic greenstone of the Birimian unit in the West African craton (Ghana, Ivory Coast, Burkina Faso, Mali, eastern Liberia, Guinea) shows distinct settings and hosts significant Mn deposits hosted inside the Birimian greenstone sequence, which includes isoclinally folded volcanic rocks (mainly MORB-type basalts with a low amount of andesite, dacite, and minor rhyolite) underlay a package of chemical sediments, volcanoclastics, argillites and turbidites (Leube et al., 1990.; Roy, 1988). In the Guiana Shield (which is a continuation of the Birimian greenstone belt) in South America, manganese silicate-oxide ore and silicate carbonate protores are interstratified with metamorphic rocks that consist of low to medium-grade carbonaceous black shales, pelitic rocks and quartzites in the time equivalent Yuruari Series (Venezuela), the Barama series (Guyana) the Lower Paramaka series (French Guiana and Suriname) (Roy, 2006).

1.2.1 Serra do Navio deposit (Brazil)

The Serra do Navio Mn deposit is located in the Amazonian rainforest 235 km northwest of the regional capital of Macapá in the Amapa province of northwestern Brazil. The Mn deposit was exploited from 1957 to 1997 and during the early years of production it was one of the most important high-grade manganese ores for the North American market (Chisonga et al., 2012).

The deposit is hosted by metamorphosed and strongly deformed rocks of the Paleoproterozoic age forming part of the Guiana shield of the Amazonian craton and belongs to the Guianese Paleoproterozoic greenstone belts and more specifically to the Villa Nova Group (Kroonenberg et al., 2019). The rocks were metamorphosed during the Trans-Amazonian tectonothermal event that resulted in the rework of both the Archean basement, (lower rock unit of the Guiana shield) and the volcanic and volcano-sedimentary successions

that have been dated at 2.11 Ga (Voicu et al., 2001). The sedimentary sequence that hosts the Mn deposit constitutes part of such a Paleoproterozoic sequence that is exposed in the southwestern part of the Amapa Province. It forms a poorly exposed NW-SE striking fold belt that is composed of the Vila Nova Group and surrounded by granitic gneiss domes (Scarpelli, 1970).

The lithotypes of the Serra do Navio group include biotite and graphite schists, Mn-silicate rock, Mn-calcite, and rhodochrosite marble (Figure 2). The main Mn-bearing minerals identified are spessartine, tephroite, rhodonite, Mn-calcite, and Mn-amphiboles (Chisonga et al., 2012).

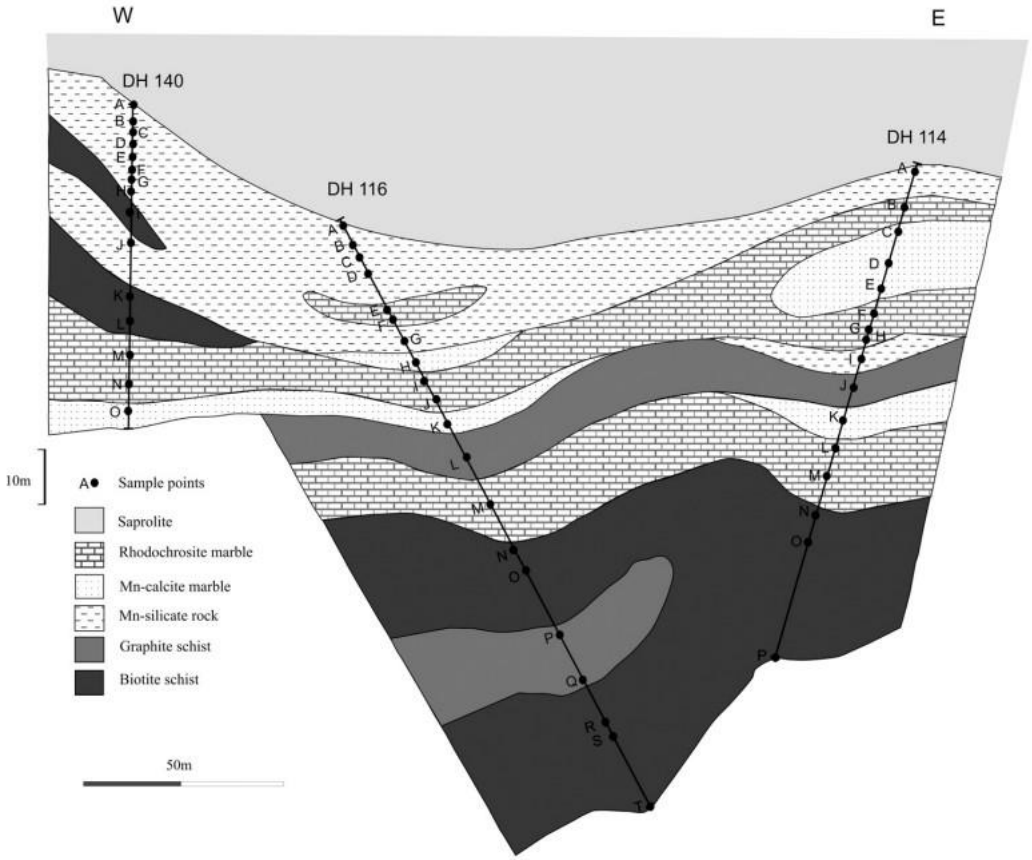

Figure 2: Schematic profile of the three drill cores at the Sera do Navio deposit.(Chisonga et al., 2012).

The mineralization was deposited in a marine environment and the siliciclastic/ volcanoclastic sediments were accumulated proximal to an active volcanic arc. Possibly Mn^{4+} oxyhydroxides precipitants were accumulated proximal to organic-rich matter sediments in deeper waters to account for the apparent abundance of organic matter and their transformation into diagenetic Mn carbonates. The carbonaceous pelites accumulated in a shallower marine environment under suboxic to anoxic conditions. (Chisonga et al., 2012).

1.2.2 Nsuta deposit (Ghana)

The Nsuta Manganese deposit is hosted in the Paleoproterozoic Birimian supergroup which is located on the eastern side of the West African craton (Nyame, 2008) and was deposited at ~2.2 Ga (Albani et al., 2010; El Albani et al., 2014). The Nsuta deposit's stratigraphy is composed of a basal greenstone unit followed successively upwards by argillaceous rocks and tuffs and greenstone (Kesse, 1976). The rocks that underlie and overlie the Mn carbonate proto-ore are grey to dark grey, fine to medium-grained, and variably bedded to laminated phyllite (Nyame, 1998). Other sedimentary structures identified include graded bedding, thin or localized slump structures, and various flame structures and intraclasts. (Nyame, 2001).

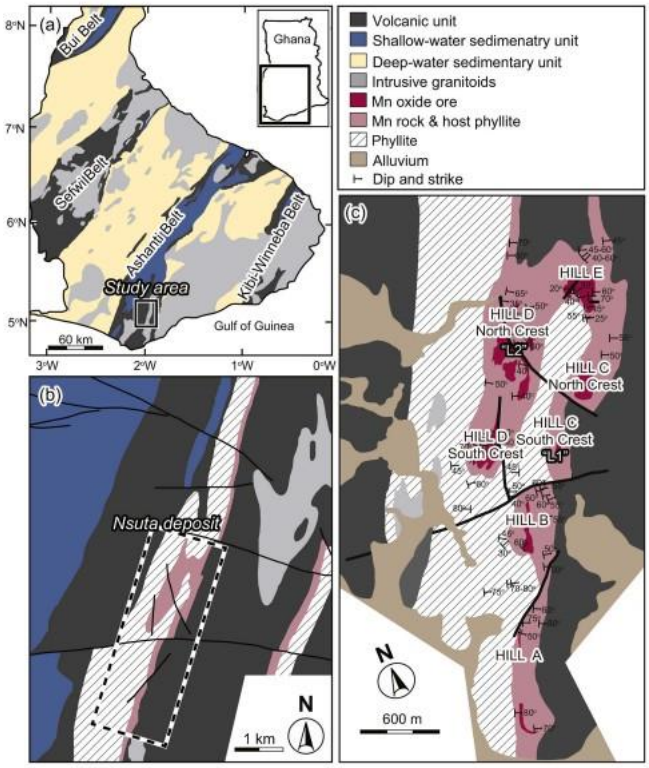

Figure 3: (a) Birimian Supergroup map (b,c) The Nsuta deposit(Goto et al., 2021)

The Mn-bearing rocks that have been reported in the Nsuta deposit include carbonates (rhodochrosite), silicate (gondite), and oxide (cryptomelane and pyrolusite) rocks. Mn-carbonate rocks are considered the least altered while in contrast Mn-silicate and Mn-oxide rocks are considered the products of local metamorphism and oxidative weathering respectively (Dixon, 1979; Nyame, 1998).

The Nsuta Mn deposit was deposited in a reduced marine environment in the outer margin where carbonate could be chemically precipitated resulting in a Mn carbonate-mud

marine sedimentation. Subsequent slumping, sliding and other gravity flows may have led to the formation of breccia, and the reworking of carbonate deposition by storms in the depositional environment (Nyame, 2008).

1.3 Purpose of Research

Although most of the Proterozoic Banded Manganese Formation (BMF) deposits have been studied thoroughly, little is known about the Mn deposition at Mathews Ridge in Guyana. This deposit is part of the Paleoproterozoic Greenstone Belt of the Guiana Shield in northern South America. Most of our knowledge about mineralization comes from an unpublished mining report from the Reunion gold company. A unique feature of this mineralization is that almost no iron can be found inside the mineralization as a primary metal. Thus, the purpose of this research is to understand the geochemical mechanisms that resulted in the deposition and preservation of Mn enrichments at this locality. More specifically, the main geochemical features of the basal rock unit will be analysed to understand the geochemistry of the rock unit, and its petrographical features and a first assessment of a deposition model will be introduced to explain the Mn deposition and preservation. The above results will be compared with the Paleoproterozoic Manganese deposits of Serra do Navio (Brazi) and Nsuta (Ghana) to recreate the redox environment of the Early Proterozoic Ocean.

2 Geological Setting

2.1 Guyana Shield and Greenschist belts

Matthews Ridge is a region located in the northwest of Guyana, on the northern coast of South America. Rocks in this area belong to the Barama group, part of the Barama-Mazaruni supergroup. This group encompasses multiple greenstone belts across the central-western part of the Guyana Shield (Guyana, 2013). The geological strata of the Guiana Shield are characterized by two primary lithological sequences. The more ancient geological units compromise the orogenic Archean and Paleoproterozoic sequences, exemplified by the Imataca Complex in Venezuela and the Trans-Amazonian granitoid-greenstone belts (Voicu et al., 2001).

The Guianese belts (2.26-2.09 Ga) (Kroonenberg et al., 2019) are usually divided into two lithological units (Gibbs, 1987; Gibbs, 1983). The stratigraphy of the lower rock unit indicates a classical succession with a tholeiitic mid-ocean ridge or back-arc basin basalts at the base, often with pillow structures, followed by sequences of more evolved island-arc-type andesites, dacites, rhyolites, and intercalated chemical sediments that were deformed and metamorphosed before the deposition of the upper unit. In contrast, the upper unit is composed of clastic meta-sediment rocks, that include greywackes and shales deposited as turbites, in combination with intermediate to felsic meta-volcanic rocks and mafic and ultra-mafic meta-volcanic rocks in smaller amounts. On top of the sequence, they are typically overlain unconformably by a sequence of epicontinental fluvial deposits (Capdevila, 1999; Choudhuri, 1980; Kroonenberg et al., 2019). The belts were shaped at the time of the Trans-Amazonian Orogeny, between 2.26 and 1.98 Ga, as a consequence of seafloor spreading, with southward subduction and finally the continental collision, between the ancestral Guyana Shield and the West-African craton, where they continue into the Birimian of West-Africa (Figure 2) (Delor, 2003; Gibbs and Gabbon, 1993). The entirety of the rocks have been metamorphosed to greenschist facies conditions that can locally reach up to amphibolite facies, near the boundaries of tonalite-trondhjemite-granodiorite (TTG) intrusions (2.18-2.11 Ga) (Figure 4) (Kroonenberg et al., 2019).

The Barama-Mazaruni supergroup follows a similar greenstone belt stratigraphy and is composed of tholeiitic basalts and associated mafic to ultramafic dykes and sills, that are overlain by intermediate-felsic volcanic rocks, interlayered with thick sedimentary and volcanic-sedimentary rocks. The syn-to late-tectonic calc-alkaline Trans-Amazonian

'granitoids' are intruded into the supergroup, ranging from felsic to intermediate composition (Vanderhaeghe et al., 1998).

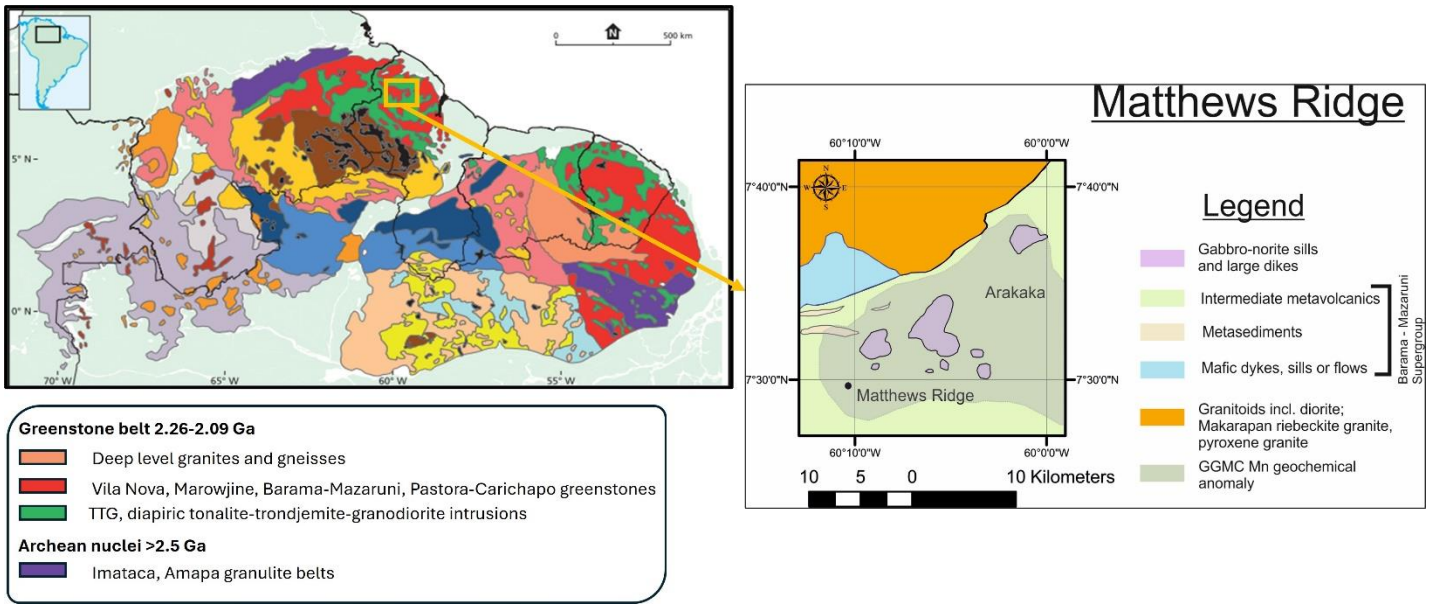

Figure 4: Modified, Guyana shield map, from Kroonenberg et al., 2019. The box in yellow highlights the Barama- Mazaruni Supergroup and the Matthews Ridge area.

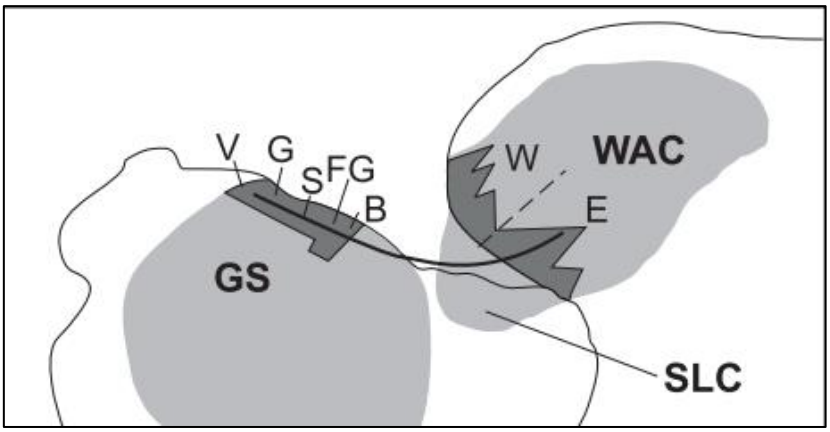

Figure 5: Modified, Paleogeographic reconstruction map at 2.0 Ga, suggested by, Ledru et al., 1994, Cratonic areas in mid grey: GS-Guyana Shield; SLC-São Luiz Craton; WAC-West African Craton. Darker grey areas, schematic representation of areas of the greenstone-granite belts in the Guyana Shield, V-Venezuela, G-Guyana, S-Surinam, FG-French Guiana, B-Brazil; W and E-western and eastern belts in the West African Craton.

2.2 Matthews Ridge Regional Geology

The Matthews Ridge Mn deposit is part of the Mathews Ridge Formation (MRF), which belongs to the Barama group of the Barama-Mazaruni supergroup. Little is currently published about the area and the Mathews Ridge Formation in general. Most of our knowledge currently comes from the unpublished Reunion Gold Corporation mining report.

The Barama group rocks were deposited in a basin environment. They can be divided into three formations which are from top to bottom, the Arakaka Formation contains a coarser sedimentary series and rudites, intercalated with volcanic piles and intrusives of mafic to acidic affinity, followed by the Matthews Ridge Formation (MRF) and overlain the Tenapu Formation. The rocks are all of low metamorphic grade and make up a predominately sedimentary sequence of very-fined clastic (pelitic) and chemical sediments that were most likely deposited in a marine environment. (Guyana, 2013).

The MRF sedimentary sequence is composed of a thick basal lower phyllitic unit (LPHY) that contains, thin and very local manganiferous and occasional chert beds, which appear to be over 75m thick. As the series progresses upwards, it progressively grades into a manganiferous phyllitic unit (MPH), which is constituted of phyllites intercalated with very thin manganese-rich beds. This unit is approximately 10 meters thick and overlain by a Banded Manganese Formation (BMF), which is described by well-stratified intercalations of phyllites and Mn-rich beds, that sequentially lead into a thick Massive Manganese unit (MMF). The BMF thickness varies from 10 to 15 meters, as the MMF unit is estimated to be around 1 to 3 meters thick. On top of the sequence, the Upper Phyllites unit (UPHY) appears. The contact between the two beds is sharp, while there are no manganiferous beds inside the UPHY and the thickness of the unit is more than 100 meters. The whole sedimentary sequence is crosscut by late dioritic intrusions, forming dikes, sills, and dome-like structures (Figure 3) (Goulet, 2012).

The sedimentary sequence has been tectonically deformed creating folds that are characterized by thickening in the hinge zone and thinning in the flanks. This is considered the product of the first deformation, which had a considerable impact on the mineralization as it is repeated several times in the same manganese beds by anticline and syncline fold structures with axial plans dipping south 40 degrees, trending east-northeast. While also subject to lateritic weathering, creating a typical laterite profile at the top of the sequence. (Guyana, 2013).

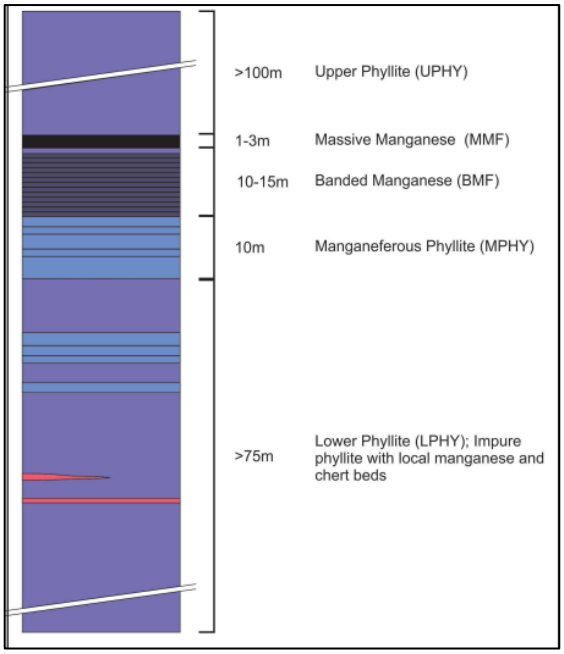

Figure 6: MRF stratigraphic sequence(Goulet, 2012)

Figure 7:Banded Manganese Unit (BMF) Affected by Typical Anticline and Syncline Structure (Guyana, 2013)

3 Methods

3.1 Sampling

For this research, 23 phyllite samples were retrieved from four drill cores, part of the Reunion- Gold Corporation geological exploration program. The samples include nine samples from drill core 11MR1001 (74.7m-87.6m) from hill 7, eight samples from core 11MR1091 (85m-106.6m) from hill 9c, two samples from drill core 11MR1094 (64.4m-73.5m) and three samples from drill core 11MR2014 (69.9m-75.4m) of an unknown location. All samples were retrieved right below the CSR zone (saprolite zone) as they were the only ones available from the targeted drill holes retrieved from the geological model documented in the NI-43-101 technical report. Drill cores of the upper stratigraphy units (MMF and BMF) were not documented well at that time and were mostly of saprolitic material. Therefore, the least samples, of the basal phyllitic unit were selected which likely preserved primary geochemical signatures even though the deposit has been affected by multiple tectonic phases and metasomatism. The cross-sections and the sampling depths of the cores 11MR1001 and 11MR1091 are seen in Figures 5-7.

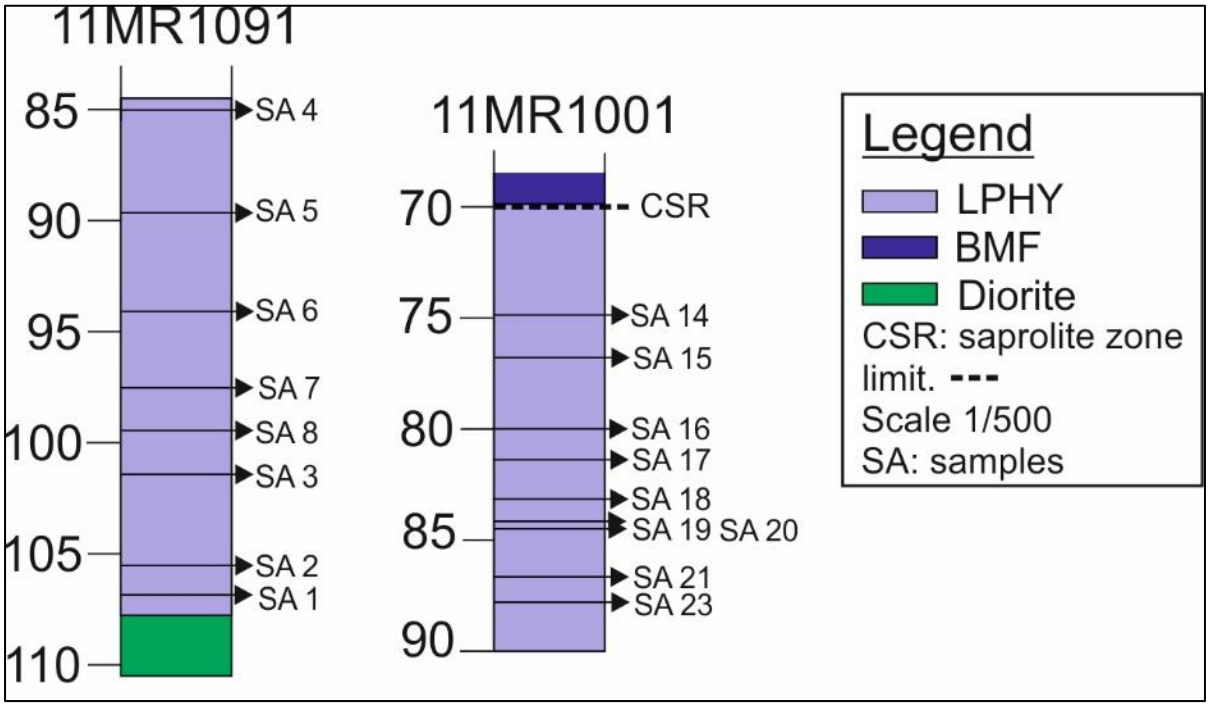

Figure 8: Sampling of Corres 11MR1001 and 11MR1091.

Figure 9: Cutting of cores during sampling.

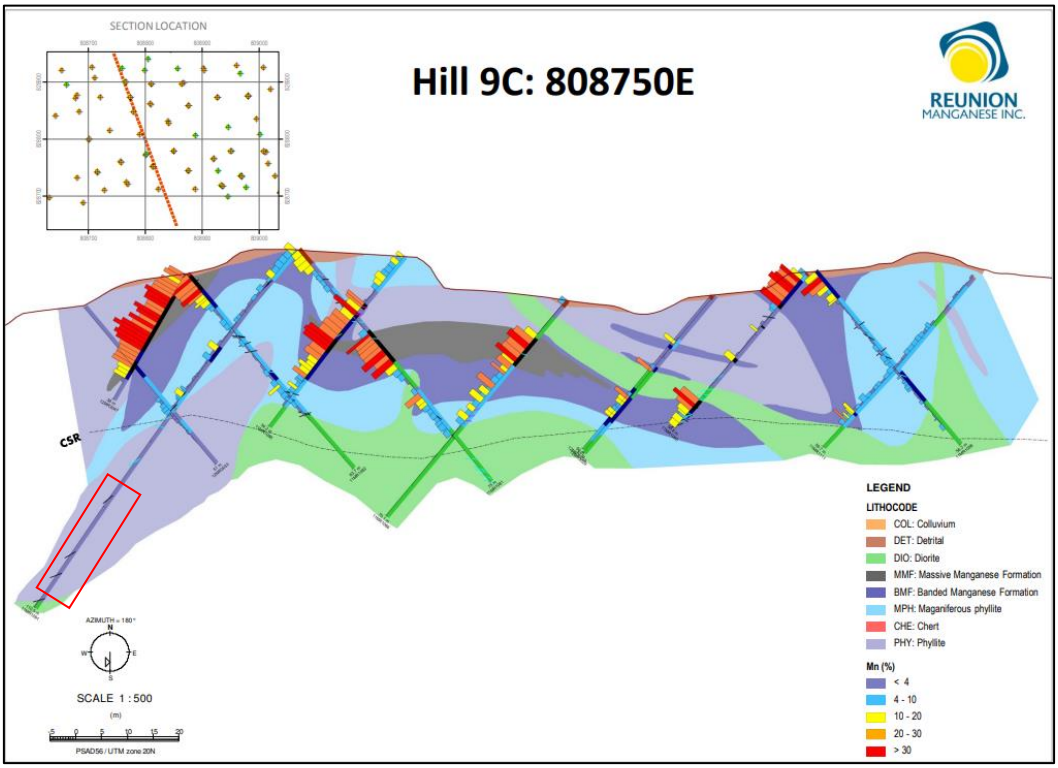

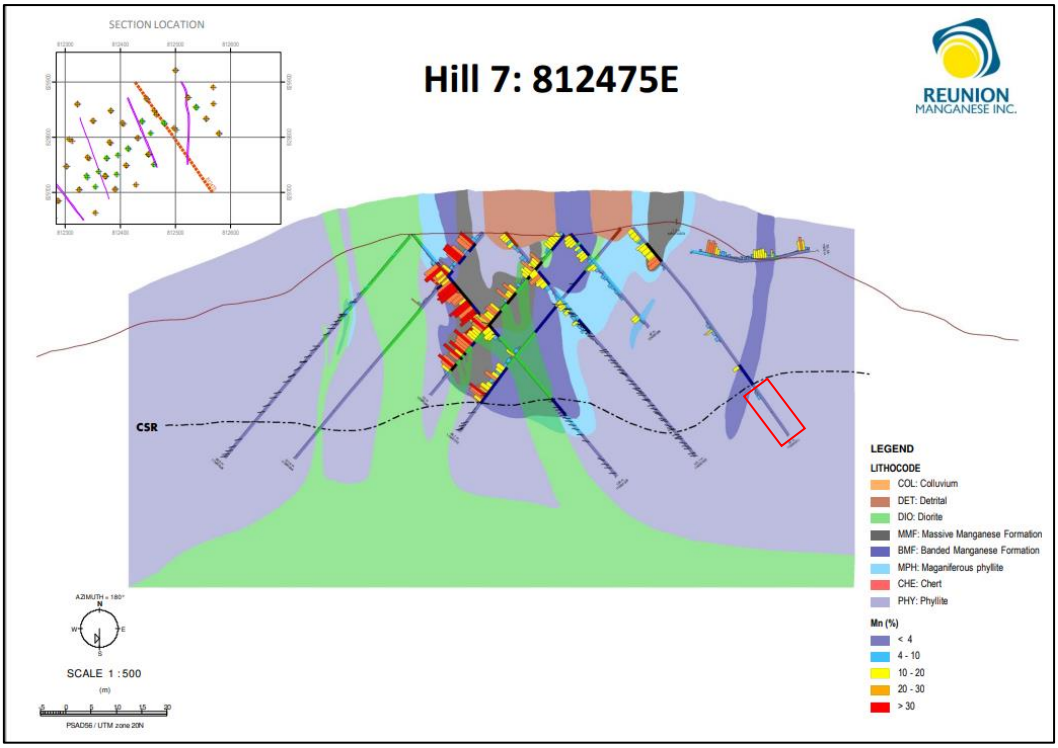

Figure 10: Cross sections of the Mathews mineralization. With red are highlighted the two cores that were sampled (Guyana, 2013).

3.2 Microscopy

Polished thin sections were prepared at Utrecht University for the samples of drill core 11MR1001 (nine samples). All thin sections were digitalized using ZEISS Axioscan. Petrological and mineralogical characteristics were determined through optical microscopy using an Axio Scope with a colour 305 Axiocam. Mineral compositional analyses of three samples of 11MR1001 were acquired on an electron microprobe (JEOL JXA-8530F) at Utrecht University equipped with 5 tuneable wavelength dispersive spectrometers. Operating conditions were 40 degrees take-off angle, and a beam energy of 15 keV, for all measurements. The beam current was 20 nA, and the beam diameter was 10 microns for most spots, except for a few measurements that used a more focused beam of 1 micron. Both peak and background counting times were 20 seconds. The Teph and Diops house standards were used to calibrate the instrument. For the electron microprobe, a thin carbon coating was applied on the surface of the thin sections to induce conductivity and prevent the build-up of electric charge.

3.3 Whole Rock Chemistry

After measurement by XRF, the glass beads were broken into small pieces, and the fragments were used to measure the trace elements by laser ablation inductively coupled plasma mass spectrometry (LA-ICP-MS). The analysis was performed with a Lambda Physik 193 nm wavelength COMPex 102 ArF excimer laser ablation system, connected to a Thermo Fisher Scientific-X Series 2 ICP-MS at Utrecht University. The mass- spectrometer was operated at low resolution. A 10 Hz laser repetition frequency was used with a fluence of 2-12 J cm2. Each measurement included a 50-second background interval, followed by 70 seconds of ablation. The data was acquired and calibrated against the standard NIST SRM 612 glass using Glitter software and accuracy was assessed by the USGS basalt standard BCR2-G.

For the reproducibility and precision of the data, three spots were measured in each sample that created craters of 120 μm diameter on the fusion beads After the homogeny of each sample was determined, the average of the three measurements was measured as a result, and presented with the standard division in Appendix 1.REE+Y anomalies calculations.

Due to the distinguishing behaviour of the rare earth elements and yttrium (REY) in seawater, they are often used to provide information about the depositional environment of the sediments (Bolhar & Vankranendonk, 2007; Kamber & Webb, 2001). When normalized to PAAS (post Archean Australian Shale, Pourmand et al., 2012) it produces smooth distribution patterns. Normalizing REY with PAAS is a common practice to remove natural variation in the absolute concentration of REY and allows the comparison with the upper continental crust for which shale is a proxy (Tostevin et al., 2016).

Usually, anomalous REE abundance spikes are expressed as the ratio, of the observed element divided by the value, interpolated from immediately neighbouring trace elements. The general expression is $[REE_n/REE_n^*]=2REE_n/(REE_{n-1}+REE_{n+1})$, where REE is the shale-normalized abundance and n=1, 2, 3,… is the REE in the order of the lanthanide series (e.g. La=1). This simple principle was initially used for the calculation of the Ce and Eu enrichment in igneous rocks. Due to the complexity of the marine REE systematics, this principle is not strictly applicable to seawater (and precipitants) (Bolhar et al., 2004). The calculation of the anomalies presented in this study are as follows:

I. Ce anomaly: Ce is unique among the REY since it can exist in both +3 and +4 oxidation states. In the presence of oxygen, Ce (III) is partially oxidized to Ce (IV)on the surface of Mn (oxyhydr)oxides, where it no longer participates in solid-solution exchange

reactions, leaving residual seawater depleted in Ce relative to other trivalent REE (German & Elderfield, 1990). This fractionation occurs only under oxic conditions (German et al., 1991). Traditionally the anomaly is calculated by comparing the normalized concentrations of Ce with the neighbouring REE (La and Pr) by using the formula proposed by Bau and Dulksi,1996:

$$Ce_{sn}/Ce_{sn}^{*}=\frac{Ce_{sn}}{0.5*La_{sn}+0.5*Pr_{sn}}$$

The anomalous behaviour La can artificially exaggerate the Ce anomaly. That is why a more appropriate way to calculate the Ce anomaly avoiding the comparison with La (Lawrence et al., 2006):

$$Ce_{sn}/Ce_{sn}^{*}=\frac{Ce_{sn}}{(Pr_{sn})^{2}/Nd_{sn}}$$

II. Eu anomaly: On a similar note, Eu anomaly was calculated by comparing the normalized concentrations of Eu with the neighbouring REE (Sm and Gd). BaO can cause significant spectral interference with Eu (Jarvis et al., 1989; Smirnova et al., 2006). However, no correlation was noted between Ba and Eu anomalies (r^2=0.0358) (Figure 8). Although, because of the anomalous abundances of Gd, Eu_{sn} anomalies have been quantified as (Bau & Dulski, 1996):

$$Eu_{sn}/Eu_{sn}^{*}=\frac{Eu_{sn}}{0.67Sm_{sn}+0.33Tb_{sn}}$$

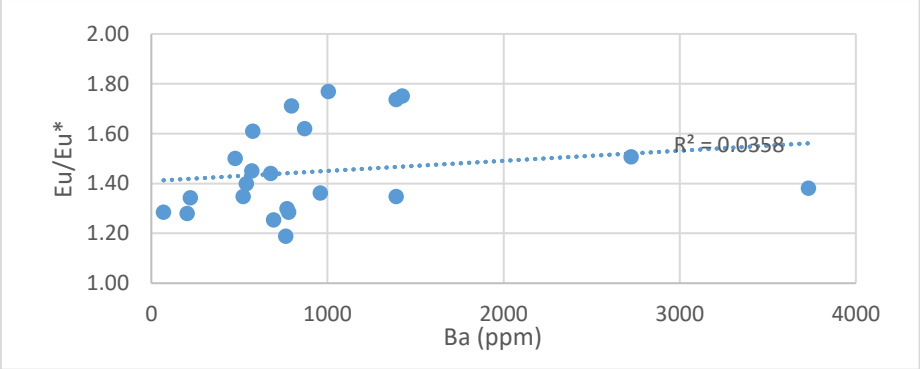

Figure 11: Eu/Eu*-Ba, Harker variation diagram.

III. Y anomaly: Y is inserted between Dy and Ho according to its ionic radius. The closest similarity exists between Y and Ho, hence the anomalous behaviour of Y concerning the REEs will be evaluated by considering Y/Ho ratios (Bau & Dulski, 1996).

3.4 Chemical Alteration Indexes Calculations.

To understand the chemical weathering trends of the LPHY rock unit, several chemical alteration indexes were calculated. The indexes are the chemical index of alteration (CIA)

proposed by Nesbitt & Young (1982), the mafic index of alteration (MIA), and the index of lateralization (IOL) proposed by Babechuk et al. (2014). For their calculations, the molar fractions of the major oxides were used for the CIA and MIA indexes, and the % values for the IOL index and presented as % below.

$$CIA = 100 * \left(\frac{Al_2O_3}{Al_2O_3 + CaO + Na_2O + K_2O}\right)$$

$$MIA = 100 * \left(\frac{Al_2O_3}{Al_2O_3 + Fe_2O_3 + CaO + MgO + Na_2O + K_2O}\right)$$

$$IOL = 100 * \left(\frac{Al_2O_3 + Fe_2O_3}{SiO_2 + Al_2O_3 + Fe_2O_3}\right)$$

4 Results

4.1 Petrographic features of core 11MR1001.

4.1.1 Petrography of core samples

All the phyllite core samples of 11MR1001 appear to have yellow, orange, and grey colours. The phyllites are composed of a typical phyllite rock paragenesis that includes micas (muscovite/illite/Al-illite hydromica/chlorite), quartz, and feldspars, alongside Fe-oxides (hematite, magnetite, ilmenite) and Mn-oxides (cryptomelane, todorokite, lithiophorite). The preferred orientation of micas and chlorite defines the well-developed schistosity planes. Elongated grains of quartz of quartz and feldspar run parallel to the schistosity planes.

Two varieties of muscovite have been identified based on the grain size and grain relationship to other minerals. Muscovite type I has a small grain size that shows preferred orientation marking the schistosity along with illite and chlorite grains. Muscovite type II appears with bigger developed crystals showing angular relationship with quartz crystals and in some cases, it is developed on top of deformed quartz crystal, or with a smaller grain size in between microcrystalline quartz as a matrix alongside illite. Chlorite shows a yellowish green to light green pleochroism with first-order interference colours. It shows the preferred orientation marking the schistosity along with mica minerals. The mica bends round or is pushed aside slightly by quartz grains which indicate quartz formation before or during the matrix development.

Quartz appears fined grained in most cases alongside a small number of feldspars parallel to the schistosity plane. Recrystallized quartz shows a wavy extinction, and inclusions

of muscovite were observed. Also, quartz veins occur parallel to the schistosity plains, along with small amounts of micas and well-formed hematite crystals (as opaque minerals).

Iron oxides include well-formed hematite crystals and microcrystalline hematite parallel to the schistosity planes, either in between quartz as a matrix or on top of quartz and mica crystals. Magnetite and hematite crystals occur alongside secondary manganese minerals such as cryptomelane, todorokite, and lithiophorite in sample 11MR1001(76.6m) that has been developed parallel to the schistosity planes. Lastly, ilmenite crystals appear as opaque minerals.

4.1.2 Tectonic Features

Post-tectonic features and mylonite zones are frequently observed in the majority of samples. The mylonites are characterized by a homogeneous planar fabric defined collectively and aligned phyllosilicate minerals (including muscovite, chlorite, and illite) polycrystalline quartz, or heavily deformed quartz and a fine-graded mylonitic ” paste” rich in quartz, micas, and Fe-oxides (Figure a,b,e,f).

Other post-tectonic features include the kinking of micas, and the deformation of quartz crystals, shattered quartz crystals, surrounded by mica crystals. (Figure 9g).

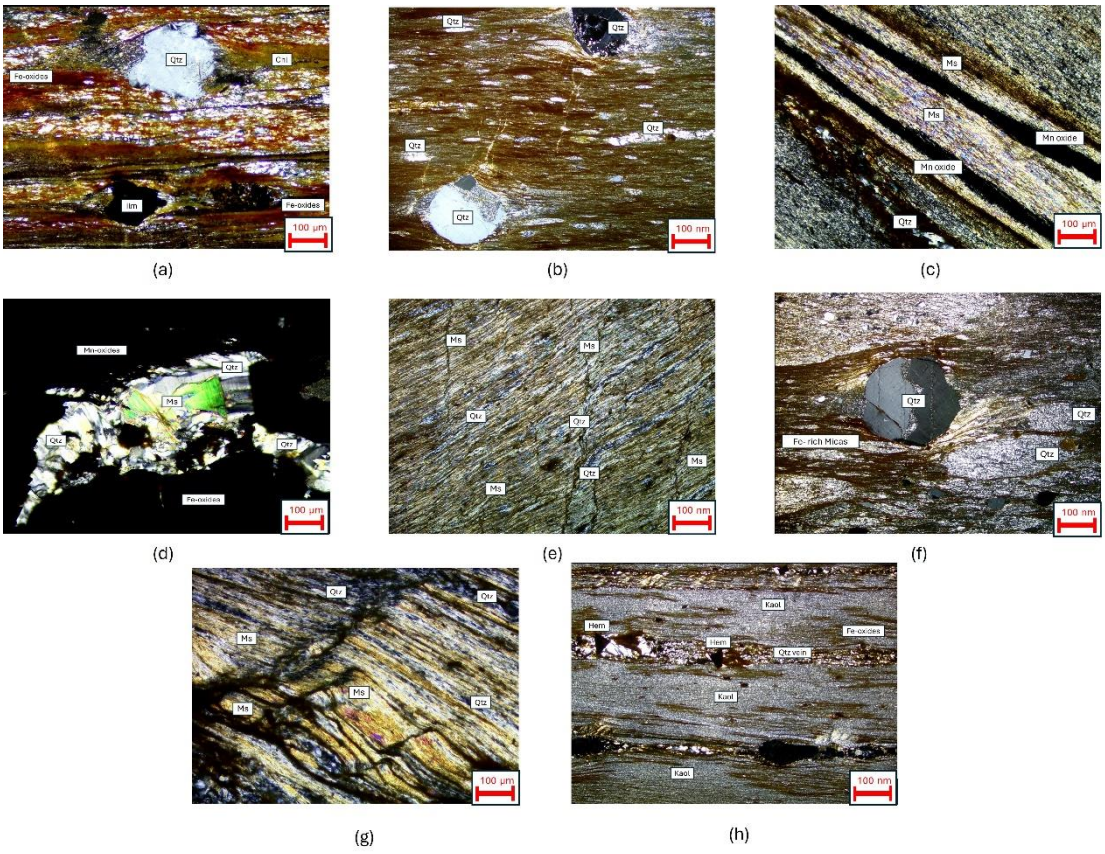

Figure 12: Thin sections images (a)11MR1001(81.3m), (b) 11MR1001(79.8m),(c)11MR1001(83.4m), (d and g) 11MR1001(76.6m) (e) 11MR1001(87.6m), (f)11MR1001(79.8m), (h) 11MR1001(74.4m).

4.1.3 TT-SEM and Microprobe Findings.

Through the TT-SEM and microprobe analysis, the identification of different phyllosilicate minerals is established while also the identification of the different oxides based on their chemistry is presented in Appendix X. The phyllosilicate minerals include micas: muscovite, illite, chlorite, and kaolinite and are identified by using microprobe analysis. All micas have a low percentage of potassium (K) and it was able to identify Al-illite hydromica a variety of muscovite low in K_2O wt.% and high H_2O wt.%. A lot of micas appear to be enriched in either Fe or Mn. Chlorite minerals are Fe-rich and Mg-poor. Kaolinite is identified using SEM analysis and is only found in core samples 11MR1001(74.7m), 11MR1001(76.6m), and 11MR1001(89.7m). The Fe-oxides include hematite, magnetite, and ilmenite, while the Mn-oxides include cryptomelane and lithiophorite. Other minerals that were identified using SEM analysis are small monazite crystals on top of Fe and Mn oxides.

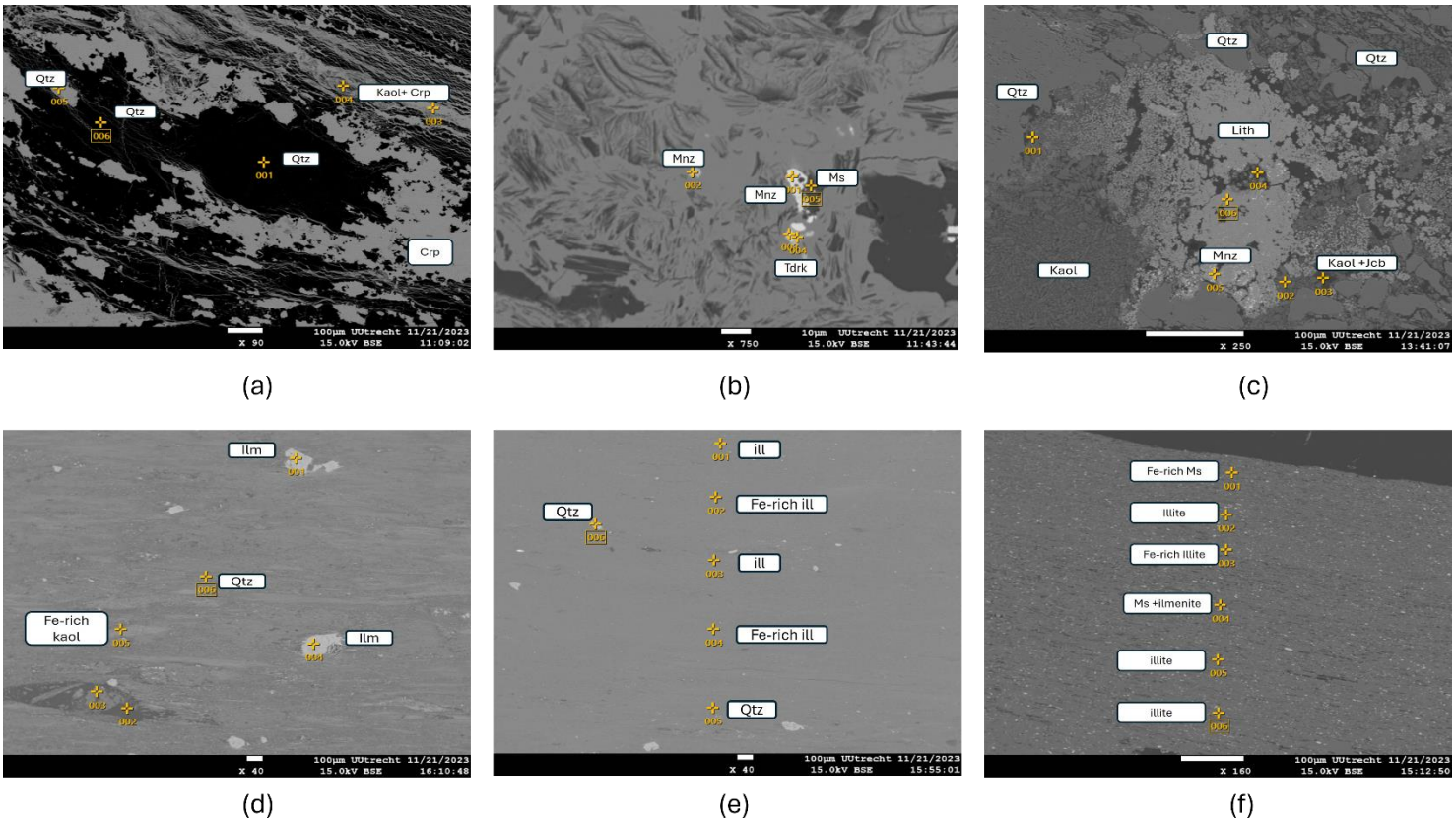

Figure 13:SEM pictures, a-c SEM pictures of thin section 11MR1001(76.6m) focused on the secondary Mn mineralization, d-f SEM images of thin section 11MR1001(81.3m).

4.2 Major element oxides.

The whole rock and trace element chemical data of the 23 analysed samples is shown in Appendix 1. The lower phyllite unit (LPHY) is characterized by low to moderate silica

(SiO_2) concentrations ranging from 48.17 wt.% to 74.42 wt.%. Aluminum (Al_2O_3) content is also high ranging from low to high values from 3.86 wt.%. up to 23.97 wt.%. The iron content of the phyllites (total Fe as Fe_2O_3) is characterized as low to moderate ranging from 3.28 wt.% to 10.85 wt.%. The manganese content (total Mn as MnO) is less than 1 wt.% in most of the samples in contrast to two samples 11MR1001(7.6.6m) and 11MR1001(87.6m) that display Mn values of 24.94 wt.% and 16.63 wt.%, respectively. Other major element oxide contents include, K_2O (-0.21 wt.%-2.97 wt.%.), MgO (0.05 wt.%-2.97 wt, %), Na_2O (0 wt.%-1.77 wt, %), P_2O_5 (0.01 wt.%-0.17 wt.%) and TiO_2 (0.16 wt.%-1 wt.%).

The lower phyllite unit is mainly composed of quartz and phyllosilicate minerals (white micas). For this reason, Al_2O_3 was chosen as a fractionation index for creating Harker variation diagrams that are presented in Figure 8. In most diagrams, the entire dataset has a similar behaviour by comparing the major oxides with the aluminium content, although in some cases cores 11MR1001 and 11MR1091 follow opposite trends. A strongly positive trend is observed between TiO_2-Al_2O_3 and a weaker positive correlation between Fe_2O_3-Al_2O_3. A negative correlation is observed between SiO_2-Al_2O_3, and no correlation is observed between MnO, MgO, and P_2O_5-Al_2O_3. By comparing the cores 11MR1001 and 11MR1091, it is apparent of the variability in the geochemical content of the samples since a difference was observed in the CaO-Al_2O_3 and K_2O-Al_2O_3 variation diagrams. In 11MR1001 a strong negative correlation can be observed for CaO-Al_2O_3 while in contrast a strong positive correlation between K_2O-Al_2O_3 is observed. Vise-versa in 11MR1091 core samples, a positive correlation between CaO-Al_2O_3 is noticed and a none to a weak correlation between K_2O-Al_2O_3. The same trend is also noted for the Na_2O-Al_2O_3 variation diagram (Figure 14).

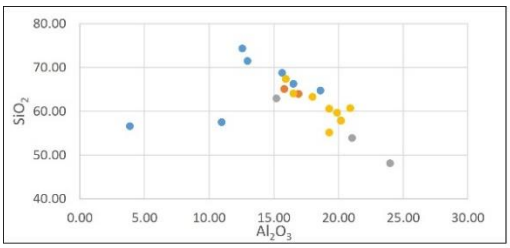

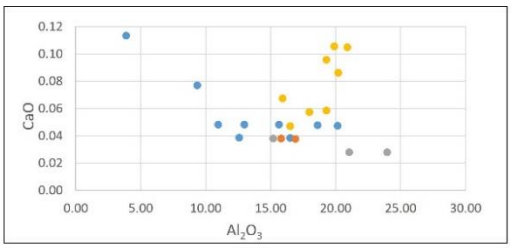

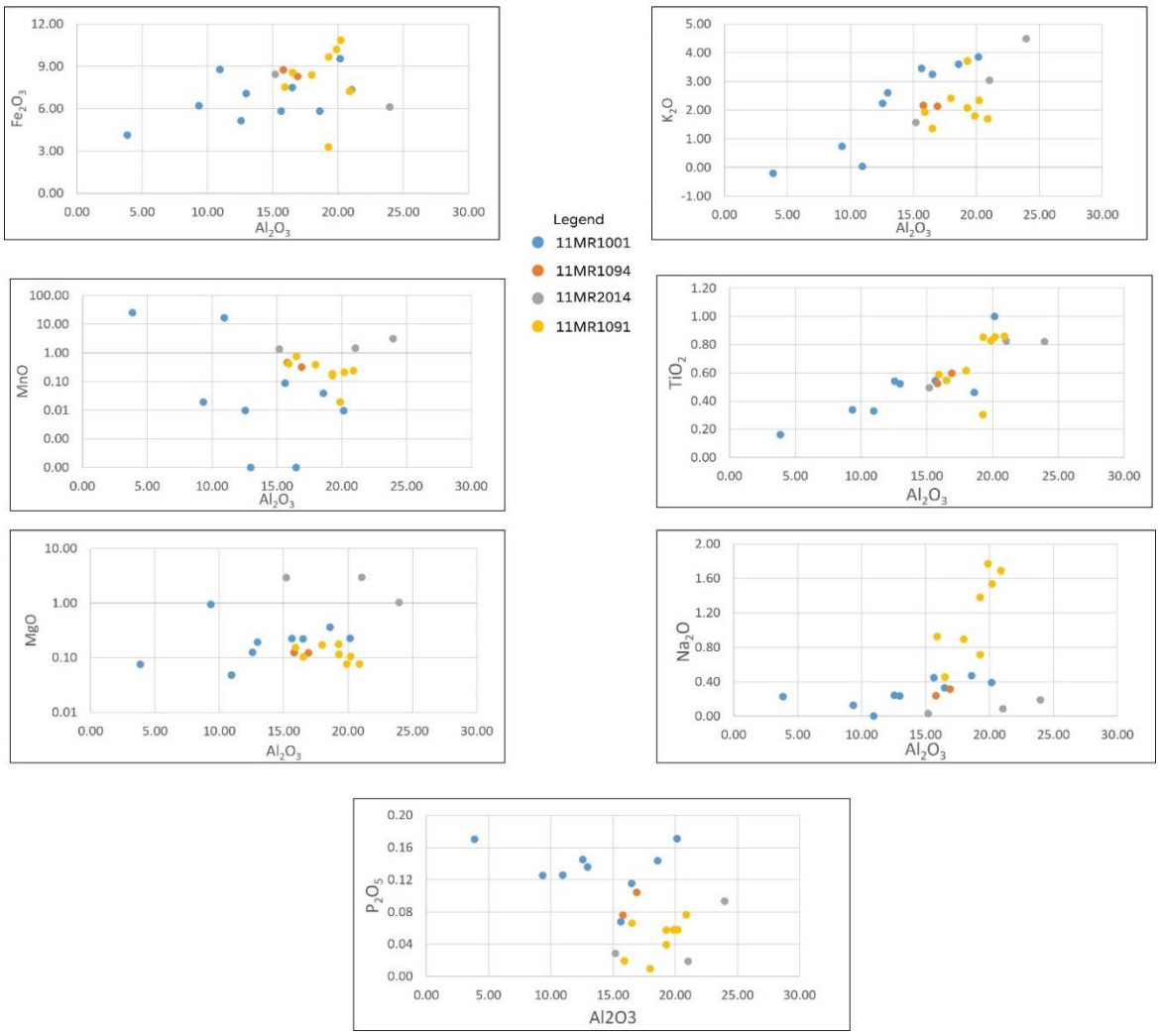

Figure 14:Harker variation diagrams of major oxides. (major oxides are presented as %).

4.3 REE+Y patterns.

The PAAS normalized patterns of the 23 analysed samples are presented by core in Figure 9. Again, the variability of the geochemical content between the samples is clear, and different patterns of REE+Y distribution can be detected, although there are features that remain in all samples. All samples appear to have positive Eu anomalies, with their values ranging from 1.19 to 1.77. Also, all samples present positive Y anomalies with weak to absent Y/Ho anomaly values that range from 24.65 to 32.88, while the Ce anomalies are variable from strongly negative (0.24) to strongly positive (4.42). All samples show a negative to zero correlation between Al_2O_3 indicating zero terrestrial REE influence (Figure 15).

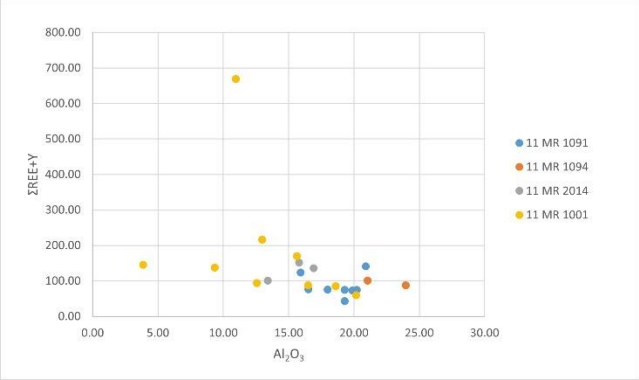

Figure 15: ΣREE+Y and Al_2O_3 harker variation diagram.

Most of the samples from core 11MR1091 have a positive slope (LREEs<HREEs), in their REE pattern, similar to seawater patterns, except samples 97.5m and 101.4m which have a slightly negative slope (LREEs>HREEs). Only some samples show Y anomalies, while Ce anomalies vary from sample to sample. Samples from the depth of 106.6m to 97.5m have a weak to strong negative Ce anomaly, and samples from the depth of 94m to 85m have a strong positive Ce anomaly. A similar positive slope pattern is observed in core 11MR1094 samples, with solid positive Ce anomalies, and weakly positive Eu and Y anomalies.

In contrast to these two cores samples, samples from cores 11MR1001 and 11MR2014, have a relatively flat REE pattern (LREEs=HREEs), similar to the UCC pattern, to a very weak positive one except for sample 11MR1001(81.3m) which has a positive slope. The samples have weak positive Eu anomalies and very weak positive to no Y anomalies. Most samples have a weak or absent Ce anomaly except for sample 11MR1001(83m) which appears to have a strong negative Ce anomaly. 11MR2014 samples have even more flat patterns with strongly positive Eu anomalies and less strong positive Y, while Ce anomalies are very weak, and they vary from flat (74.5m) to negative (73m) to positive (69.9m) (Figure 16).

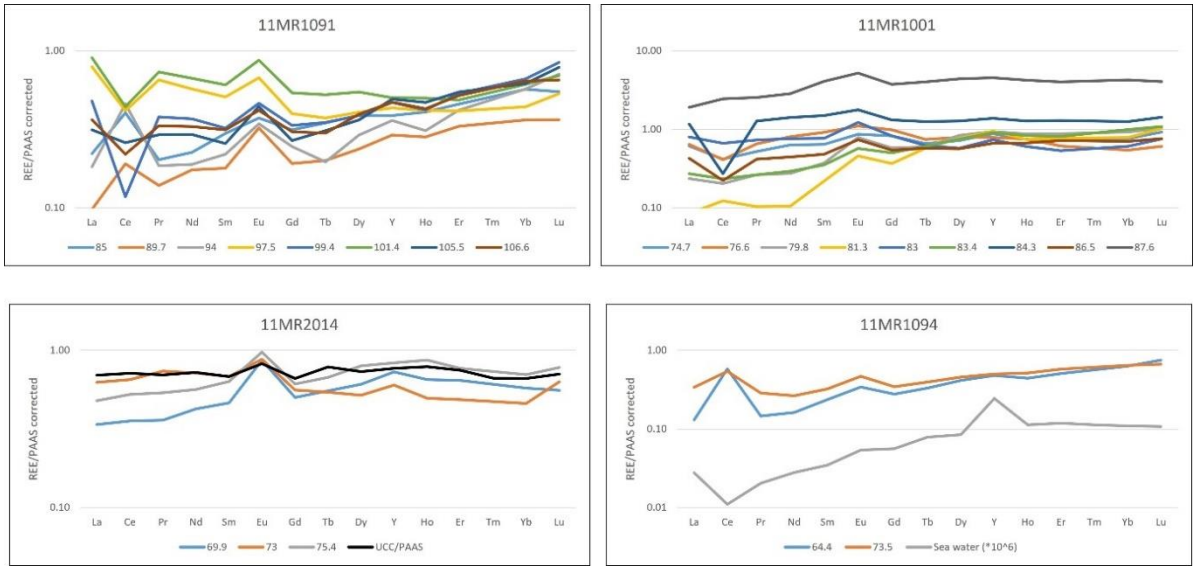

Figure 16: REE+Y (PAAS normalized) patterns of the 23 samples.

4.4 Chemostratigraphy of cores 11MR1091 and 11MR1001.

To understand the distribution of the major and trace components inside the two cores and their changes, chemostratigraphic diagrams of iO_2, Al_2O_3, MnO, Fe_2O_3, K_2O, Ba, MgO, and CaO were created and presented in Figures 17 and 18. The major oxides are in wt.% and Ba is in ppm.

Samples in core 11MR1001 contain a relatively higher amount of SiO_2 (56.72-74.72 wt.%) in contrast with the samples in core 11MR1091(55.19-67.49 wt.%) with the values fluctuating with depth. In core 11MR1001 the peak can be found at the depth of 74.7m and drops sharply to the lowest value observed at 56.72 to the depth of 76.6m, afterward the values rise with depth with minor fluctuations and reach the value of 74.42 at the depth of 86.5m and again it drops very suddenly at 57.57 at the depth of 88m. In contrast, in core 11MR1091, at the top of the core the drops strongly from 64.14 at the depth of 85m to 55.19 at the depth of 89.7m. From there the value increases steadily to the value of 67.49 at the depth of 97.5m and falls to the value of 59.72 at the depth of 99.4m. Then, the value remains relatively steady with minor fluctuations until the depth of 106.6m reaches 60.63.

By contrast to Silica content, Al_2O_3 presents higher values in core 11MR1091 rather than core 11MR1001, with the values ranging from 15.91 to 20.90 and 3.86 to 20.16, respectively. In core 11MR1001, at the top of the core at a depth of 74.5m, the value is at 9.34 and drops slightly at 3.86 at the depth of 76.6m, similar to SiO_2. From there the values greatly increase to the value of 18.6 at the depth of 79.8m and continue to grow until it reaches 20.16 at the depth of 81.3m and then drops steadily until it reaches 10.95 at the depth of 87.6m. In

core 11MR1091, Al_2O_3 increases from 16.51 at 85 depth and increases to 19.28 at the depth of 89.7m, then drops steadily to 15.91 at the depth of 97.5m. Then the value remains relatively steady with a minor increase to 20.90 at the depth of 105.5m and again a minor drop to 19.28 at the depth of 106.6m.

Iron content behaves similarly in the two cores and increases steadily with depth with major fluctuations in core 11MR1001 (from 6.20 at the depth of 74.7 to 8.78 at the depth of 87.6m) with the lowest peak being at the depth of 76.6m at 4.13, and the highest peak at the depth of 81.3m at 9.53. In contrast in core 11MR1001, Fe_2O_3 values fluctuate slightly from 8.57 at the depth of 85m to 9.66 at the depth of 106.6m, with the lowest peak being at the depth of 89.7m at 89.7m and the highest peak at the depth of 105.5m at 10.85m.

In contrast to iron, Manganese shows different behaviour in two cores. In core 11MR1001 MnO is below 0.1 in the entire core except for the depths of 76.6m and 87.6m where it reaches the values of 24.94 and 16.63 respectively. In core 11MR1091 MnO decreases steadily with depth, except for two sharp drops, with the values being 0.19 and 0.02 at the depths of 89.7m and 99.4m.

Potassium and Barium content follows a similar trend in both cores. In 11MR1001 at the depths, of 74.7m and 76.6m K_2O slightly decreases from 0.73 to 0 while Ba slightly increases from 252.62 to 302. At the depth of 79.8m, both values increase sharply at 3.6 and 1072, and then both values decrease steadily until the depth of 86.5m and then there is a sudden drop at the depth of 87.6m with the values being 0.03 and 283. On a similar note, in core 11MR1091, K_2O and Ba have a sudden increase from 1.36 and 808 at the depth of 85m to 3.71 and 5454.51 at the depth of 89.7. In deeper depths, the values of K_2O drop at a steady rate, to the value of the depth of 101.40m reaching the value of 1.69. Then the value increases to the value of 2.33 at the depth of 105.5m and then drops a little to 2.08 at the depth of 106.6m. Ba values drop suddenly to the value of 898.69 at the depth of 94. The values continue to drop at a steady rate to the value of 606.08 at the depth of 97.5m and they remain steady with minor fluctuations until the bottom of the core, where Ba reaches 584.15.

Magnesium and Calcium content both decrease with depth in core 11MR1001. The highest values of MgO are observed at the top of the core at a depth of 74.7m at 0.94 while the value of CaO, at the same depth, is at 0.08. At the depth of 76.6m, there is a sudden increase of CaO reaching the value 0.11, and a sudden decrease of MgO at 0.08. MgO increases at 0.36 at the depth of 79.8m and then it decreases at a steady pace until the depth of 87.6m at 0.05. In

contrast in core 11MR1091 CaO increases with depth. From the depth of 85m to the depth of 97.5m, the values increase from 0.05 to 0.07 while at the depth of 99.4m, the values increase to 0.11 and then remain steady with minor fluctuations until the depth of 106.6m at 0.10.

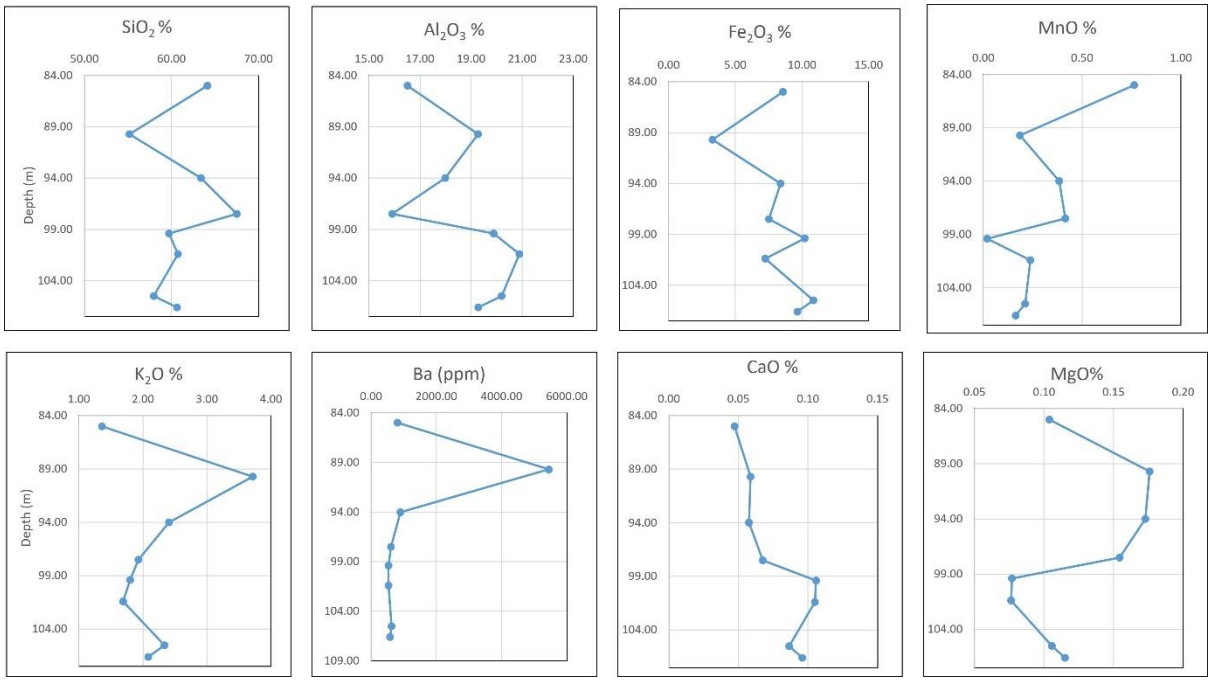

Figure 17: Chemostratigraphic diagrams of core 11MR1091.

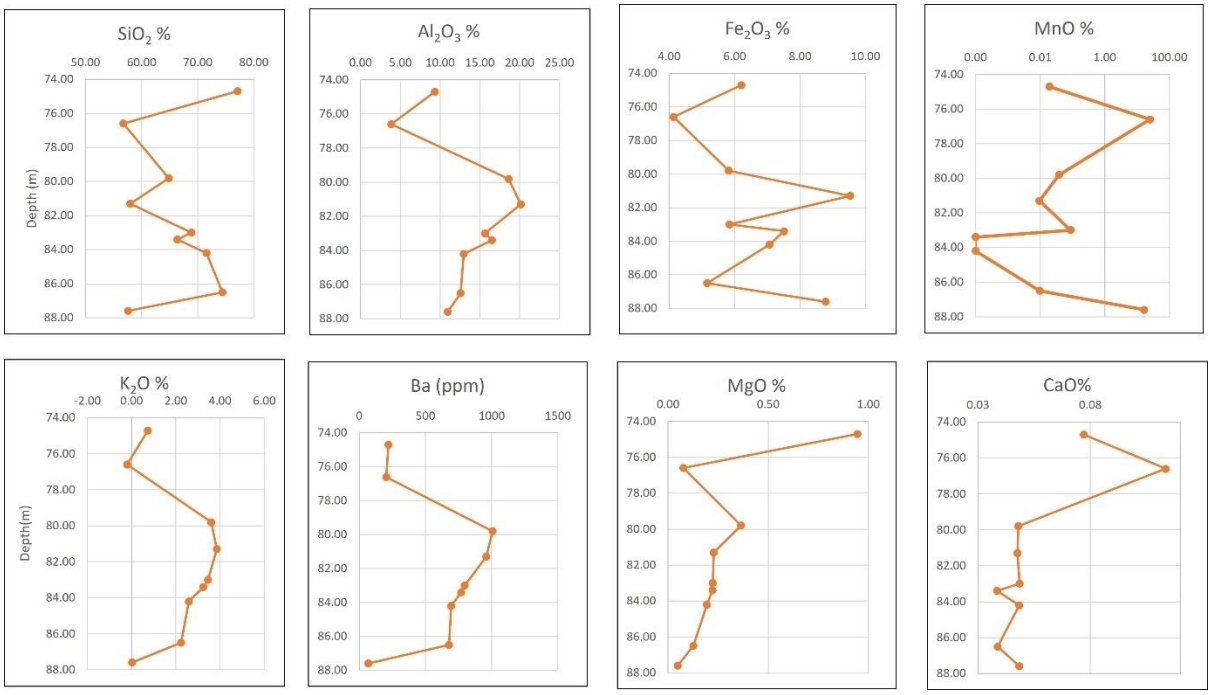

Figure 18:Chemostratigraphic diagrams of core 11MR1001.

4.5 Ce_{sn}/Ce_{sn} anomaly.

By plotting the Ce_{sn}/Ce_{sn}* to Pr_{sn}/Pr_{sn}* variation diagram proposed by (Bau & Dulski, 1996), in Figure 19b it is clear that the majority of the Ce anomalies are real and not affected by the anomalous behaviour of La except samples 11MR1001(74,7m) 11MR1001(83m) 11MR1001(83.4m) that present negative La anomaly and sample 11MR1001(87.6m) that presents positive La.anomaly. The rest of the core samples, present either positive, negative, or no Ce anomaly, while no La anomaly was detected in the rest of the samples. Positive Ce anomalies are considered at values above 1.10, as negative ones were considered anomalies with values below 0.90, while the values between 0.90 and 1.1 were considered to be without a Ce anomaly.

Ce behaves differently in each core and Ce anomaly presented different patterns with depth. In core 11MR1091, Ce decreases with increasing depth. In the upper parts of the core depths 85m, 89.7m, and 94m Ce anomaly appear positive with the values being 2.21, 1.73, and 2.53. In the lower part of the core, from the depth of 94m to 106.6m the Ce anomaly drops sharply, and negative values are found. The values minorly fluctuate from 0.56 to 0.65 with the lowest peak at 0.30 at the depth of 99.4m and the highest peak at 0.89 at the depth of 105.5m.

In contrast, on the whole in core 11MR1001 Ce anomaly appears as negative or non-existent and decreases with increasing depth, except in one sample at the depth of 81.3m, where Ce appears to be positive with the value being at 1.21. From the depth of 74.7m to 76.6m Ce anomaly decreases from 0.97 to 0.78 and remains steady until the depth of 79.8m. From the depth of 83m to 83.4m, the values are 0.94 and 0.98. At the depth of 84.2m the value suddenly dropped to 0.24 increased steadily to 0.57 at the depth of 86.5m and finally at 1.08 at the depth of 87.6m.

In core 11MR2014 Ce anomaly shows variation. At the top of the core at 69.9m the value is detected at 1.16, it drops sharply at 0.86 at 73m and it increases at 1.02 at 75.4. In core 11MR1094 the values are positive with the values being 4.42 at 64.4m and 1.75 at 73.5m (Figure 19a).

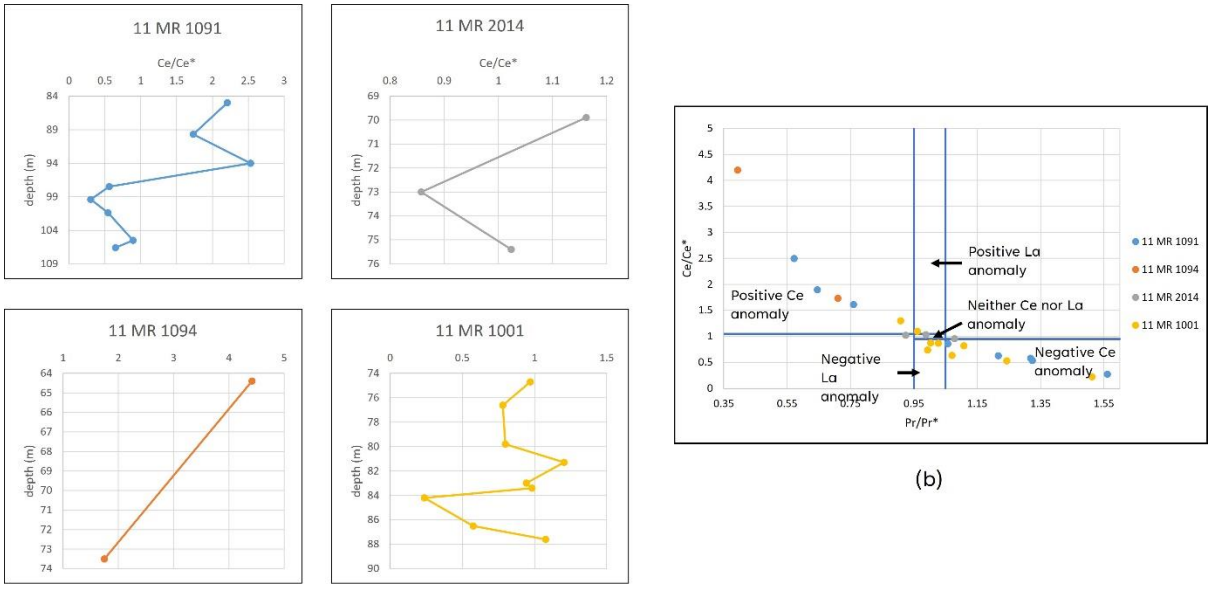

Figure 19: (a) Chemostratigraphy of Ce anomaly of cores 11MR1091, 11MR2014, 11MR1094, and 11MR1001 (b) Ce/Ce* and Pr/Pr* variation diagram *(Bau & Dulski, 1996).*

5 Discussion

5.1 Paleoweathering conditions.

5.1.1 Alteration indexes: Chemical Index of Alteration (CIA), Mafic Index of Alteration (MIA), and Index of Lateralization (IOL)

All the values present values that range from intermediate weathering to strong weathering for both CIA and MIA indexes, with the values being 68.93-98.65 and 77.43-99.06 respectively, indicating the strong present paedogenetic minerals and kaolinite inside the rock samples. The CIA index tracks the dissolution of feldspar and release of Ca, Na, and K in contrast to Al (H. W. Nesbitt et al., 1996). MIA index is an extension of CIA that includes Mg and Fe and tracks the loss of Mg in mafic minerals.(Babechuk et al., 2014).

In core 11MR1001, the samples appear to be mostly intermediate weathered except samples in the depths 74.7m, 76.6m, and 87.6m with the values being 89.13, 86.94, and 99.06. In the rest of the core, the values fluctuate minorly with the values being from 79.63 to 81.31 at the depths from 81.3m to 84.2, and the lowest value being recorded at the depth of 83 at 77.43. The MIA follows a very similar trend to the CIA, with the values recorded being lower. The strongly weathered values are reported at the depths of 76.6m and 86.7m at 89.38 and 98.65. In the rest of the core, the value increases with the depth with fluctuations from 79.03 to 83.18 at the depths from 74.7 to 86.7 (Figure 20a)

At core 11MR1091, CIA and MIA indexes follow again a similar trend with each other. CIA shows that all samples are intermediate weathered while MIA shows the same except sample 99.4m which is reported as strongly weathered. From depths 85m to 97.5m both increase from 78.8 and 82.01 to 81.29 and 83.84m respectively, with a small fluctuation at the depth of 94m where the CIA value increased to 82.22 and MIA value dropped at 82.25. At the of 99.4m, both values have their highest peaks, CIA at 84.7 and MIA at 86.10. Then the values drop steadily until the depth of 106.6m at 80.4 and 83.6m (Figure 20a).

MIA and CIA show a very good correlation with each other (r^2=0.6245) confirming the similar bulk behaviour of Ca, Na, and Mg (Figure 20b).

The IOL for samples is below 40 and ranges from 12.35 to 38.45, indicating that none of the samples were subjected to the lateritic profile that is recorded in the upper parts of the Mathews Ridge mineralization (Figure 20b).

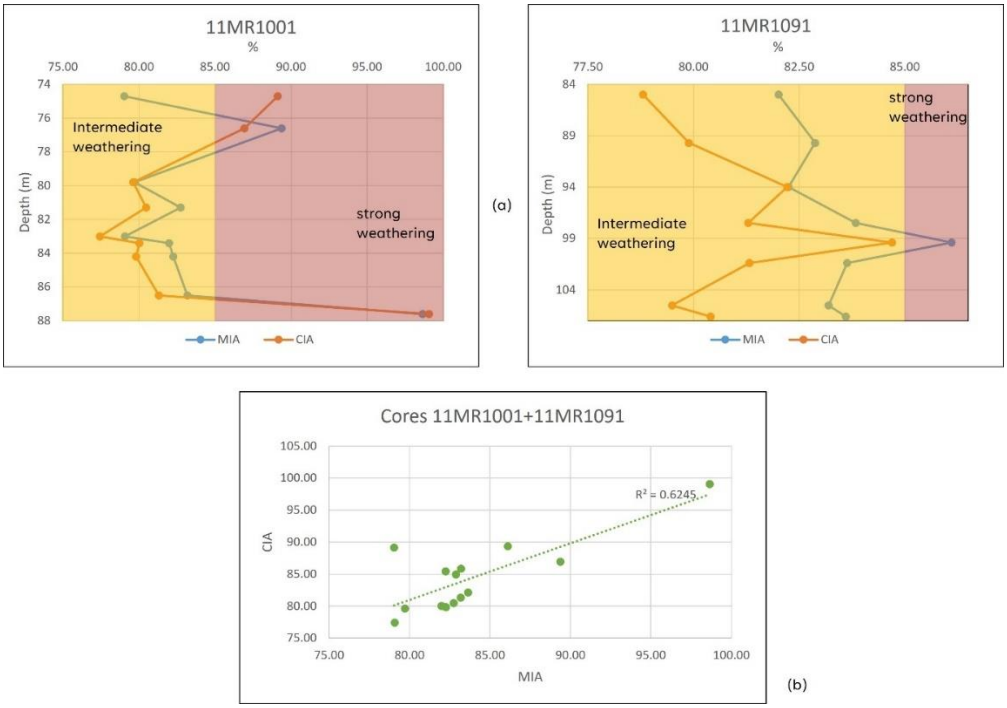

Figure 20: (a) MIA and CIA indexes stratigraphy of cores 11MR1001 and 11MR1091, (b) CIA MIA variation diagram.

5.1.2 A-CN-K, S-A-F, AF-CNK-M, A-L-F diagrams.

The SAF diagram is created with a mass fraction of SiO_2, Al_2O_3, and Fe_2O_3, while also the Index on lateralization is plotted to highlight the degree of lateralization, due to later tropical weathering that the samples had gone under. None of the samples appear to be lateralized, although samples from cores 11MR1001, 11MR2014, and 11MR1091 appear to be on the kaolinized part of the diagram (Figure 21a). The A-CN-K diagram is created with the molar

fractions of Al_2O_3, CaO Na_2O, and K_2O and it showed the chemical weathering and removal of CaO+Na_2O with increasing Al_2O_3 content while also K_2O in enriched inside the rock samples. All the samples are plotted between the Kaolinite-Illite/Muscovite line of the diagram, and one sample is plotted on the smectite/ Kaolinite line of the diagram (Figure 21b).

The ALF diagram studies the weathering trends in an oxidative environment and shows that Ca, Na K, and Mg weathering have similar behaviour, while the samples are being enriched in Al and then they are shifted towards the Fe end as the iron content increases (Figure 22b).

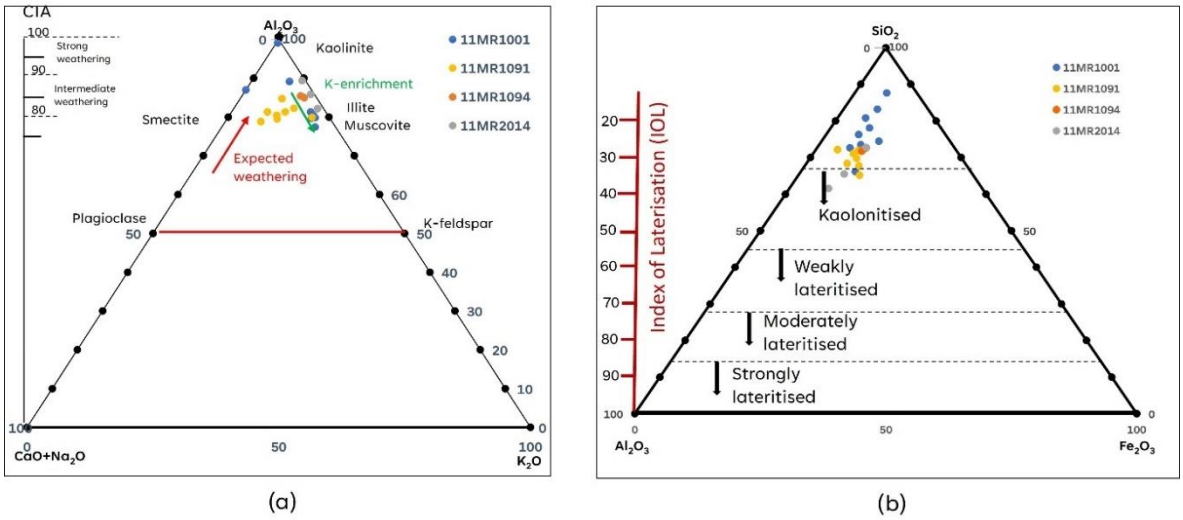

Figure 21: (a) Molar Al_2O_3-CaO+Na_2O-K_2O (A-CN-K) and (b) mass SiO_2-Al_2O_3-Fe_2O_3 (SAF) ternary plots illustrating the different degrees of alteration as seen between the 11MR core samples. The chemical index of alteration (CIA) and index of lateralization can both be included in the A-CN-K and SAF plots ternary as shown.

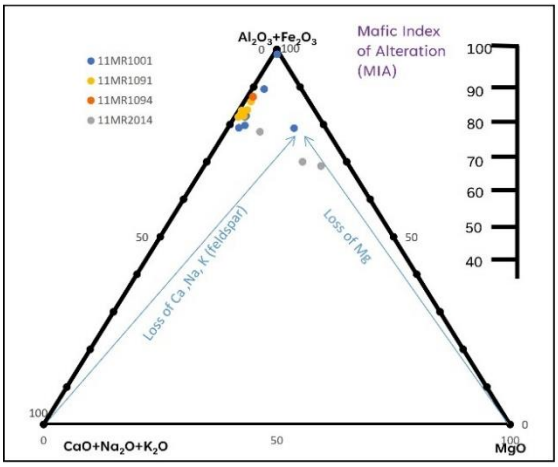

Figure 22: Molar ternary plots in Al-Fe-Ca-Na-K. The A-CNKM-F (ALF) *(Babechuk et al., 2014; H., & Y. G. M. Nesbitt, 1982)* diagram exposes the contribution of the mafic and felsic mineral components to rock weathering. The integration of the new mafic index of alteration (MIA) is illustrated; while the A–L–F and AF–CNK–M plot is integrated with the MIA for studying oxidative weathering trends.

5.2 Preservation state of weathering and tectonics.

The Phyllite rocks of the lower phyllite unit of the Matthews Ridge deposit were deposited at around 2097±39 Ma-2238±81 Ma (Carvalo & Cousens, 2022). The Serra do Navio Mn deposit (2.11 Ga; Voicu et al., 2001) and the Nsuta deposit (2.2 Ga Albani et al., 2010; El Albani et al., 2014) were also deposited during this period. Mn deposition occurred during the event of the Trans-Amazonian orogeny. The rocks in these areas were metamorphosed up to greenschist facies(Kroonenberg et al., 2016). The metapelitic rocks in these areas include the phyllite rocks of Matthews Ridge (Goulet, 2012), the biotitic and graphite schists of the Serra do Navio deposit (Chisonga et al., 2012), and the Mn-phyllites of the Nsuta deposit (Nyame, 2008).

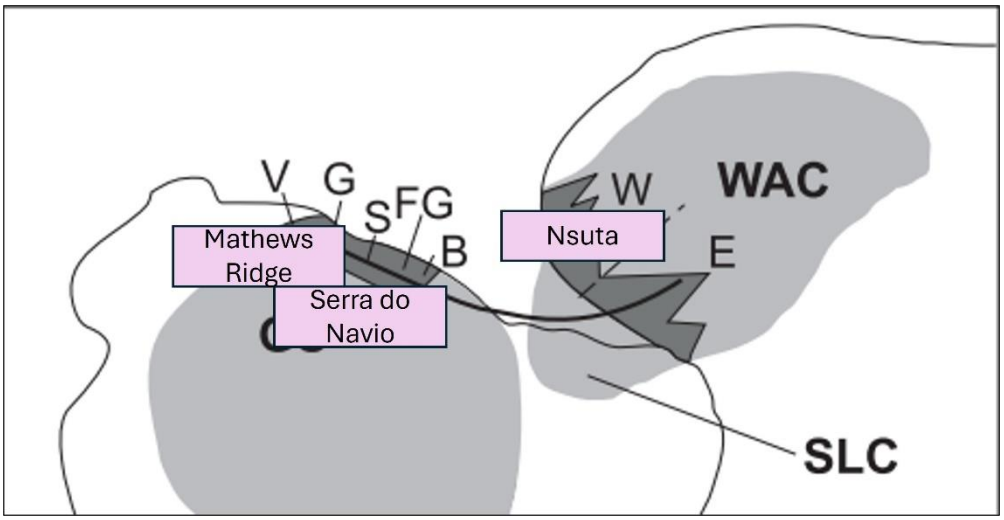

Figure 23: Recreation of the tectonical setting between the Guyana Shield and West African Craton. In the schematic the proximity between the Mathews Ridge, Nsuta and Serra do Navio deposits are highlighted (modified from Leube et al., 1990).

The Matthews Ridge has been subjected to intense tectonic activity. This tectonic activity according to (Westerman,1969) is controlled by regional block faulting. Relative movement between the basement blocks gave the effect of a recumbent fold, considered to be related to the main folding stresses, southwest of Matthews Ridge. This is folded by compression tectonics that have resulted due to the southward tilting of the Barima river basin block. Gravitational compression was directed into a funnel-shaped area followed by basement scraps. This resulted in domal structures in the Matthews Ridge area and a consequent rare type of major drag faulting. Regarding the regional tectonic activity, Matthews Ridge has also been subjected to local smaller-scale tectonic activity as seen in the petrographical observations, which makes the distinction between the tectonic activities very hard.

The tectonic impact of the area is also seen in the nature of the phyllites and the presence of certain minerals. The strongest weathered samples are correlated with the presence of kaolinite and in core 11MR1001 secondary Mn-oxide mineralization is observed, parallel to the plain schistosity of the phyllites. In addition, the strongly weathered samples also show fault presence and correlate with the presence. of mylonites All the samples of core 11MR1001, are affected by tectonic activity indicated by petrographic observations of mylonite structures in the samples. The activity could be characterized as microtectonic activity since in all thin sections small faults are found indicated by the presence of a mylonitic pattern. The least weathered samples are characterized by the presence of muscovite +chlorite+ quartz. Illite crystals are always found in thin sections affected by tectonism and most of the samples are part of the mylonite mix. Illite formed by later weathering of muscovite reflected by the low K_2O, CaO, MgO, and Na_2O content Subsequently, kaolinite in faults was formed by leaching of K_2O. Also, the Al-illite-hydromica occurs which is a low K_2O variety of muscovite with high H_2O, suggesting a higher degree of depletion of K_2O (Figure 21). The CIA and MIA indexes suggest that mobile elements have been leached out of the system due to weathering. A-CN-K indicates the removal of $CaO+Na_2O+K_2O$ while being enriched in Al_2O_3MgO is leached out of the system, while being enriched in Al_2O_3 and Fe_2O_3, proven by the presence of Fe-rich chlorites.

During the time of the Trans-Amazonian orogeny (2.26-1.98 Ga), the West African craton was southwardly subducted below the Guyana Shield (Leube et al., 1990). By using the Th-Sc-Zr/10 and La-Th-Sc triangular diagrams provided by Bhatia & Keith AW Crook (1986) can be used as indicators that the LPHY was accumulated in continental arc/ocean island arc environment (Figure 25a, b). This is aligned with the tectonic depositional setting of the area. In contrast to the Matthews Ridge deposit, the Serra do Navio deposit was deposited in an active continental margin (Chisonga et al., 2012).

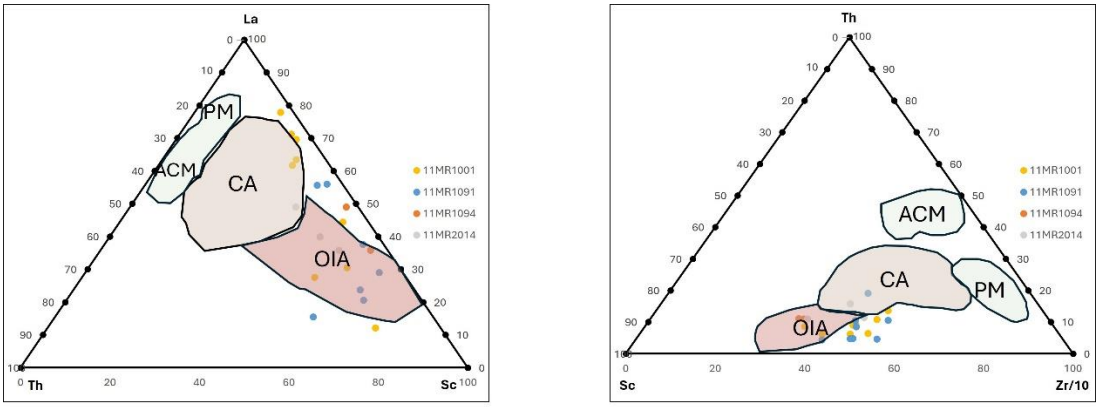

Figure 24: Tectonic features of the depositional environment of Matthews Ridge.

The low mobility of a few REEs and major elements of sediments create useful indicators to trace the sedimentary provenance (Taylor & McLennan 1985). Felsic rocks are richer in both La and Th and poorer in Sc, Cr, and Co in contrast to mafic rocks, the La/Sc, Th/Co, Th/Sc, and Cr/Th ratios are good indicators of uncovering the source rock of the sediments (Condie, 1993; Cullers, 1994; Matthew W. Totten et al., 2000). By comparing these ratios, the Matthews Ridge metasediments appear to show a mafic and ultramafic source rock. The mafic nature of the volcanic rocks of the Mazaruni Group (Kroonenberg et al., 2016) area suitable source rock for the basal phylltic unit of the Matthews Ridge deposit (Figure 25a-c).

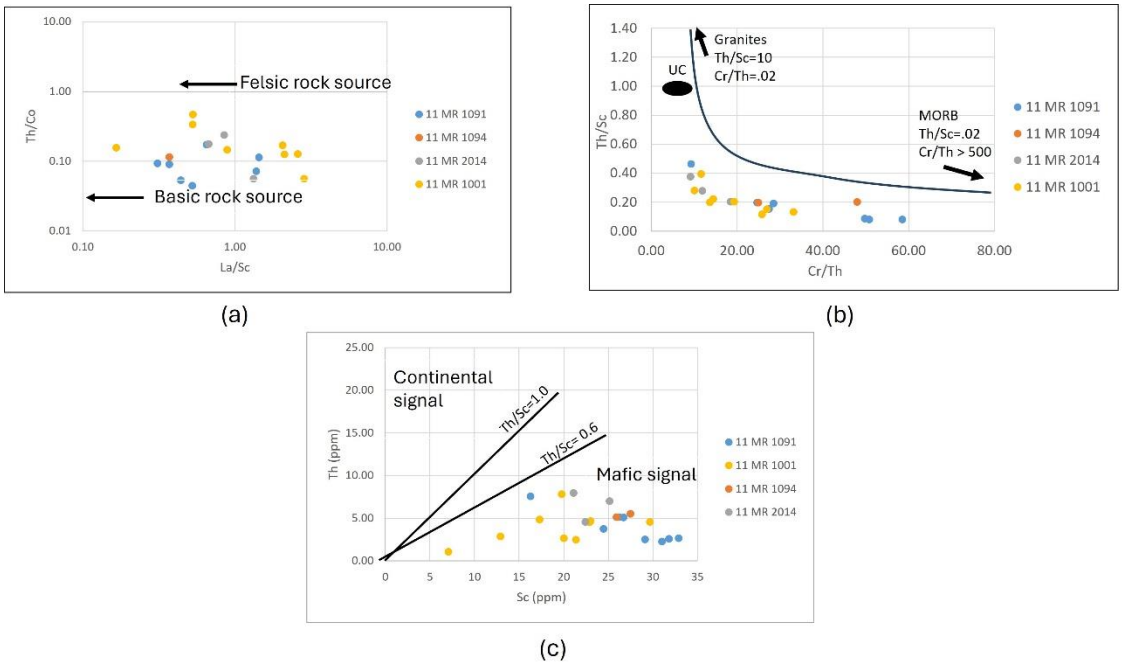

Figure 25: Source rock diagrams of the metapiletic sediments of the LPHY unit (a) (Cullers, 1994), (b) (Condie, 1993), (c)(Matthew W. Totten et al., 2000).

By comparing the data of the Nsuta and Serra do Navio deposit it can also be seen that the Serra do Navio graphite and biotite schist contain a similar mafic mixed with felsic volcanic source rock originating from the Jornal Formation (Chisonga et al., 2012). This highlights the similar compositions of the greenschist belts of the Guyana Shield and the exogenetic influences that resulted in the weathering of the mafic volcanic rocks of the Barama-Mazaruni and Villa Nova Supergroups. In contrast to the Guyana deposit, the Mn-phyllites of the Nsuta deposit have a felsic rock source signature.

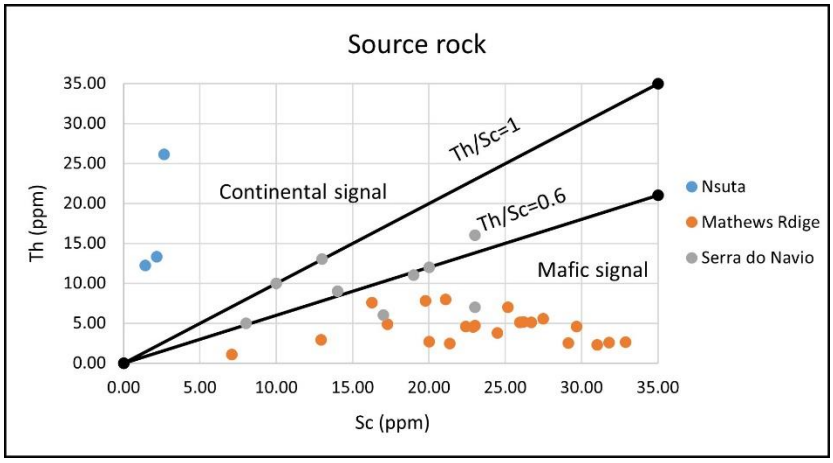

Figure 26: Source rock comparison of the metapiletic rocks between Mathews Ridge, Nsuta, and Serra do Navio.

By using the Pb/Zn and Co+ Ni/As+ Pb+ Zn+ Ni+ Cu diagrams provided by Nicholson, (1992), it appears that the mafic weathered terrigenous metasediments of the LPHY unit were deposited in a freshwater shallow marine environment (Figure 27a-b) in contrast to the Nsuta and Serra do Navios deposits that were accumulated in a marine environment (Figure 28a-b).

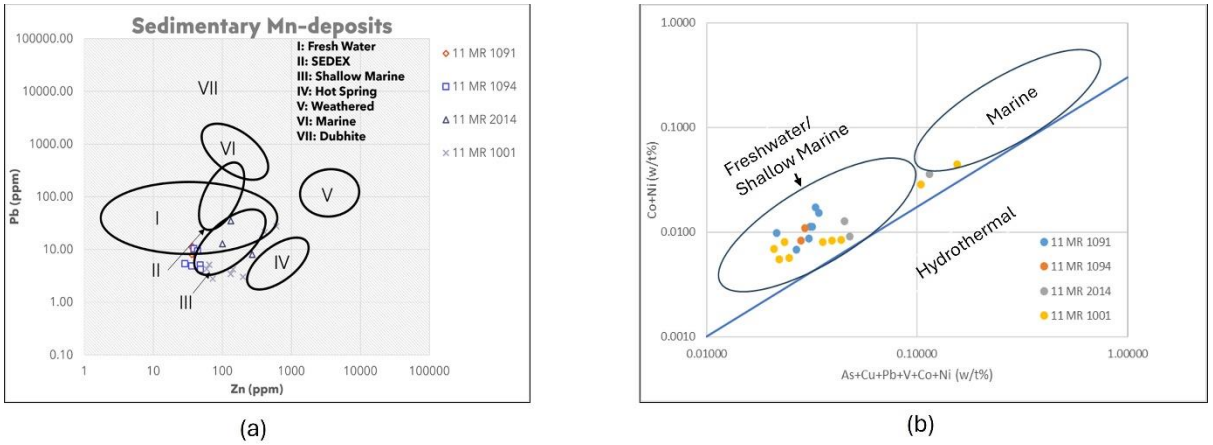

Figure 27: Depositional environment of the LPHY(Nicholson, 1992).

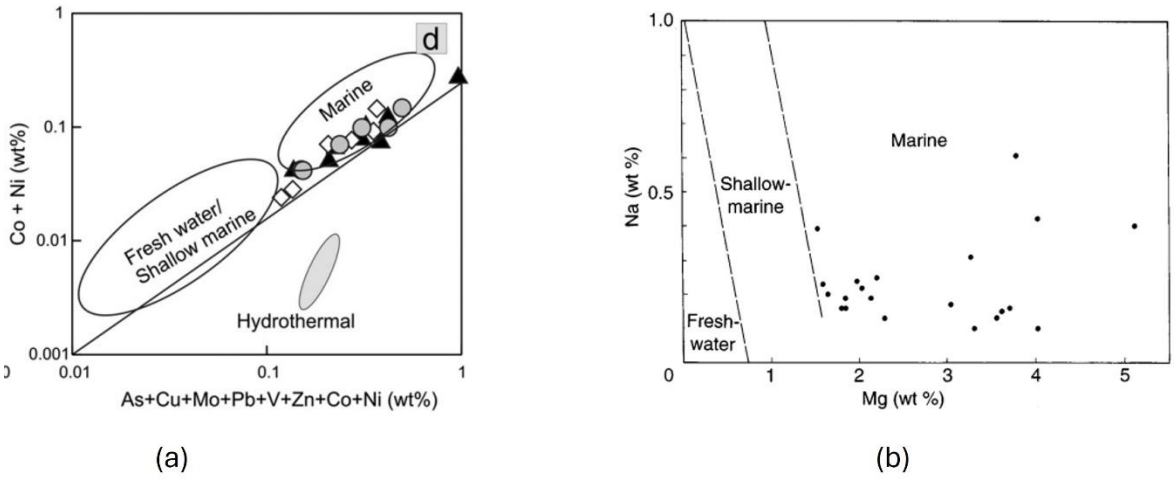

Figure 28a) Depositional environment of Serra do Navio deposit (Chisonga et al., 2012), (b) Depositional environment of the Nsuta deposit.

There are similarities between their major elements oxide. The trend of the silica, titanium, aluminum, and iron content of the rocks is similar for the phyllitic rocks of the Matthews Ridge deposit, the Nsuta deposit and Serra do Navio. Matthews-Ridge and Serra do Navio have similar SiO_2 content that ranges from 48 wt.% to 77 wt.% and from 43 wt.% to 79 wt.%, respectively. Nsuta records the lowest SiO_2 values at 24.4-47.2 wt.%. TiO_2 is also similar for both reaching up to 1 wt.% and for the Nsuta reaching up to 0.41 wt.%. Al_2O_3 varies between the three rock units. The Matthews Ridge records the highest one with 3.86-23.97 wt.% Al_2O_3, followed by the Serra do Navio at 4.617.9 wt.% Al_2O_3 and the Nsuta at 8.8-11.8 wt.% Al_2O_3. Matthews Ridge and Nsuta phyllites have similar Fe_2O_3 content of 3.28-10.85 wt.% while Serra do Navio has a higher iron content of 2.6-19.2 wt.%. The changing trend of MnO, MgO, and CaO reflects the abundance of carbonate minerals inside the rock units. The Nsuta phyllites have the highest values of MnO, MgO, and CaO of respectively 1.5618.6 wt.%, 2-18 wt.%, and 0.939.65 wt.%. Both Mathews Ridge phyllites and Serra do Navio schists are depleted in these components, with the values being 0%-3.11% for MnO, 0.05-2.97% for MgO, and 0.03%-0.11% for CaO and 0.08%-4.37% for MnO, 0.7-4.5% MgO and 0.7%-4.2% CaO respectively. K_2O content is low in all rock units. e. in Serra Do Navio and Matthews Ridge it is less than 4.9 wt, %, and in Nsuta it reaches up to 1.18 wt.%. Serra do Navio appears to have the highest amount of Na_2O with values up to 4 wt.%, while for Mathews Ridge the values reach up to 1.18 wt.%, and for the Nsuta 2.2 wt.%. Lastly, for all rock units the P_2O_5 content is almost negligible with the value being less than 0.1 wt.% for both Mathews Ridge and Serra do Navio, and less than 0.42 wt.% for Nsuta. The major components of the rock units are presented in Figure 29.

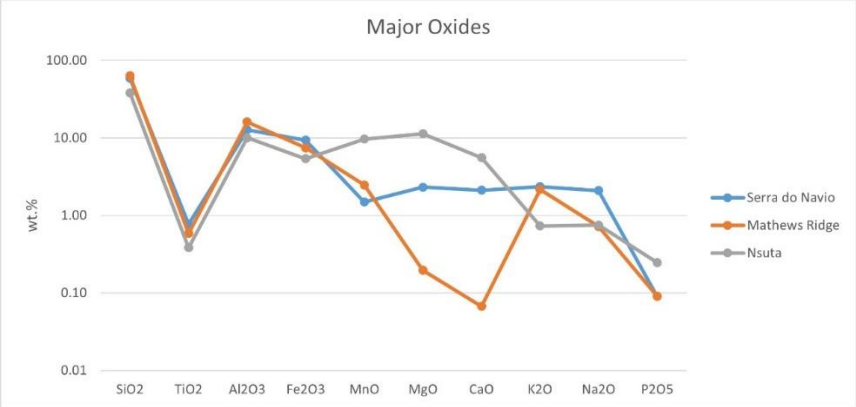

Figure 29: Major oxide plot of Mathews Ridge, Serra do Navio, and Nsuta metapelitic rock units.

The similarities between the host rocks of the deposits can also be seen when comparing the REE+Y patterns (Figure 24). All phyllitic rocks present positive Eu and Y anomalies and relatively flat REE+Y patterns similar to the UCC, where the LREE has a similar concentration relative to the HREE. The Serra do Navio schists and Matthews Ridge phyllites present a very similar REY pattern with approximately similar concentrations. In contrast, the Nsuta Mn-phyllites are enriched in the LREE relative to HREE.

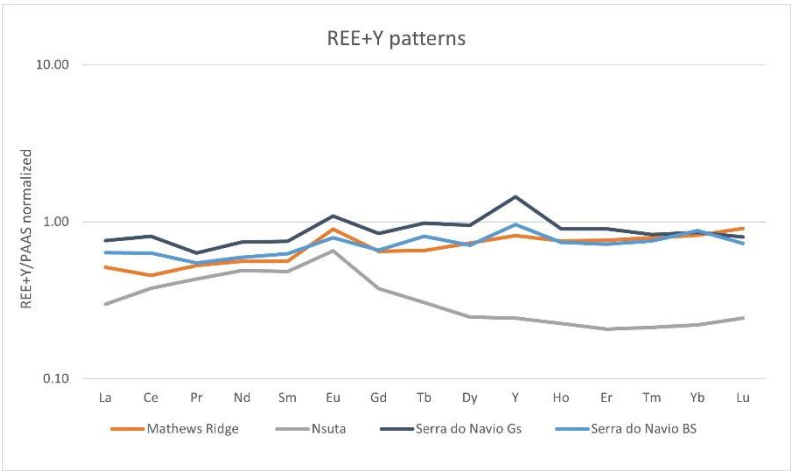

Figure 30:REE+Y patterns of Mathews Ridge, Nsuta and Serra do Navio.

Another difference that is observed in the REE+Y patterns is the negative Ce anomaly of the Matthews Ridge LPHY unit in contrast to the positive Ce anomaly in the Nsuta Mn-phyllites, and Serra do Navio graphite and biotite schists.

5.3 Redox state of the oxidative environment.

Both negative and positive Ce anomalies are closely associated with the oxidation of Mn^{2+} given their similar reduction potentials (Ederfield H., 1988). The oxidation of soluble Ce^{3+} to Ce^{4+} is catalyzed on top of Mn oxyhydroxides/oxides and immobilization of Ce^{4+} occurs

on top of particulate Mn oxides. (Takahashi et al., 2002). Cerium oxidation can also happen on the surface of Fe^{3+} oxyhydroxide/oxides (Bau, 1999; Bau & Koschinsky, 2009), but evidence for this phenomenon is less consistent than the adsorption on Mn oxyhydroxides/oxides surfaces. (Loges et al., 2012). Negative Ce anomalies are generated when the amount of available oxygen in the system is enough to drive the oxidation of Ce^{3+} to Ce^{4+}. Positive Ce anomalies in seawater occur when the O_2 concentration is enough to facilitate the oxidation Ce from the trivalent to the tetravalent state in surface waters, but due to the oxygen stratification of the water column, the lower part of the water column is O_2 limited (Tostevin, Shields, et al., 2016b; Tostevin, Wood, et al., 2016) Sinking oxidized Ce particles in the anoxic/suboxic zone results in the reduction of the now unstable Ce^{4+} and Mn and Fe oxides oxyhydroxides/ hydroxides (Ostrander et al., 2019; Tostevin, Shields, et al., 2016b).

The LPHY unit of the Matthews ridge contains both negative and positive Ce anomalies, with the average Ce anomaly being negative. Core 11MR1091 presents negative anomalies at the lower and deeper part of the core while the upper parts of the core present positive Ce values. This indicates a relatively oxidizing and reducing depositional environment.

The LPHY unit is characterized by a low percentage of MnO with local impure Mn beds and cherts (Goulet, 2012). The two core samples have different percentages of Mn available. In core 11MR1001 MnO is below 0.1 wt.% except for two samples that present secondary Mn-oxides mineralization. The MnO in core 11MR1091 is lower but still higher than the core 11MR1001 ranging from 0.02-0.76 wt.%. Thus, core 11MR1091 is more suitable for investigating the controls of Ce anomaly. In addition, core 11 MR1001 is heavily impacted by intense tectonic activity and weathering, since every sample has mylonite inside, in contrast to core 11MR1091, which is less tectonically impacted and less samples present strong weathering features. By removing samples 11MR1091(94m) and 11MR1091(99.4m) and comparing the Ce/Ce* with MnO% and Mn/Fe ratio, it can be seen that the MnO% shows a weak correlation with the Ce anomaly (r^2=0.32) (Figure 31a) and a stronger correlation with Mn/Fe ratio (r^2=0.61) (Figure 31b). This reflects the oxidative scavenging of Ce on Mn-Fe oxides. This is further proven from mineral data where small monazite crystals can be identified on top of both Mn and Fe oxides.

The above observations must be used with attention. The tectonic nature of core 11MR1091 has not been thoroughly studied. Even though none of the samples have been

subjected to lateritic weathering the Mn and Ce recycling due to tectonic activity and tropical weathering is still a possibility that needs to be studied. Thus, the assumption that the Ce anomalies that are reflected in the results reflect the true depositional environment must be made.

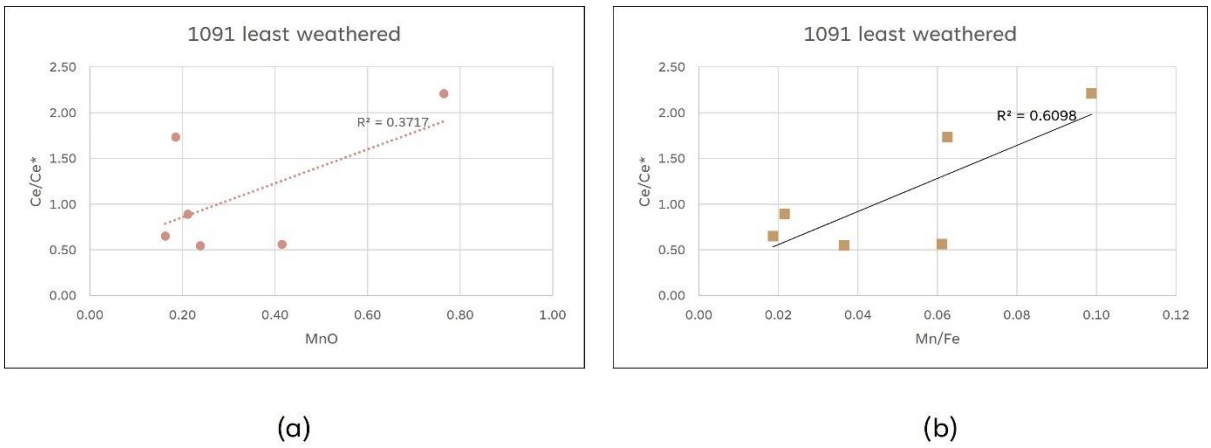

Figure 31: Ce anomaly variation diagrams (a) Correlation MnO (b) Correlation with Mn/Fe.

In Serra do Navio, the metaplectic rocks do not show a correlation with the MnO concentration but the Mn-carbonate rock samples fit well with the MnO proportion inside the carbonate rocks (Chisonga et al., 2012), and overall positive Ce/Ce* values supporting the presence of a oxic-anoxic environment. Similar to the Nsuta deposit positive Ce anomalies are detected in the Mn-ore samples whereas such anomalies are rarely observed in the Mn-phyllites (Goto et al., 2021). While Nyame (2008), reports negative or no Ce anomalies in the Nsuta Mn-carbonate.

5.4 Depositional model of the MPHY unit and the state of the Early-Paleoproterozoic Ocean.

By combining all the above results and comparing the metallogenic models of the Nsuta deposit (Nyame, 2008), the Serra do Navio deposit (Chisonga et al., 2012) and the Manganese stromatolites in Koegas Group, South Africa (Warke et al., 2020) a first assessment about the depositional model of Matthews Ridge can be made.

The Matthews Ridge metasediments are composed of terrestrial sediments that are more enriched in HREEs than LREEs, sediments with mafic/ultra-mafic signatures that probably originate from the mafic volcanic rocks of the Mazaruni group. By accepting the assumption that the Mn/Fe variability is controlled by variations that occurred in the depositional environment it is suggested that the sediments have been deposited in an oxygen

and redox stratified ocean in a continental /ocean island arc environment. The upper part of the ocean was oxygen efficient to facilitate the oxidation of soluble Mn^{2+}, above the Mn^{4+}/Mn^{2+} redoxcline, to insoluble Mn^{4+} oxides that catalyze the oxidation of Ce^{3+} (Bau, 1999) resulting in negative Ce anomalies. As the ocean basin was deepening due to the ocean stretching because of the Trans-Amazonian orogeny processes the sediments started to be deposited below the Mn^{4+}/Mn^{2+} where the amount of O_2 was insufficient, resulting in anoxic/suboxic conditions. The particulate oxides sink through the redox stratified waters, resulting in the reduction of Mn^{4+} oxides to Mn^{2+} oxides and consequentially resulting in the reduction of Ce^{4+} to Ce^{3+} and generating positive Ce anomalies (Tostevin, Shields, et al., 2016b). Even though MnO is low, it is still non-negligible because the Ce anomalies are positively correlated to Mn/Fe. This suggests redox cycling of these elements by the rise of oxygen in the atmosphere. In this model, the lower phyllitic unit has been deposited deeper in the basin just where the environment became reducing again, resulting in the transformation of Mn oxides into Mn^{2+} before reaching the sediment profile. Subsequently, the mobile Mn^{2+} is transported to shallower oxygenated water depths where conditions are favourable for Mn to be stored in sediments together with the scavenged Ce (need some references). If such is the case, we should find positive Ce anomalies in the Mn-enriched rocks higher up in the stratigraphy, which supports the hypothesis of the barren basal LPHY. With the Mn/Fe controlling the oxidation of Ce^{3+} it is suggested that the formation of Fe^{3+} oxyhydroxides along Mn redoxcline is related to the upward diffusion of Fe^{2+} due to O_2 consumption by Mn^{2+} oxidations and the following replacement of Mn^{4+} by Fe^{3+} in particulate Mn^{4+} oxides (Dellwig et al., 2010; Kurzweil et al., 2016).

The origin of Mn is still a mystery in most Early-Paleoproterozoic Mn deposits, most authors support that Mn originates from a subthermal volcanic activity supported by the high positive Eu anomalies and the enrichment of the Early Paleproterozoic ocean in Eu due to volcanic activity (Bau & Dulski, 1996) or a terrestrial source that was eroded and resulted to the Mn enrichment (Roy, 2006).

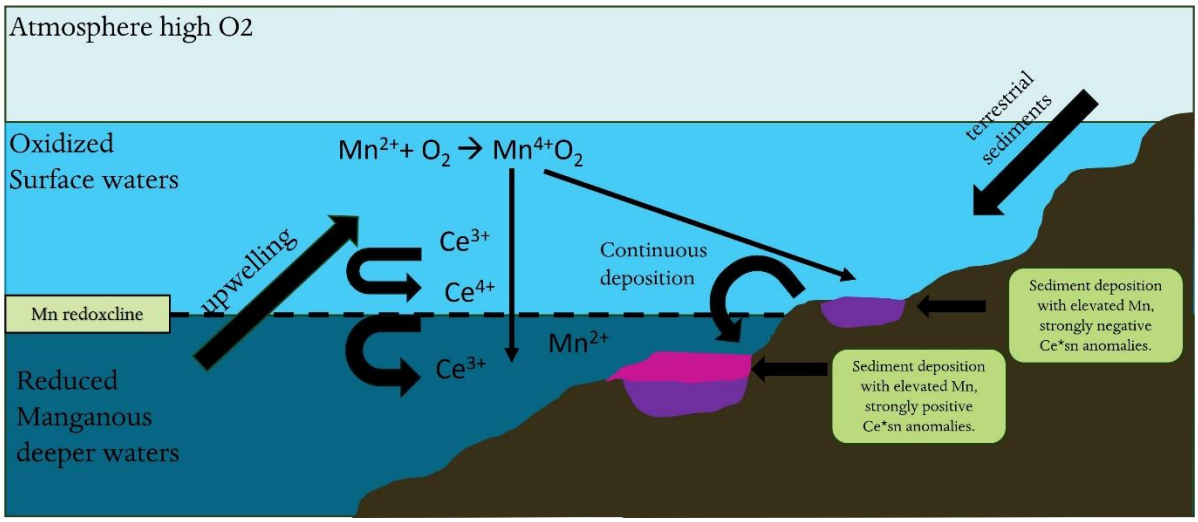

Figure 32: Depositional model of the LPHY unit (modified by Warke et al., 2020).

6 Conclusions

Summarizing, the Lower Phyllite Unit of the Matthews Ridge Unit is composed of moderately to strongly weathered terrestrial sediments with mafic signatures. It suggested that the sediments accumulated in a freshwater shallow-marine environment and an oxygen/redox stratified ocean, above the Mn4+/Mn2+ redoxcline, and, as the ocean basin was deepening the sediments were continuously deposited in a reduced environment below the Mn2+/Mn4+redoxcline. The sediments were later metamorphosed to greenschist facies because of the event of the Trans-Amazonian orogeny. Later tectonic activity and dioritic intrusions resulted in the creation of major fault units and folds in the entire stromatographic column, while due to tropical weathering, it was subjugated to lateritic weathering.

7 Reference

A. Karhu, H. D. H., & Heinrich D. Holland. (1996). carbon isotopes and the rise of atmospheric oxygen. *Geology*, *24*(10), 867–870.

Albani, A. El, Bengtson, S., Canfield, D. E., Bekker, A., Macchiarelli, R., Mazurier, A., Hammarlund, E. U., Boulvais, P., Dupuy, J.-J., Fontaine, C., Fürsich, F. T., Gauthier-Lafaye, F., Janvier, P., Javaux, E., Ossa, F. O., Pierson-Wickmann, A.-C., Riboulleau, A., Sardini, P., Vachard, D., … Meunier, A. (2010). Large colonial organisms with coordinated growth in oxygenated environments 2.1 Gyr ago. *Nature*, *466*(7302), 100–104. https://doi.org/10.1038/nature09166

Altermann, W., & Nelson, D. R. (1998). Sedimentation rates, basin analysis and regional correlations of three Neoarchaean and Palaeoproterozoic sub-basins of the Kaapvaal craton as inferred from precise U–Pb zircon ages from volcaniclastic sediments. *Sedimentary Geology*, *120*(1–4), 225–256. https://doi.org/10.1016/S0037-0738(98)00034-7

A.R Westerman. (1969). A structural analysis of Matthew Ridge Manganese Mine,. *N.W.D, Guyana for the 8th Guiana Geological Conference* , 1–32.

Babechuk, M. G., Widdowson, M., & Kamber, B. S. (2014). Quantifying chemical weathering intensity and trace element release from two contrasting basalt profiles, Deccan Traps, India. *Chemical Geology*, *363*, 56–75. https://doi.org/10.1016/j.chemgeo.2013.10.027

Bau, M. (1999). Scavenging of dissolved yttrium and rare earths by precipitating iron oxyhydroxide: experimental evidence for Ce oxidation, Y-Ho fractionation, and lanthanide tetrad effect. *Geochimica et Cosmochimica Acta*, *63*(1), 67–77. https://doi.org/10.1016/S0016-7037(99)00014-9

Bau, M., & Dulski, P. (1996). Premmbrinn Resenrth Distribution of yttrium and rare-earth elements in the Penge and Kuruman iron-formations, Transvaal Supergroup, South Africa. In *Precambrian Research* (Vol. 79).

BAU, M., & KOSCHINSKY, A. (2009). Oxidative scavenging of cerium on hydrous Fe oxide: Evidence from the distribution of rare earth elements and yttrium between Fe oxides and Mn oxides in hydrogenetic ferromanganese crusts. *GEOCHEMICAL JOURNAL*, *43*(1), 37–47. https://doi.org/10.2343/geochemj.1.0005

Beukes, N. J. ,. (1993). A review of manganese deposits associated with the early Proterozoic Transvaal Supergroup in Northern Cape Province, South Africa. *16th International Colloquium on African Geology*, 37–38.

Bhatia, M. R., & Keith AW Crook. (1986). Trace element characteristics of graywackes and tectonic setting discrimination of sedimentary basins. *Contributions to Mineralogy and Petrology*, *92*(2), 181–193.

Bolhar, R., Kamber, B. S., Moorbath, S., Fedo, C. M., & Whitehouse, M. J. (2004). Characterisation of early Archaean chemical sediments by trace element signatures. *Earth and Planetary Science Letters*, *222*(1), 43–60. https://doi.org/10.1016/j.epsl.2004.02.016

BOLHAR, R., & VANKRANENDONK, M. (2007). A non-marine depositional setting for the northern Fortescue Group, Pilbara Craton, inferred from trace element geochemistry of stromatolitic carbonates. *Precambrian Research*, *155*(3–4), 229–250. https://doi.org/10.1016/j.precamres.2007.02.002

Buick, I. S., Uken, R., Gibson, R. L., & Wallmach, T. ,. (1993). . High δ13C Paleoproterozoic carbonates from the Transvaal Supergroup, South Africa. *Geology*, *26*, 875–878.

Calvert, S. E., & Pedersen, T. F. (1993). Geochemistry of Recent oxic and anoxic marine sediments: Implications for the geological record. *Marine Geology*, *113*(1–2), 67–88. https://doi.org/10.1016/0025-3227(93)90150-T

Calvert, S. E., & Pedersen, T. F. (1996). Sedimentary geochemistry of manganese; implications for the environment of formation of manganiferous black shales. *Economic Geology*, *91*(1), 36–47. https://doi.org/10.2113/gsecongeo.91.1.36

Capdevila, R. , A. N. , L. J. , & S. J. F. (1999). Diamonds in volcaniclastic komatiite from French Guiana. *Nature*, *399*(6735), 456–458.

Carvalo, B., & Cousens, B. L. (2022). PETROLOGY, GEOCHEMISTRY, AND U-PB GEOCHRONOLOGY OF MAFIC AND ULTRAMAFIC ROCKS OF NW GUYANA, GUIANA SHIELD, SOUTH AMERICA. *Goldschmidt.*

Catling D.C., Zahnle K.H., & McKay C.P. (2001). Biogenic methane, hydrogen escape, and the irreversible oxidation of early Earth. *Science*, *293*, 839–843.

Chisonga, B. C., Gutzmer, J., Beukes, N. J., & Huizenga, J. M. (2012). Nature and origin of the protolith succession to the Paleoproterozoic Serra do Navio manganese deposit, Amapa Province, Brazil. *Ore Geology Reviews*, *47*, 59–76. https://doi.org/10.1016/j.oregeorev.2011.06.006

Choudhuri, A. (1980). The early proterozoic greenstone belt of the northern Guiana Shield, South América. *Precambrian Research*, *13*(4), 363–374.

Condie, K. C. (1993). Chemical composition and evolution of the upper continental crust: Contrasting results from surface samples and shales. *Chemical Geology*, *104*(1–4), 1–37. https://doi.org/10.1016/0009-2541(93)90140-E

Cullers, R. L. (1994). The controls on the major and trace element variation of shales, siltstones, and sandstones of Pennsylvanian-Permian age from uplifted continental blocks in Colorado to platform sediment in Kansas, USA. *Geochimica et Cosmochimica Acta*, *58*(22), 4955–4972. https://doi.org/10.1016/0016-7037(94)90224-0

Dellwig, O., Leipe, T., März, C., Glockzin, M., Pollehne, F., Schnetger, B., Yakushev, E. V., Böttcher, M. E., & Brumsack, H.-J. (2010). A new particulate Mn–Fe–P-shuttle at the redoxcline of anoxic basins. *Geochimica et Cosmochimica Acta*, *74*(24), 7100–7115. https://doi.org/10.1016/j.gca.2010.09.017

Delor, C. L. D. E. E. L. J.-M. C. A. G. C. de A. V. (2003). Transamazonian crustal growth and reworking as revealed by the 1:500,000-scale geological map of French Guiana. *Géologie de La France*, *5*(57), 2–4.

Dixon, C. J. (1979). The Nsuta Manganese Deposit — Ghana. In *Atlas of Economic Mineral Deposits* (pp. 20–21). Springer Netherlands. https://doi.org/10.1007/978-94-011-6511-2_6

Ederfield H. (1988). The oceanic chemistry of the rare-earth elements. *Philosophical Transactions of the Royal Society of London. Series A, Mathematical and Physical Sciences*, *325*(1583), 105–126. https://doi.org/10.1098/rsta.1988.0046

El Albani, A., Bengtson, S., Canfield, D. E., Riboulleau, A., Rollion Bard, C., Macchiarelli, R., Ngombi Pemba, L., Hammarlund, E., Meunier, A., Moubiya Mouele, I., Benzerara, K., Bernard, S., Boulvais, P., Chaussidon, M., Cesari, C., Fontaine, C., Chi-Fru, E., Garcia Ruiz, J. M., Gauthier-Lafaye, F., … Bekker, A. (2014). The 2.1 Ga Old Francevillian Biota: Biogenicity, Taphonomy and Biodiversity. *PLoS ONE*, *9*(6), e99438. https://doi.org/10.1371/journal.pone.0099438

Eriksson, P. G., Condie, K. C., Tirsgaard, H., Mueller, W. U., Altermann, W., Miall, A. D., Aspler, L. B., Catuneanu, O., & Chiarenzelli, J. R. (1998). Precambrian clastic sedimentation systems. *Sedimentary Geology*, *120*(1–4), 5–53. https://doi.org/10.1016/S0037-0738(98)00026-8

German, C. R., & Elderfield, H. (1990). Application of the Ce anomaly as a paleoredox indicator: The ground rules. *Paleoceanography*, *5*(5), 823–833. https://doi.org/10.1029/PA005i005p00823

German, C. R., Holliday, B. P., & Elderfield, H. (1991). Redox cycling of rare earth elements in the suboxic zone of the Black Sea. *Geochimica et Cosmochimica Acta*, *55*(12), 3553–3558. https://doi.org/10.1016/0016-7037(91)90055-A

Gibbs. (1987). A. K. Proterozoic volcanic rocks of the northern Guiana Shield, South America. *In: PHARAOH, T. C.; BECKINSALE, R. D.; RICKARD, D. (Cords) Geochemistry and Mineralization of Proterozoic Volcanic Suites. London: Geological Society of London, (Special Publication*(no 33), 275–288.

GIBBS, A. K. ; B. C. N. (1983). The Guiana Shield revisited. *Episodes*, *2*, 7–14.

Gibbs AK, B. C. (1993). *Geology of the Guiana shield* (246pp ed.). Oxford University Press,.

Goto, K. T., Sekine, Y., Ito, T., Suzuki, K., Anbar, A. D., Gordon, G. W., Harigane, Y., Maruoka, T., Shimoda, G., Kashiwabara, T., Takaya, Y., Nozaki, T., Hein, J. R., Tetteh, G. M., Nyame, F. K., & Kiyokawa, S. (2021). Progressive ocean oxygenation at ~2.2 Ga

inferred from geochemistry and molybdenum isotopes of the Nsuta Mn deposit, Ghana. *Chemical Geology*, *567*. https://doi.org/10.1016/j.chemgeo.2021.120116

Goulet, F. (2012). *Summary Report of the Structural Geology of the Matthews Ridge Deposit, NW District of Guyana and memoranda on structural geology of Matthews Ridge*.

Grill, E. V. (1982). Kinetic and thermodynamic factors controlling manganese concentrations in oceanic waters. *Geochimica et Cosmochimica Acta*, *46*(12), 2435–2446. https://doi.org/10.1016/0016-7037(82)90366-0

Guyana. (2013). *Matthews Ridge Manganese Project*. www.reuniongold.com

Hem, J. D. (1972). *Chemical Factors That Influence the Availability of Iron and Manganese in Aqueous Systems* (pp. 17–24). https://doi.org/10.1130/SPE140-p17

Hem, J. D. (1978). Redox processes at surfaces of manganese oxide and their effects on aqueous metal ions. *Chemical Geology*, *21*(3–4), 199–218. https://doi.org/10.1016/0009-2541(78)90045-1

Hem, J. D., & Lind, C. J. (1983). Nonequilibrium models for predicting forms of precipitated manganese oxides. *Geochimica et Cosmochimica Acta*, *47*(11), 2037–2046. https://doi.org/10.1016/0016-7037(83)90219-3

Jarvis, K. E., Gray, A. L., & McCurdy, E. (1989). Avoidance of spectral interference on europium in inductively coupled plasma mass spectrometry by sensitive measurement of the doubly charged ion. *Journal of Analytical Atomic Spectrometry*, *4*(8), 743. https://doi.org/10.1039/ja9890400743

Kamber, B. S., & Webb, G. E. (2001). The geochemistry of late Archaean microbial carbonate: implications for ocean chemistry and continental erosion history. *Geochimica et Cosmochimica Acta*, *65*(15), 2509–2525. https://doi.org/10.1016/S0016-7037(01)00613-5

Kesse, G. O. (1976). *The manganese ore deposits of Ghana.*

Krauskopf, K. B. (1957). Separation of manganese from iron in sedimentary processes. *Geochimica et Cosmochimica Acta*, *12*(1–2), 61–84. https://doi.org/10.1016/0016-7037(57)90018-2

Kroonenberg, S. B., De Roever, E. W. F., Fraga, L. M., Reis, N. J., Faraco, T., Lafon, J. M., Cordani, U., & Wong, T. E. (2016). Paleoproterozoic evolution of the Guiana Shield in Suriname: A revised model. *Geologie En Mijnbouw/Netherlands Journal of Geosciences*, *95*(4), 491–522. https://doi.org/10.1017/njg.2016.10

Kroonenberg, S. B., Mason, P. R. D., Kriegsman, L., & De Roever, E. (2019). *Geology and mineral deposits of the Guiana Shield*. https://www.researchgate.net/publication/331357379

Kurzweil, F., Wille, M., Gantert, N., Beukes, N. J., & Schoenberg, R. (2016). Manganese oxide shuttling in pre-GOE oceans – evidence from molybdenum and iron isotopes. *Earth and Planetary Science Letters*, *452*, 69–78. https://doi.org/10.1016/j.epsl.2016.07.013

Landing, W. M., & Bruland, K. W. (1980). Manganese in the North Pacific. *Earth and Planetary Science Letters*, *49*(1), 45–56. https://doi.org/10.1016/0012-821X(80)90149-1

Lawrence, M. G., Greig, A., Collerson, K. D., & Kamber, B. S. (2006). Rare Earth Element and Yttrium Variability in South East Queensland Waterways. *Aquatic Geochemistry*, *12*(1), 39–72. https://doi.org/10.1007/s10498-005-4471-8

Ledru, P., V6ra, J., Mil6si, J. P., & Tegyey, M. (1994). Pretumbriun Resenrth Markers of the last stages of the Palaeoproterozoic collision: evidence for a 2 Ga continent involving circum-South Atlantic provinces. In *Precambrian Research* (Vol. 69).

Leube, A., Hirdes, W., Mauer, R., & Kesse, G. O. (1990). The early Proterozoic Birimian Supergroup of Ghana and some aspects of its associated gold mineralization. *Precambrian Research*, *46*, 139–165.

Lind, C. J. , H. J. D. , R. C. E. (1987). *Reaction products of manganese bearing waters. In: Averett, R.C., McKnight, D.M. (Eds.), Chemical Quality of Water and Hydrologic Cycle.*

Loges, A., Wagner, T., Barth, M., Bau, M., Göb, S., & Markl, G. (2012). Negative Ce anomalies in Mn oxides: The role of Ce4+ mobility during water–mineral interaction. *Geochimica et Cosmochimica Acta*, *86*, 296–317. https://doi.org/10.1016/j.gca.2012.03.017

Matthew W. Totten, Mark A. Hanan, & Barry L. Weaver. (2000). Beyond whole-rock geochemistry of shales: The importance of assessing mineralogic controls for revealing tectonic discriminants of multiple sediment sources for the Ouachita Mountain flysch deposits. *GSA Bulletin*, *112*(7), 1012–1022.

Melezhik, V. A., & Fallick, A. E. (1994). A worldwide 2.2–2.0 Ga old positive δ13Ccarb anomaly as a phenomenon in relation to the Earth's major palaeoenvironmental changes. *Mineralogical Magazine*, *58A*, 593–594.

Melezhik, V. A., Fallick, A. E., Medvedev, P. V., & Makarikhin, V. V. (1999). Extreme 13Ccarb enrichment in ca. 2.0 Ga magnesite–stromatolite–dolomite–`red beds' association in a global context: a case for the world-wide signal enhanced by a local environment. *Earth-Science Reviews*, *48*(1–2), 71–120. https://doi.org/10.1016/S0012-8252(99)00044-6

Michael Gurnis. (1988). Large-scale mantle convection and the aggregation and dispersal of supercontinents . *Nature*, *332*, 695–699.

Murray, J. W., Balistrieri, L. S., & Paul, B. (1984). The oxidation state of manganese in marine sediments and ferromanganese nodules. *Geochimica et Cosmochimica Acta*, *48*(6), 1237–1247. https://doi.org/10.1016/0016-7037(84)90058-9

Murray, J. W., Dillard, J. G., Giovanoli, R., Moers, H., & Stumm, W. (1985). Oxidation of Mn(II): Initial mineralogy, oxidation state and ageing. *Geochimica et Cosmochimica Acta*, *49*(2), 463–470. https://doi.org/10.1016/0016-7037(85)90038-9

Nesbitt, H. , & Y. G. M. (1982). Nes Early Proterozoic climates and plate motions inferred from major element chemistry of lutites. *Nature*, *299*(5885), 715–717.

Nesbitt, H. W., Young, G. M., McLennan, S. M., & Keays, R. R. (1996). Effects of Chemical Weathering and Sorting on the Petrogenesis of Siliciclastic Sediments, with Implications for Provenance Studies. *The Journal of Geology*, *104*(5), 525–542. https://doi.org/10.1086/629850

Nicholson, K. (1992). Contrasting mineralogical-geochemical signatures of manganese oxides; guides to metallogenesis. *Economic Geology*, *87*(5), 1253–1264. https://doi.org/10.2113/gsecongeo.87.5.1253

Nyame, F. K. (1998). *Mineralogy, Geochemistry and Genesis of the Nsuta Manganese Deposit, Ghana. Unpublished Ph.D. thesis*. Okayama University, Japan .

Nyame, F. K. (2008). Petrography and geochemistry of intraclastic manganese-carbonates from the ~2.2 Ga Nsuta deposit of Ghana: Significance for manganese sedimentation in the Palaeoproterozoic of West Africa. *Journal of African Earth Sciences*, *50*(2–4), 133–147. https://doi.org/10.1016/j.jafrearsci.2007.09.007

Nyame, F. K. , 2001. (2001). Petrological significance of manganese–carbonate inclusions in spessartine garnet and relation to the stability of spessartine in metamorphosed manganese-rich rocks. *Contributions to Mineralogy and Petrology.*, *141*(6), 733–746.

Okita, P. M. , Maynard, Spiker, E. C., & Force, E. R. (1988). Isotopic evidence for organic matter oxidation by manganese reduction in the formation of stratiform manganese carbonate ore. *Geochimica et Cosmochimica Acta*, *52*, 2679–2685.

Okita, P. M., & Shanks III, W. C. ,. (1992). Origin of stratiform sedimenthosted manganese carbonate ore deposits: examples from Molango, Mexico and Taojiang, China. *Chemical Geology*, *99*, 139–164.

Ostrander, C. M., Nielsen, S. G., Owens, J. D., Kendall, B., Gordon, G. W., Romaniello, S. J., & Anbar, A. D. (2019). Fully oxygenated water columns over continental shelves before the Great Oxidation Event. *Nature Geoscience*, *12*(3), 186–191. https://doi.org/10.1038/s41561-019-0309-7

Piper, D. Z., Basler, J. R., & Bischoff, J. L. (1984). Oxidation state of marine manganese nodules. *Geochimica et Cosmochimica Acta*, *48*(11), 2347–2355. https://doi.org/10.1016/0016-7037(84)90230-8

Polgári, M., Okita, P. M., & Hein, J. R. ,. (1991). Stable isotope evidence for the origin of the Úrkút manganese ore deposit, Hungary. *Journal of Sedimentary Petrology* , *61*, 384–393.

Pourmand, A., Dauphas, N., & Ireland, T. J. (2012). A novel extraction chromatography and MC-ICP-MS technique for rapid analysis of REE, Sc and Y: Revising CI-chondrite and

Post-Archean Australian Shale (PAAS) abundances. *Chemical Geology*, *291*, 38–54. https://doi.org/10.1016/j.chemgeo.2011.08.011

Roy, S. (1988). MANGANESE METALLOGENESIS: A REVIEW. In *Ore Geology Reviews* (Vol. 4).

Roy, S. (1992). Environments and Processes of Manganese Deposition. In *Economic Geology* (Vol. 87).

Roy, S. (2006). Sedimentary manganese metallogenesis in response to the evolution of the Earth system. *Earth-Science Reviews*, *77*(4), 273–305. https://doi.org/10.1016/j.earscirev.2006.03.004

Scarpelli, W. ,. (1970). The Serra do Navio manganese deposit (Brazil). UNESCO. Genesis of Precambrian iron and manganese deposits. *Kiev Symp*, 217–228.

Smirnova, E. V., Mysovskaya, I. N., Lozhkin, V. I., Sandimirova, G. P., Pakhomova, N. N., & Smagunova, A. A. (2006). Spectral interferences from polyatomic barium ions in inductively coupled plasma mass spectrometry. *Journal of Applied Spectroscopy*, *73*(6), 911–917. https://doi.org/10.1007/s10812-006-0175-0

Stumm W & Giovanoli R. (1976). On the nature of particulate manganese in simulated lake waters. *Geochimica et Cosmochimica Acta*, *30*(9), 423–425. https://doi.org/10.1016/0016-7037(84)90390-9

Takahashi, Y., Sakami, H., & Nomura, M. (2002). Determination of the oxidation state of cerium in rocks by Ce LIII-edge X-ray absorption near-edge structure spectroscopy. *Analytica Chimica Acta*, *468*(2), 345–354. https://doi.org/10.1016/S0003-2670(02)00709-2

Taylor S.R., & McLennan S.M. (1985). *The continental crust: its composition and evolution*. Scientific Publications.

Tostevin, R., Shields, G. A., Tarbuck, G. M., He, T., Clarkson, M. O., & Wood, R. A. (2016a). Effective use of cerium anomalies as a redox proxy in carbonate-dominated marine settings. *Chemical Geology*, *438*, 146–162. https://doi.org/10.1016/j.chemgeo.2016.06.027

Tostevin, R., Shields, G. A., Tarbuck, G. M., He, T., Clarkson, M. O., & Wood, R. A. (2016b). Effective use of cerium anomalies as a redox proxy in carbonate-dominated marine settings. *Chemical Geology*, *438*, 146–162. https://doi.org/10.1016/j.chemgeo.2016.06.027

Tostevin, R., Wood, R. A., Shields, G. A., Poulton, S. W., Guilbaud, R., Bowyer, F., Penny, A. M., He, T., Curtis, A., Hoffmann, K. H., & Clarkson, M. O. (2016). Low-oxygen waters limited habitable space for early animals. *Nature Communications*, *7*(1), 12818. https://doi.org/10.1038/ncomms12818

Tsikos, H., & Moone, J. M. (1997). Petrography and Geochemistry of the Paleoproterozoic Hotazel Iron-Formation, Kalahari Manganese Field, South Africa: Implications for Precambrian Manganese Metallogenesis. In *Economic Geology* (Vol. 92).

Vanderhaeghe, O., Ledru, P., Thiéblemont, D., Egal, E., Cocherie, A., Tegyey, M., & Milési, J.-P. (1998). Contrasting mechanism of crustal growth. *Precambrian Research*, *92*(2), 165–193. https://doi.org/10.1016/S0301-9268(98)00074-6

Voicu, G., Bardoux, M., & Stevenson, R. (2001). Lithostratigraphy, geochronology and gold metallogeny in the northern Guiana Shield, South America: a review. In *Ore Geology Reviews* (Vol. 18). www.elsevier.comrlocateroregeorev

W. Stumm und J. J. Morgan. (1973). quatic Chemistry An Introduction Emphasizing Chemical Equilibria in Natural Waters. *Acta Hydrochimica et Hydrobiologica*, *1*(1), 117–117. https://doi.org/10.1002/aheh.19730010116

Warke, M. R., Strauss, H., & Schröder, S. (2020). Positive cerium anomalies imply pre-GOE redox stratification and manganese oxidation in Paleoproterozoic shallow marine environments. *Precambrian Research*, *344*. https://doi.org/10.1016/j.precamres.2020.105767

Worsley, T. R., Nance, D., & Moody, J. B. (1984). Global tectonics and eustasy for the past 2 billion years. *Marine Geology*, *58*(3–4), 373–400. https://doi.org/10.1016/0025-3227(84)90209-3

Major and trace elements	Core sample and depth										
	11MR1001									11MR1094	
	74.7m	76.6m	79.8m	81.3m	83m	83.4m	84.2m	86.5m	87.6m	64.4m	73.5m
%	%									%	
Al2O3	9.34	3.86	18.60	20.16	15.64	16.50	12.97	12.56	10.95	15.80	16.91
CaO	0.08	0.11	0.05	0.05	0.05	0.04	0.05	0.04	0.05	0.04	0.04
Fe2O3	6.20	4.13	5.82	9.53	5.84	7.51	7.07	5.16	8.78	8.75	8.28
K2O	0.73	-0.21	3.60	3.85	3.45	3.24	2.60	2.24	0.03	2.16	2.13
MgO	0.94	0.08	0.36	0.23	0.22	0.22	0.19	0.13	0.05	0.12	0.12
MnO	0.02	24.94	0.04	0.01	0.09	0.00	0.00	0.01	16.63	0.46	0.32
Na2O	0.13	0.23	0.47	0.39	0.45	0.33	0.23	0.24	0.00	0.24	0.31
P2O5	0.13	0.17	0.14	0.17	0.07	0.12	0.14	0.15	0.13	0.08	0.10
SiO2	77.07	56.72	64.83	57.95	68.88	66.36	71.55	74.42	57.57	65.17	64.05
TiO2	0.34	0.16	0.46	1.00	0.54	0.55	0.52	0.54	0.33	0.52	0.60
LOI	3.58	5.30	4.20	4.91	3.06	3.76	3.15	3.20	3.15	4.82	5.39
Total	94.98	90.19	94.38	93.33	95.22	94.86	95.32	95.48	94.52	93.33	92.86
ppm	ppm									ppm	
Mn/Fe	0.00	6.69	0.01	0.00	0.02	0.00	0.00	0.00	2.10	0.06	0.04
Sc	13	7	20	23	17	23	20	21	30	26	27
Ti	3048	1385	4032	7561	3953	4674	4725	4828	2827	4503	5149
V	38	48	52	94	65	73	56	73	206	114	122
Cr	42	29	90	62	49	91	88	64	127	128	266
Mn	215	155295	389	166	535	67	109	111	113059	3156	2307
Co	23	216	17	29	29	14	21	17	81	45	36
Ni	60	69	68	51	51	41	48	40	361	65	47
Cu	65	67	162	33	18	21	17	40	432	20	20
Zn	200	606	132	143	65	65	59	73	412	39	44
Ga	18	13	59	51	44	55	41	40	18	46	69
As	6	10	2	3	2	2	4	2	36	1	2
Rb	13	21	67	78	70	67	57	46	4	97	94
Sr	41	1573	101	77	93	78	57	54	116	52	68

Y	24	21	26	26	20	25	38	18	124	13	14
Zr	137	85	297	245	228	239	202	164	190	154	172
Nb	6	2	13	11	8	8	7	7	9	7	8
Mo	2	17	2	2	2	1	4	2	12	2	2
Cs	1	2	5	7	6	6	5	3	2	3	3
Ba	222	204	1006	960	796	770	694	678	69	780	1390
La	27	29	10	4	36	12	52	19	85	6	15
Ce	37	36	18	11	59	21	24	20	215	51	48
Pr	5.29	6.61	2.68	1.05	7.43	2.68	12.90	4.21	25.75	1.48	2.90
Nd	23.63	30.13	10.19	3.94	28.32	10.91	52.60	16.60	106.08	6.07	9.85
Sm	4.42	6.32	2.56	1.51	5.27	2.42	10.27	3.30	28.07	1.62	2.22
Eu	1.06	1.34	0.96	0.56	1.49	0.69	2.15	0.89	6.34	0.42	0.57
Gd	5.00	5.97	3.51	2.22	4.99	3.03	7.97	3.28	22.56	1.67	2.08
Tb	0.59	0.66	0.53	0.51	0.55	0.54	1.11	0.51	3.58	0.29	0.35
Dy	3.84	4.23	4.46	4.10	3.05	3.98	6.79	3.02	23.46	2.21	2.44
Ho	0.78	0.79	0.92	0.78	0.64	0.88	1.34	0.71	4.45	0.47	0.54
Er	2.23	1.88	2.71	2.37	1.64	2.49	3.98	2.21	12.36	1.57	1.77
Yb	2.29	1.64	2.78	2.37	1.83	2.98	3.77	2.12	12.83	1.89	1.95
Lu	0.40	0.27	0.45	0.45	0.33	0.48	0.62	0.33	1.78	0.33	0.29
Hf	3.25	1.76	7.94	6.79	6.21	6.12	4.66	3.70	4.81	3.51	4.01
Ta	0.78	0.47	1.85	1.38	1.08	1.18	0.91	0.87	0.81	0.85	1.09
Pb	3.03	27.65	3.44	4.20	5.11	5.17	4.26	2.78	21.34	10.36	9.36
Th	2.88	1.07	7.80	4.54	4.86	4.68	2.66	2.46	4.57	5.12	5.53
U	0.71	0.44	0.41	0.73	0.33	0.38	0.55	0.63	5.39	1.17	1.34

Major and trace elements	Core sample and depth										
	11MR2014			11MR1091							
	69.9m	73m	75.4m	85m	89.7m	94m	97.5m	99.4m	101.4m	105.5m	106.6m
%	%			%							
Al2O3	15.20	23.97	21.05	16.51	19.28	17.98	15.91	19.89	20.90	20.20	19.28
CaO	0.04	0.03	0.03	0.05	0.06	0.06	0.07	0.11	0.11	0.09	0.10
Fe2O3	8.43	6.13	7.35	8.57	3.28	8.39	7.52	10.20	7.24	10.85	9.66
K2O	1.57	4.49	3.04	1.36	3.71	2.41	1.93	1.80	1.69	2.33	2.08
MgO	2.95	1.04	2.97	0.10	0.18	0.17	0.15	0.08	0.08	0.11	0.12
MnO	1.34	3.11	1.44	0.76	0.19	0.38	0.41	0.02	0.24	0.21	0.16
Na2O	0.03	0.19	0.08	0.45	0.71	0.89	0.93	1.77	1.69	1.54	1.38
P2O5	0.03	0.09	0.02	0.07	0.04	0.01	0.02	0.06	0.08	0.06	0.06
SiO2	63.03	48.17	53.97	64.14	55.19	63.37	67.49	59.72	60.75	57.96	60.63
TiO2	0.49	0.82	0.83	0.55	0.30	0.61	0.59	0.83	0.86	0.85	0.85
LOI	4.90	6.68	6.21	5.60	2.25	3.99	3.49	3.84	4.54	3.94	4.08
Total	93.10	88.03	90.78	92.56	82.94	94.29	95.02	94.46	93.62	94.20	94.32
ppm	ppm			ppm							
Mn/Fe	0.18	0.56	0.22	0.10	0.06	0.05	0.06	0.00	0.04	0.02	0.02
Sc	22	21	25	27	16	26	24	33	29	32	31
Ti	4339	5149	6727	4641	2947	5287	5146	7183	6844	6716	6644
V	75	435	154	118	86	81	62	148	118	122	132
Cr	85	73	83	145	70	127	103	155	125	131	217
Mn	9449	17495	10539	5087	1611	2803	2775	235	1719	1513	1158
Co	26	142	29	56		55	33	15	35	48	51
Ni	65	218	98	57	48	118	65	53	52	104	62
Cu	143	63	55	30	10	25	10	16	58	12	17
Zn	133	271	101	37	38	36	36	29	36	48	48
Ga	67	158	159	49	73	51	36	39	41	48	47
As	1	8	1	1	2	1	2	1	1	1	2
Rb	53	145	91	54	147	109	89	72	64	82	73

Sr	36	57	49	99	101	120	127	198	194	156	137
Y	20	16	23	11	8	10	12	13	14	13	13
Zr	146	214	292	172	157	177	157	223	202	207	190
Nb	7	9	12	6	7	8	7	9	9	8	8
Mo	5	2	2	3	3	3	3	2	2	3	4
Cs	5	11	8	2	5	4	4	3	3	3	3
Ba	1426	3731	2725	763	1391	870	570	540	476	575	521
La	15	28	21	10	4	8	35	21	40	14	16
Ce	31	58	46	36	17	40	37	10	39	23	19
Pr	3.66	7.50	5.45	2.06	1.41	1.88	6.61	3.85	7.45	3.0	3.39
Nd	15.84	26.77	21.05	8.41	6.51	7.07	21.30	13.76	24.97	10.9	12.29
Sm	3.19	4.69	4.37	2.05	1.23	1.51	3.50	2.21	4.17	1.8	2.16
Eu	1.05	1.07	1.19	0.45	0.39	0.42	0.82	0.56	1.06	0.54	0.51
Gd	3.03	3.38	3.69	1.90	1.16	1.48	2.40	2.02	3.27	1.6	1.84
Tb	0.49	0.48	0.60	0.31	0.18	0.17	0.33	0.31	0.47	0.3	0.27
Dy	3.24	2.76	4.24	2.06	1.26	1.55	2.16	2.06	2.91	1.9	2.10
Ho	0.69	0.52	0.91	0.43	0.30	0.33	0.44	0.44	0.53	0.5	0.45
Er	1.98	1.49	2.36	1.41	1.02	1.29	1.27	1.65	1.50	1.7	1.60
Yb	1.73	1.38	2.11	1.72	1.09	1.72	1.33	2.00	1.84	1.9	1.93
Lu	0.24	0.28	0.34	0.24	0.16	0.31	0.23	0.37	0.30	0.3	0.29
Hf	3.47	5.99	7.29	3.98	4.46	4.09	3.83	5.14	4.62	4.9	4.25
Ta	1.03	1.27	1.51	0.80	3.12	0.96	1.37	1.02	0.95	0.9	0.89
Pb	34.92	8.07	12.88	11.43	8.20	10.93	8.00	5.40	4.89	5.1	4.21
Th	4.58	7.94	7.00	5.09	7.56	5.14	3.75	2.65	2.51	2.6	2.25
U	0.77	1.11	0.89	1.14	0.77	1.29	0.86	0.82	1.10	0.7	0.71

REE anomalies	Core sample and depth										
	11MR1001									11MR1094	
	74.7m	76.6m	79.8m	81.3m	83m	83.4m	84.2m	86.5m	87.6m	64.4m	73.5m
Eu/Eu*	1.34	1.28	1.77	1.36	1.71	1.30	1.25	1.44	1.29	1.29	1.35
Ce/Ce*(Bau&Dulski, 1996)	0.73	0.63	0.82	1.30	0.87	0.87	0.22	0.53	1.10	4.2	1.73
Ce/Ce*	0.97	0.78	0.80	1.21	0.94	0.98	0.24	0.57	1.08	4.42	1.75
Pr/Pr*	0.99	1.07	1.11	0.91	1.03	1.00	1.51	1.24	0.96	0.39	0.71

REE anomalies	Core sample and depth										
	11MR2014			11MR1091							
	69.9m	73m	75.4m	85m	89.7m	94m	97.5m	99.4m	101.4m	105.5m	106.6m
Eu/Eu*	1.75	1.38	1.51	1.19	1.74	1.62	1.45	1.40	1.50	1.61	1.35
Ce/Ce*(Bau&Dulski, 1996)	1.02	0.96	1.03	1.90	1.61	2.50	0.58	0.27	0.54	0.86	0.63
Ce/Ce*	1.16	0.86	1.02	2.21	1.73	2.53	0.56	0.30	0.55	0.89	0.65
Pr/Pr*	0.92	1.08	0.99	0.65	0.76	0.57	1.32	1.56	1.32	1.06	1.22

Chemical alteration indexes	Core sample and depth										
	11MR1001									11MR1094	
	74.7m	76.6m	79.8m	81.3m	83m	83.4m	84.2m	86.5m	87.6m	64.4m	73.5m
CIA%	89.13	86.94	79.63	80.46	77.43	80.02	79.81	81.31	99.06	84.95	85.42
MIA%	79.03	89.38	79.71	82.74	79.08	81.98	82.26	83.18	98.65	87.30	87.41
IOL%	16.78	12.35	27.36	33.88	23.77	26.56	21.88	19.24	25.53	27.36	28.22

Chemical alteration indexes	Core sample and depth										
	11MR2014			11MR1091							
	69.9m	73m	75.4m	85m	89.7m	94m	97.5m	99.4m	101.4m	105.5m	106.6m
CIA%	89.33	82.12	85.81	78.80	79.89	82.22	81.29	84.70	81.32	79.49	80.40
MIA%	68.93	78.06	70.06	82.01	82.87	82.25	83.84	86.10	83.64	83.19	83.60

IOL%	27.26	38.45	34.48	28.10	30.27	27.82	27.72	28.88	31.65	34.88	32.31

Nsuta Mine	Samples		
Chemical alteration	M9	M10	NS5
CIA%	43.96	77.54	34.46
MIA%	14.51	15.71	28.27

Serra Do Navio	Graphite-Schist				Biotite-Schist				
Chemical alteration	DH114-J	DH116-K	DH116-P	D114-O	D114-P	D116-N	D116-Q	D116-T	DH140-K
CIA%	48.50	50.55	53.73	52.69	54.58	52.28	47.82	91.92	58.46
MIA%	43.07	30.89	41.45	37.12	29.22	39.04	19.57	46.54	39.60

APPENDIX 2 (ICP-MS data)

Sample (ppm)						
Element	**11MR1001(76.6M)MIN-5**	**11MR1001(76.6M)MIN-6**	**11MR1001(76.6M)MIN-7**	**11MR1001(76.6M)MIN-8**	**11MR1001(76.6M)MIN-9**	**11MR1001(76.6M)MIN-10**
Sc45	12.58	3.82	10.30	5.41	34.54	4.84
Ti49	68.86	18.80	5411.39	336.36	111.94	440.29
V51	815.43	211.27	136.70	69.79	1940.28	58.63
Cr52	15.01	3.24	29.62	4.39	10.39	5.52
Mn55	4301124.00	1512915.88	582713.44	453346.81	6495900.50	400380.63
Co59	3931.75	1140.77	754.55	391.71	15926.62	513.97
Ni60	455.99	168.37	48.93	23.80	831.24	37.34
Cu63	598.18	110.66	349.34	54.98	1272.72	94.14
Zn66	31175.95	10206.24	2953.20	2275.46	62968.91	2665.88
Rb85	438.91	149.62	67.19	62.21	688.51	51.74
Sr88	46373.14	13412.83	5114.20	3717.53	75926.83	3346.72
Zr90	7.92	0.35	122.85	23.82	15.82	41.60
Nb93	0.14	<0.0088	11.99	0.45	0.19	0.76
Cs133	42.08	13.33	7.23	6.00	106.81	5.22
Ba137	3556.74	81.85	242.17	304.67	1300.76	212.12
Pb208	2844.77	4.61	43.94	21.17	3717.99	0.74
La139	206.24	15.19	49.59	16.72	857.84	27.00
Ce140	782.48	11.53	75.66	26.62	1845.47	62.95
Pr141	41.00	2.81	12.92	4.04	202.52	7.15
Nd146	169.91	13.84	55.24	18.36	830.73	30.30
Sm147	32.91	2.80	11.64	3.71	160.29	6.58
Eu151	8.37	0.75	2.93	0.87	38.41	1.63
Eu153	8.66	0.81	2.86	0.99	38.69	1.52
Eu	8.52	0.78	2.90	0.93	38.55	1.58
Gd157	37.55	4.70	11.90	4.25	149.01	6.58
Tb159	4.88	0.64	1.62	0.55	17.72	0.77
Dy163	27.91	3.68	9.21	3.05	96.33	4.32
Y89	173.10	35.10	42.72	17.43	429.61	23.21
Ho165	5.17	0.81	1.79	0.58	15.23	0.81
Er166	12.96	2.07	4.62	1.43	37.14	2.13
Tm169	1.84	0.22	0.61	0.17	4.34	0.25
Yb172	11.46	1.20	4.18	1.06	23.55	1.62
Lu175	1.67	0.22	0.71	0.16	3.96	0.25
Hf178	0.17	0.03	2.72	0.54	0.19	0.92
Ta181	<0.0193	<0.0080	0.80	0.05	<0.030	0.07
Th232	0.29	0.02	1.60	0.30	0.58	0.32
U238	2.36	0.42	1.64	0.24	5.32	0.28

	Sample (ppm)					
Element	**11MR1001(81.3M)MnMIN-13**	**11MR1001(81.3M)-14**	**11MR1001(81.3M)-15**	**11MR1001(81.3M)-16**	**11MR1001(81.3M)-17**	**11MR1001(81.3M)-18**
Sc45	2.66	9.06	19.29	7.34	20.69	4.69
Ti49	154.57	1669.43	3522.61	1244.20	9527.68	594.47
V51	1.92	36.89	121.37	42.16	100.84	14.16
Cr52	2.54	11.38	15.31	43.17	51.76	8.81
Mn55	134.99	41.00	11.74	25.81	8.84	55.68
Co59	3.20	0.49	2.65	0.67	0.67	0.33
Ni60	4.11	6.11	21.69	24.50	16.61	2.81
Cu63	3.80	11.25	38.55	46.26	36.57	5.13
Zn66	8.28	37.09	146.45	233.27	153.27	23.06
Rb85	8.15	44.16	138.85	27.16	91.08	20.51
Sr88	23.80	36.44	92.48	36.24	79.82	28.82
Zr90	67.88	98.96	166.87	78.42	802.71	76.32
Nb93	0.48	2.90	6.53	1.72	20.62	1.33
Cs133	0.24	3.83	12.90	2.32	7.61	1.54
Ba137	75.61	468.12	1260.81	257.57	871.17	195.32
Pb208	3.79	3.18	7.81	4.46	9.04	3.60
La	32.31	2.71	1.26	3.28	1.94	2.89
Ce140	37.40	4.06	3.23	4.45	5.66	4.31
Pr141	4.43	0.57	0.44	0.78	0.66	0.59
Nd146	21.39	2.40	1.87	3.44	3.73	2.40
Sm147	4.52	0.57	0.85	0.88	2.34	0.51
Eu151	0.91	0.26	0.43	0.24	1.12	0.14
Eu153	1.00	0.25	0.41	0.28	1.08	0.15
Eu	0.95	0.25	0.42	0.26	1.10	0.15
Gd157	5.17	0.81	1.33	1.07	4.52	0.85
Tb159	0.35	0.16	0.28	0.20	0.93	0.17
Dy163	1.66	1.19	2.23	1.35	7.36	1.32
Y89	7.41	7.27	13.35	7.37	53.31	10.58
Ho165	0.24	0.25	0.48	0.25	2.02	0.31
Er166	0.54	0.78	1.58	0.73	6.48	0.76
Tm169	0.09	0.13	0.25	0.10	1.01	0.09
Yb172	0.49	1.02	1.78	0.77	8.28	0.62
Lu175	0.07	0.17	0.28	0.13	1.27	0.09
Hf178	1.65	2.69	4.94	2.01	19.18	1.98
Ta181	0.05	0.40	1.35	0.17	1.92	0.12
Th232	0.95	2.06	3.82	1.45	13.65	1.16
U238	0.28	0.32	0.76	0.52	2.01	0.29

	Sample (ppm)					
Element	**11MR1001(84.2M)-21**	**11MR1001(84.2M)-22**	**11MR1001(84.2M)-23**	**11MR1001(84.2M)-24**	**11MR1001(84.2M)-25**	**11MR1001(84.2M)-26**
Sc45	15.37	27.66	15.55	12.94	21.62	11.07
Ti49	4392.49	18230.40	210.19	937.31	14875.08	3646.87
V51	53.81	111.16	45.64	36.35	114.12	67.89
Cr52	72.80	164.92	0.00	35.78	171.89	69.41
Mn55	13.20	10.03	871.87	17.49	13.08	67.84
Co59	1.89	0.72	0.24	0.37	0.47	0.30
Ni60	24.19	12.08	0.00	10.96	39.43	6.45
Cu63	25.31	14.02	2.80	11.59	36.73	14.56
Zn66	140.37	73.63	9.21	62.61	220.92	48.57
Rb85	51.17	112.46	146.62	51.99	115.57	44.20
Sr88	40.81	87.79	67.15	52.84	104.34	26.02
Zr90	210.54	592.89	0.20	72.70	346.92	103.00
Nb93	6.67	29.38	0.08	2.10	25.24	5.15
Cs133	4.86	8.75	8.58	3.72	9.48	3.61
Ba137	399.92	1072.16	1098.28	476.04	877.47	410.66
Pb208	4.28	11.30	2.63	4.34	14.07	6.29
La139	6.55	37.34	0.04	32.57	44.56	7.71
Ce140	7.17	70.68	0.15	13.99	42.86	10.01
Pr141	1.24	7.81	0.02	2.74	11.19	2.13
Nd146	5.06	29.46	0.04	14.65	43.24	8.07
Sm147	1.27	7.00	0.07	2.32	8.15	1.66
Eu151	0.46	1.84	0.00	0.53	2.11	0.40
Eu153	0.46	1.68	0.00	0.53	2.13	0.42
Eu	0.46	1.76	0.00	0.53	2.12	0.41
Gd157	1.56	5.85	0.00	1.90	6.37	1.37
Tb159	0.28	0.99	0.01	0.25	0.98	0.24
Dy163	2.41	8.05	0.00	1.23	5.99	1.62
Y89	15.07	48.35	0.00	6.74	32.87	8.64
Ho165	0.56	1.81	0.01	0.27	1.12	0.33
Er166	1.88	5.50	0.00	0.65	3.42	1.21
Tm169	0.34	0.90	0.01	0.08	0.54	0.17
Yb172	2.26	6.71	0.00	0.79	4.39	1.30
Lu175	0.41	1.09	0.01	0.12	0.63	0.20
Hf178	5.16	14.75	0.08	1.63	7.53	2.11
Ta181	0.58	2.33	0.09	0.20	1.87	0.36
Th232	4.40	10.07	0.03	1.66	6.58	4.58
U238	0.47	1.05	0.01	0.33	0.97	0.33

	Sample (ppm)					
Element	**CHERT-29**	**CHERT-30**	**CHERT-31**	**CHERT-32**	**CHERT-33**	**CHERT-34**
Sc45	7.89	8.09	4.44	7.41	5.24	5.63
Ti49	41.26	120.18	160.92	89.22	99.79	138.29
V51	0.73	46.60	2.18	70.96	3.30	2.70
Cr52	133.46	13.46	188.64	54.84	50.71	76.94
Mn55	17.84	12.54	564.21	4862.06	573.22	75.87
Co59	3.35	7.65	2.89	853.25	4.29	8.43
Ni60	<9.53	<2.40	<17.71	30.51	14.57	22.94
Cu63	14.15	19.11	336.86	3840.54	252.20	453.60
Zn66	27.85	9.46	58.69	708.97	45.90	46.03
Rb85	2.86	46.67	0.95	4.58	6.87	5.80
Sr88	9.78	24.77	12.77	34.43	19.14	38.68
Zr90	21.12	3.69	35.11	40.53	56.37	61.01
Nb93	0.20	0.02	0.45	0.23	0.56	0.26
Cs133	0.17	2.98	0.36	0.24	0.35	0.24
Ba137	66.05	350.30	40.77	59.03	74.73	72.13
Pb208	2.31	0.87	5.93	2.46	3.58	3.85
La139	2287.25	63.00	3731.39	107.34	5622.62	1548.47
Ce140	1.70	0.17	10.61	14.12	4.07	3.36
Pr141	0.28	0.03	0.33	3.00	0.54	0.52
Nd146	17.67	0.25	0.49	15.45	2.21	1.56
Sm147	0.00	0.06	0.64	4.07	0.39	0.52
Eu151	0.00	0.00	0.00	1.22	0.13	0.42
Eu153	0.00	0.00	0.24	1.05	0.00	0.07
Eu	0.00	0.00	0.12	1.14	0.06	0.24
Gd157	0.00	0.00	1.09	4.53	0.82	0.22
Tb159	0.23	0.00	0.15	0.74	0.17	0.06
Dy163	0.31	0.05	0.00	5.86	0.36	0.69
Y89	1.47	0.21	1.55	33.28	2.09	2.95
Ho165	0.03	0.00	0.20	0.94	0.06	0.10
Er166	0.09	0.04	0.11	2.70	0.53	0.20
Tm169	0.00	0.00	0.32	0.41	0.13	0.05
Yb172	0.07	0.00	0.00	2.14	0.81	0.59
Lu175	0.03	0.00	0.03	0.30	0.01	0.08
Hf178	0.95	0.13	1.04	0.89	1.83	1.82
Ta181	0.00	0.02	0.00	0.03	0.04	0.06
Th232	0.54	0.08	1.18	0.38	1.01	1.19
U238	1.23	0.04	0.25	4.30	0.27	0.36

Appendix 3: MP analysis data			
analyses	Quartz	Mn ox	Mn ox
wt%	11MR1001(76.6m)-A	11MR1001(76.6m)-A	11MR1001(76.6m)-A-1um
SiO2	100.08	0.06	6.43
TiO2	0.02	-0.01	0.01
Al2O3	1.61	0.25	5.59
Cr2O3			
Fe2O3			
FeO	0.03	0.15	0.49
Mn2O3			
MnO	0.17	72.83	63.45
MgO	0.01	0.04	0.16
CaO	0.01	0.32	0.28
Na2O	0.06	0.65	0.71
K2O	0.38	2.27	3.21
SO3	0.01	0.03	0.01
CoO	0.42	0.36	0.34
P2O5	0.01	0.46	0.32
Cu2O	-0.01	-0.02	0.01
CO2			
H2O			
total wt%	102.81	77.39	81.01
oxy	2.00	16.00	16.00
adapting Fe3+, Mn3+ and H2O	11MR1001(76.6m)-A	11MR1001(76.6m)-A	11MR1001(76.6m)-A-1um
wt%		0.06	
SiO2			
TiO2		0.25	
Al2O3			
Cr2O3		0.17	
Fe2O3		0.00	
FeO		80.97	
Mn2O3		0.06	
MnO		0.04	
MgO		0.32	
CaO		0.65	
Na2O		2.27	
K2O			
H2O			
CO2			
CoO		84.80	0.00
total wt%			
oxy			
mineral formulae (oxides)	11MR1001(76.6m)-A	11MR1001(76.6m)-A	11MR1001(76.6m)-A-1um
Si		0.01	
Ti			
Al		0.05	
Cr			
Fe3+		0.02	
Fe2+			
Mn3+		10.30	
Mn2+		0.01	
Mg		0.01	
Ca		0.06	
Na		0.21	
K		0.48	
OH			
C			
Co			
cation sum		11.15	
ideal cations	1.00	9.00	
name	Quartz	Cryptomelane	Unidentified Mn-oxide

analyses	Mica	Mn ox	Fe ox
wt%	11MR1001(76.6m)-A-1um	11MR1001(76.6m)-A-1um	11MR1001(76.6m)-B
SiO2	45.22	0.09	2.12
TiO2	0.02	0.01	-0.01
Al2O3	36.95	0.62	0.12
Cr2O3			
Fe2O3			
FeO	0.15	1.86	72.54
Mn2O3			
MnO	5.97	71.70	0.51
MgO	0.15	0.04	0.10
CaO	0.10	0.29	0.01
Na2O	4.74	0.62	0.01
K2O	2.92	2.21	-0.03
SO3	-0.01	-0.01	0.14
CoO	0.28	0.26	0.23
P2O5	0.03	0.56	0.29
Cu2O	-0.01	0.03	0.04
CO2			
H2O			
total wt%	96.51	78.29	76.08
oxy	11.00	16.00	
adapting Fe3+, Mn3+ and H2O	11MR1001(76.6m)-A-1um	11MR1001(76.6m)-A-1um	11MR1001(76.6m)-B
wt%	45.22		2.12
SiO2	0.02		0.01
TiO2	36.95		5.59
Al2O3			0.00
Cr2O3	0.05		72.50
Fe2O3	0.11		7.30
FeO	1.82		0.00
Mn2O3	4.34		0.51
MnO	0.15		0.10
MgO	0.10		0.01
CaO	4.74		0.01
Na2O	2.92		0.00
K2O	4.59		0.00
H2O			
CO2	0.28		0.23
CoO	101.27	0.00	88.38
total wt%			
oxy			
mineral formulae (oxides)	11MR1001(76.6m)-A-1um	11MR1001(76.6m)-A-1um	11MR1001(76.6m)-B
Si	2.95	0.02	0.06
Ti		0.00	0.00
Al	2.84	0.13	0.19
Cr			0.00
Fe3+			1.59
Fe2+	0.01	0.29	0.18
Mn3+	0.09	10.03	0.00
Mn2+	0.24		0.01
Mg	0.01	0.01	0.00
Ca	0.01	0.06	0.00
Na	0.60	0.22	0.00
K	0.24	0.52	0.00
OH	2.00		
C			
Co	0.02		
cation sum	7.00	11.27	2.04
ideal cations	7.00	9.00	2.00
name	Mn-rich Muscovite	Cryptomelane	Hematite

analyses	Mn ox	Unidentified Mineral	lithiphorite
wt%	11MR1001(76.6m)-B	11MR1001(76.6m)-B	11MR1001(76.6m)-E
SiO2	0.08	55.83	0.27
TiO2	0.01	0.04	-0.01
Al2O3	0.77	3.39	21.32
Cr2O3			
Fe2O3			
FeO	0.26	0.07	3.67
Mn2O3			
MnO	72.91	32.50	40.76
MgO	0.08	0.03	0.10
CaO	0.27	0.07	0.05
Na2O	0.66	0.27	0.14
K2O	2.27	2.04	0.00
SO3	-0.01	0.01	0.01
CoO	0.65	0.37	1.51
P2O5	0.48	0.09	0.09
Cu2O	0.02	-0.01	0.27
CO2			
H2O			
total wt%	78.47	94.70	68.18
oxy			3.00
adapting Fe3+, Mn3+ and H2O	11MR1001(76.6m)-B	11MR1001(76.6m)-B	11MR1001(76.6m)-E
wt%	0.08		
SiO2	0.01		
TiO2	0.77		
Al2O3			
Cr2O3			
Fe2O3	0.26		
FeO	75.00		
Mn2O3	8.60		
MnO	0.08		
MgO	0.27		
CaO	0.66		
Na2O	2.27		
K2O	-0.01		
H2O			
CO2			
CoO	88.01		0.00
total wt%			
oxy			
mineral formulae (oxides)	11MR1001(76.6m)-B	11MR1001(76.6m)-B	11MR1001(76.6m)-E
Si	0.01	8.74	
Ti	0.00		
Al	0.15	0.63	
Cr	0.00		
Fe3+	0.00		
Fe2+	0.03	0.01	
Mn3+	9.13		
Mn2+	1.16	4.31	
Mg	0.02	0.01	
Ca	0.05	0.01	
Na	0.21	0.08	
K	0.46	0.41	
OH	-0.01	2.03	
C			
Co		0.06	
cation sum	11.22	14.19	0.00
ideal cations	9.00	15.00	3.00
name	Cryptomelane	Unidentified Mineral	lithiophorite

analyses	magnetite	Chlorite	Mica
wt%	11MR1001(76.6m)-F	11MR1001(76.6m)-F	11MR1001(81.3m)-2
SiO2	1.31	29.57	58.35
TiO2	0.04	0.25	2.96
Al2O3	9.16	25.81	18.42
Cr2O3			
Fe2O3			
FeO	55.22	11.87	8.08
Mn2O3			
MnO	0.20	0.23	0.01
MgO	0.04	0.27	0.19
CaO	0.08	0.08	0.01
Na2O	0.02	0.08	0.43
K2O	-0.02	0.01	3.43
SO3	0.01	0.03	0.00
CoO	0.34	0.10	0.20
P2O5	2.17	0.39	0.10
Cu2O	0.06	0.04	0.00
CO2	3.00		0.00
H2O			
total wt%	68.63	68.71	92.18
oxy	2.00		12.00
adapting Fe3+, Mn3+ and H2O	11MR1001(76.6m)-F	11MR1001(76.6m)-F	11MR1001(81.3m)-2
wt%			
SiO2			
TiO2			
Al2O3			
Cr2O3			
Fe2O3			
FeO			
Mn2O3			
MnO			
MgO			
CaO			
Na2O			
K2O			
H2O			
CO2			
CoO	0.00		
total wt%			
oxy			
mineral formulae (oxides)	11MR1001(76.6m)-F	11MR1001(76.6m)-F	11MR1001(81.3m)-2
Si	0.04		4.28
Ti	0.00		0.16
Al	0.36		1.59
Cr	0.00		0.00
Fe3+	1.25		0.00
Fe2+	0.29		0.50
Mn3+	0.00		0.00
Mn2+	0.01		0.00
Mg	0.00		0.02
Ca	0.00		0.00
Na	0.00		0.06
K	0.00		0.32
OH	0.00		3.97
C			
Co			
cation sum	1.96	0.00	6.95
ideal cations	2.00	3.00	7.00
name	Magnetite	Unidentified Chlorite	illite

analyses	Mica	Mica	Fe-Ti oxide
wt%	11MR1001(81.3m)-2	#	11MR1001(81.3m)-3
SiO2	45.44	47.96	1.03
TiO2	0.10	0.36	56.95
Al2O3	25.45	25.53	1.56
Cr2O3			
Fe2O3			
FeO	7.67	6.66	30.05
Mn2O3			
MnO	0.01	0.00	-0.03
MgO	0.28	0.28	0.02
CaO	0.03	0.02	0.03
Na2O	0.61	0.58	0.03
K2O	5.64	5.51	-0.01
SO3	0.02	0.00	0.02
CoO	0.22	0.30	0.29
P2O5	0.23	0.16	0.20
Cu2O	-0.01	0.00	0.02
CO2	0.00	0.00	0.00
H2O			
total wt%	85.70	87.34	90.16
oxy	11.00	11.00	3.00
adapting Fe3+, Mn3+ and H2O	11MR1001(81.3m)-2	11MR1001(81.3m)-2	11MR1001(81.3m)-3
wt%			
SiO2			
TiO2			
Al2O3			
Cr2O3			
Fe2O3			
FeO			
Mn2O3			
MnO			
MgO			
CaO			
Na2O			
K2O			
H2O			
CO2			
CoO			
total wt%			
oxy			
mineral formulae (oxides)	11MR1001(81.3m)-2	11MR1001(81.3m)-2	11MR1001(81.3m)-3
Si	3.37	3.45	0.03
Ti	0.01	0.02	1.10
Al	2.23	2.17	0.05
Cr	0.00	0.00	0.00
Fe3+	0.00	0.00	0.00
Fe2+	0.48	0.40	0.65
Mn3+	0.00	0.00	0.00
Mn2+	0.00	0.00	0.00
Mg	0.03	0.03	0.00
Ca	0.00	0.00	0.00
Na	0.09	0.08	0.00
K	0.53	0.51	0.00
OH	2.48	2.40	0.00
C			
Co			
cation sum	6.74	6.65	1.82
ideal cations	7.00	7.00	2.00
name	Al-illite-hydromica	Al-illite-hydromica	illmenite

analyses	Mica	Chlorite	Chlorite
wt%	11MR1001(81.3m)-3	11MR1001(81.3m)-3	11MR1001(81.3m)-3
SiO2	45.23	29.71	18.37
TiO2	0.10	0.05	0.03
Al2O3	30.67	26.76	18.49
Cr2O3			
Fe2O3			
FeO	4.65	18.23	21.55
Mn2O3			
MnO	-0.01	-0.01	0.01
MgO	0.39	0.18	0.14
CaO	0.07	0.05	0.08
Na2O	0.87	0.36	0.29
K2O	7.75	2.75	1.58
SO3	0.01	0.02	0.02
CoO	0.09	0.28	0.35
P2O5	0.07	0.57	0.71
Cu2O	0.00	0.02	0.02
CO2	0.00	0.00	0.00
H2O			
total wt%	89.90	78.97	61.63
oxy	11.00		
adapting Fe3+, Mn3+ and H2O	11MR1001(81.3m)-3	11MR1001(81.3m)-3	11MR1001(81.3m)-3
wt%			
SiO2			
TiO2			
Al2O3			
Cr2O3			
Fe2O3			
FeO			
Mn2O3			
MnO			
MgO			
CaO			
Na2O			
K2O			
H2O			
CO2			
CoO			
total wt%			
oxy			
mineral formulae (oxides)	11MR1001(81.3m)-3	11MR1001(81.3m)-3	11MR1001(81.3m)-3
Si	3.20		
Ti	0.01		
Al	2.56		
Cr	0.00		
Fe3+	0.00		
Fe2+	0.27		
Mn3+	0.00		
Mn2+	0.00		
Mg	0.04		
Ca	0.01		
Na	0.12		
K	0.70		
OH	2.36		
C			
Co			
cation sum	6.90		
ideal cations	7.00		
name	Muscovite	Unidentified Chlorite	Unidentified Chlorite

analyses	Mn-Ox	Unidentified Mineral	Chlorite
wt%	11MR1001(81.3m)-4	11MR1001(83.4m)-1	11MR1001(83.4m)-1
SiO2	1.54	63.46	24.50
TiO2	0.01	1.34	0.04
Al2O3	22.11	12.19	16.51
Cr2O3			
Fe2O3			
FeO	3.04	17.84	16.85
Mn2O3			
MnO	37.26	0.03	-0.02
MgO	0.31	0.16	0.15
CaO	0.06	0.01	0.05
Na2O	0.14	0.45	0.14
K2O	0.05	3.11	0.76
SO3	0.00	0.02	0.00
CoO	3.49	0.19	0.11
P2O5	0.05	0.01	0.73
Cu2O	0.11	-0.01	0.05
CO2	0.00		
H2O			
total wt%	68.17	98.78	59.88
oxy			
adapting Fe3+, Mn3+ and H2O	11MR1001(81.3m)-4	11MR1001(83.4m)-1	11MR1001(83.4m)-1
wt%			
SiO2			
TiO2			
Al2O3			
Cr2O3			
Fe2O3			
FeO			
Mn2O3			
MnO			
MgO			
CaO			
Na2O			
K2O			
H2O			
CO2			
CoO			
total wt%			
oxy			
mineral formulae (oxides)	11MR1001(81.3m)-4	11MR1001(83.4m)-1	11MR1001(83.4m)-1
Si			
Ti			
Al			
Cr			
Fe3+			
Fe2+			
Mn3+			
Mn2+			
Mg			
Ca			
Na			
K			
OH			
C			
Co			
cation sum			
ideal cations			
name	lithiophorite	Unidentified Mineral	Unidentified Chlorite

analyses	Unidentified Mineral	Mica	Unidentified Mineral
wt%	11MR1091(99.4m)_prof1	11MR1091(99.4m)_prof1	11MR1091(99.4m)_prof1
SiO2	49.62	49.91	67.46
TiO2	0.51	0.28	0.23
Al2O3	17.31	28.06	5.96
Cr2O3			
Fe2O3			
FeO	10.03	5.71	9.43
Mn2O3			
MnO	0.00	0.00	-0.01
MgO	0.06	0.14	0.02
CaO	0.07	0.13	0.04
Na2O	1.44	2.91	0.55
K2O	1.26	3.11	0.61
SO3	0.01	0.00	0.00
CoO	0.19	0.07	0.26
P2O5	0.07	0.01	0.04
Cu2O	0.00	0.01	0.00
CO2	0.00	0.00	0.00
H2O			
total wt%	80.58	90.35	84.58
oxy			
adapting Fe3+, Mn3+ and H2O	11MR1091(99.4m)_prof1	11MR1091(99.4m)_prof1	11MR1091(99.4m)_prof1
wt%			
SiO2			
TiO2			
Al2O3			
Cr2O3			
Fe2O3			
FeO			
Mn2O3			
MnO			
MgO			
CaO			
Na2O			
K2O			
H2O			
CO2			
CoO			
total wt%			
oxy			
mineral formulae (oxides)	11MR1091(99.4m)_prof1	11MR1091(99.4m)_prof1	11MR1091(99.4m)_prof1
Si		3.43	
Ti		0.01	
Al		2.27	
Cr		0.00	
Fe3+		0.00	
Fe2+		0.33	
Mn3+		0.00	
Mn2+		0.00	
Mg		0.01	
Ca		0.01	
Na		0.39	
K		0.27	
OH		2.29	
C			
Co			
cation sum	0.00	6.73	0.00
ideal cations		6.50	
name	Unidentified Mineral	illite	Unidentified Mineral

analyses	Chlorite	Identidied mineral	Mica
wt%	11MR1001(83.4m)-1	11MR1001(83.4m)-1	11MR1001(83.4m)-3
SiO2	25.77	70.63	39.12
TiO2	6.99	0.64	1.79
Al2O3	5.10	3.04	24.14
Cr2O3			
Fe2O3			
FeO	55.31	26.46	13.27
Mn2O3			
MnO	0.01	0.01	-0.01
MgO	0.07	0.03	0.24
CaO	0.02	0.01	0.05
Na2O	0.15	0.08	0.67
K2O	0.97	0.67	4.62
SO3	0.00	0.02	0.02
CoO	0.30	0.42	0.25
P2O5	0.06	0.00	0.20
Cu2O	0.03	0.01	0.02
CO2			
H2O			
total wt%	94.78	102.01	84.37
oxy			11.00
adapting Fe3+, Mn3+ and H2O	11MR1001(83.4m)-1	11MR1001(83.4m)-1	11MR1001(83.4m)-3
wt%			
SiO2			
TiO2			
Al2O3			
Cr2O3			
Fe2O3			
FeO			
Mn2O3			
MnO			
MgO			
CaO			
Na2O			
K2O			
H2O			
CO2			
CoO			
total wt%			
oxy			
mineral formulae (oxides)	11MR1001(83.4m)-1	11MR1001(83.4m)-1	11MR1001(83.4m)-3
Si			3.08
Ti			0.11
Al			2.24
Cr			0.00
Fe3+			0.00
Fe2+			0.87
Mn3+			0.00
Mn2+			0.00
Mg			0.03
Ca			0.00
Na			0.10
K			0.46
OH			2.62
C			
Co			
cation sum			6.89
ideal cations			7.00
name	Unidentified Chlorite	Unidentidied mineral	Muscovite

analyses	Mica	Identidied mineral	Mica
wt%	11MR1001(83.4m)-4	11MR1001(83.4m)-4	11MR1001(83.4m)-4
SiO2	48.06	65.03	48.47
TiO2	0.47	0.56	1.12
Al2O3	26.86	8.81	21.13
Cr2O3			
Fe2O3			
FeO	4.43	17.98	11.98
Mn2O3			
MnO	0.00	-0.03	0.01
MgO	0.29	0.08	0.20
CaO	0.04	0.07	0.05
Na2O	0.70	0.13	0.53
K2O	5.82	1.24	3.81
SO3	0.02	0.01	0.00
CoO	0.31	0.28	0.17
P2O5	0.05	0.14	0.26
Cu2O	-0.01	-0.01	0.00
CO2			
H2O			
total wt%	87.04	94.30	87.72
oxy			
adapting Fe3+, Mn3+ and H2O	11MR1001(83.4m)-4	11MR1001(83.4m)-4	11MR1001(83.4m)-4
wt%			
SiO2			
TiO2			
Al2O3			
Cr2O3			
Fe2O3			
FeO			
Mn2O3			
MnO			
MgO			
CaO			
Na2O			
K2O			
H2O			
CO2			
CoO			
total wt%			
oxy			
mineral formulae (oxides)	11MR1001(83.4m)-4	11MR1001(83.4m)-4	11MR1001(83.4m)-4
Si	3.44		3.55
Ti	0.03		0.06
Al	2.26		1.82
Cr	0.00		0.00
Fe3+	0.00		0.00
Fe2+	0.26		0.73
Mn3+	0.00		0.00
Mn2+	0.00		0.00
Mg	0.03		0.02
Ca	0.00		0.00
Na	0.10		0.07
K	0.53		0.36
OH	2.38		2.44
C			
Co			
cation sum	6.65		6.62
ideal cations	6.50		6.50
name	illite	Unidentified mineral	illite

analyses	Mica	Magnetite	Quartz
wt%	11MR1001(83.4m)-4	11MR1001(83.4m)-5	11MR1001(83.4m)-5
SiO2	46.58	1.68	100.92
TiO2	0.83	0.03	0.00
Al2O3	27.64	7.08	0.03
Cr2O3			
Fe2O3			
FeO	6.98	48.43	0.71
Mn2O3			
MnO	0.03	-0.04	-0.01
MgO	0.31	0.02	-0.01
CaO	0.04	0.06	0.01
Na2O	0.73	0.04	0.01
K2O	5.87	0.00	0.00
SO3	0.02	0.00	-0.02
CoO	-0.03	0.58	0.05
P2O5	0.10	2.60	-0.01
Cu2O	0.00	0.07	0.01
CO2		3.00	
H2O			
total wt%	89.11	60.56	101.68
oxy			
adapting Fe3+, Mn3+ and H2O			
wt%			
SiO2			
TiO2			
Al2O3			
Cr2O3			
Fe2O3			
FeO			
Mn2O3			
MnO			
MgO			
CaO			
Na2O			
K2O			
H2O			
CO2			
CoO			
total wt%			
oxy			
mineral formulae (oxides)	11MR1001(83.4m)-4	11MR1001(83.4m)-5	11MR1001(83.4m)-5
Si	3.32	0.06	
Ti	0.04	0.00	
Al	2.32	0.32	
Cr	0.00	0.00	
Fe3+	0.00	1.14	
Fe2+	0.42	0.39	
Mn3+	0.00	0.00	
Mn2+	0.00	0.00	
Mg	0.03	0.00	
Ca	0.00	0.00	
Na	0.10	0.00	
K	0.53	0.00	
OH	2.38	0.00	
C			
Co			
cation sum	6.78	1.92	0.00
ideal cations	6.50	3.00	2.00
name	illite	Magnetite	Quartz

analyses	Q+impurities	Mica	Mica
wt%	11MR1001(83.4m)-6	11MR1091(99.4m)_prof1	11MR1091(99.4m)_prof1
SiO2	85.02	62.30	54.43
TiO2	0.72	0.82	1.53
Al2O3	6.86	16.23	20.47
Cr2O3			
Fe2O3			
FeO	3.85	9.40	5.22
Mn2O3			
MnO	0.00	-0.01	0.00
MgO	0.14	0.08	0.10
CaO	0.03	0.10	0.12
Na2O	0.18	1.96	2.18
K2O	1.85	1.40	2.11
SO3	0.00	0.01	0.00
CoO	0.23	0.27	0.19
P2O5	0.02	0.04	0.03
Cu2O	0.01	-0.03	-0.02
CO2		0.00	0.00
H2O			
total wt%	98.91	92.59	86.35
oxy	2.00	12.00	12.00
adapting Fe3+, Mn3+ and H2O			
wt%			
SiO2			
TiO2			
Al2O3			
Cr2O3			
Fe2O3			
FeO			
Mn2O3			
MnO			
MgO			
CaO			
Na2O			
K2O			
H2O			
CO2			
CoO			
total wt%			
oxy			
mineral formulae (oxides)	11MR1001(83.4m)-6	11MR1091(99.4m)_prof1	11MR1091(99.4m)_prof1
Si		4.14	3.84
Ti		0.04	0.08
Al		1.27	1.70
Cr		0.00	0.00
Fe3+		0.00	0.00
Fe2+		0.52	0.31
Mn3+		0.00	0.00
Mn2+		0.00	0.00
Mg		0.01	0.01
Ca		0.01	0.01
Na		0.25	0.30
K		0.12	0.19
OH		2.22	2.12
C			
Co			
cation sum	0.00	6.37	6.43
ideal cations	2.00	6.00	6.50
name	Quartz +impurities	Fe-rich illite	Fe-rich illite

analyses	Mica	Mica	Mica
wt%	11MR1091(99.4m)_prof1	11MR1091(99.4m)_prof1	11MR1091(99.4m)_prof1
SiO2	52.26	50.41	45.53
TiO2	0.67	0.62	0.67
Al2O3	17.90	24.40	30.76
Cr2O3			
Fe2O3			
FeO	8.22	7.38	6.06
Mn2O3			
MnO	0.00	0.00	0.03
MgO	0.07	0.09	0.14
CaO	0.10	0.13	0.16
Na2O	1.75	2.55	3.41
K2O	1.42	2.46	3.15
SO3	-0.01	0.00	0.01
CoO	0.28	0.11	0.20
P2O5	0.04	0.03	0.02
Cu2O	0.02	0.00	0.01
CO2	0.00	0.00	0.00
H2O			
total wt%	82.72	88.17	90.18
oxy	12.00	12.00	11.00
adapting Fe3+, Mn3+ and H2O	11MR1091(99.4m)_prof1	11MR1091(99.4m)_prof1	11MR1091(99.4m)_prof1
wt%			
SiO2			
TiO2			
Al2O3			
Cr2O3			
Fe2O3			
FeO			
Mn2O3			
MnO			
MgO			
CaO			
Na2O			
K2O			
H2O			
CO2			
CoO			
total wt%			
oxy			
mineral formulae (oxides)	11MR1091(99.4m)_prof1	11MR1091(99.4m)_prof1	11MR1091(99.4m)_prof1
Si	3.89	3.56	3.19
Ti	0.04	0.03	0.04
Al	1.57	2.03	2.54
Cr	0.00	0.00	0.00
Fe3+	0.00	0.00	0.00
Fe2+	0.51	0.44	0.35
Mn3+	0.00	0.00	0.00
Mn2+	0.00	0.00	0.00
Mg	0.01	0.01	0.01
Ca	0.01	0.01	0.01
Na	0.25	0.35	0.46
K	0.13	0.22	0.28
OH	2.24	2.12	2.33
C			
Co			
cation sum	6.41	6.65	6.89
ideal cations	2.00	6.50	7.00
name	illite	illite	Al-illite-Hydromica

analyses	Chlorite	Mica	Unidentified Mineral
wt%	11MR1091(99.4m)_prof1	11MR1091(99.4m)_prof1	11MR1091(99.4m)_prof1
SiO2	22.31	43.44	46.74
TiO2	0.41	1.40	0.21
Al2O3	12.48	27.64	16.33
Cr2O3			
Fe2O3			
FeO	7.55	12.00	9.96
Mn2O3			
MnO	-0.01	0.01	-0.02
MgO	0.04	0.11	0.07
CaO	0.22	0.12	0.13
Na2O	0.42	3.04	1.26
K2O	0.54	2.74	1.38
SO3	0.01	0.02	0.02
CoO	0.14	-0.03	0.19
P2O5	0.52	0.02	0.16
Cu2O	0.02	0.01	0.01
CO2	0.00	0.00	0.00
H2O			
total wt%	44.64	90.53	76.45
oxy		11.00	
adapting Fe3+, Mn3+ and H2O	11MR1091(99.4m)_prof1	11MR1091(99.4m)_prof1	11MR1091(99.4m)_prof1
wt%			
SiO2			
TiO2			
Al2O3			
Cr2O3			
Fe2O3			
FeO			
Mn2O3			
MnO			
MgO			
CaO			
Na2O			
K2O			
H2O			
CO2			
CoO			
total wt%			
oxy			
mineral formulae (oxides)	11MR1091(99.4m)_prof1	11MR1091(99.4m)_prof1	11MR1091(99.4m)_prof1
Si		3.13	
Ti		0.08	
Al		2.34	
Cr		0.00	
Fe3+		0.00	
Fe2+		0.72	
Mn3+		0.00	
Mn2+		0.00	
Mg		0.01	
Ca		0.01	
Na		0.42	
K		0.25	
OH		2.40	
C			
Co			
cation sum	0.00	6.97	0.00
ideal cations		7.00	15.00
name		Myscovite	

analyses	Unidentified Mineral	Mica	Mica
wt%	11MR1091(99.4m)_prof1	11MR1091(99.4m)_prof1	11MR1091(99.4m)_prof1
SiO2	70.99	58.08	52.57
TiO2	2.14	0.08	0.11
Al2O3	6.62	21.95	24.06
Cr2O3			
Fe2O3			
FeO	16.24	5.93	4.96
Mn2O3			
MnO	-0.02	0.02	0.00
MgO	0.04	0.12	0.08
CaO	0.07	0.10	0.11
Na2O	0.77	2.05	1.98
K2O	0.55	2.20	1.37
SO3	-0.01	0.01	0.01
CoO	0.30	0.33	0.27
P2O5	0.02	0.03	0.02
Cu2O	-0.01	0.01	-0.03
CO2	0.00	0.00	0.00
H2O			
total wt%	97.71	90.91	85.50
oxy			
adapting Fe3+, Mn3+ and H2O	11MR1091(99.4m)_prof1	11MR1091(99.4m)_prof1	11MR1091(99.4m)_prof1
wt%			
SiO2			
TiO2			
Al2O3			
Cr2O3			
Fe2O3			
FeO			
Mn2O3			
MnO			
MgO			
CaO			
Na2O			
K2O			
H2O			
CO2			
CoO			
total wt%			
oxy	0.00	0.00	0.00
mineral formulae (oxides)	11MR1091(99.4m)_prof1	11MR1091(99.4m)_prof1	11MR1091(99.4m)_prof1
Si		3.86	3.71
Ti		0.00	0.01
Al		1.72	2.00
Cr		0.00	0.00
Fe3+		0.26	0.00
Fe2+		0.07	0.29
Mn3+		0.00	0.00
Mn2+		0.00	0.00
Mg		0.01	0.01
Ca		0.01	0.01
Na		0.26	0.27
K		0.19	0.12
OH		2.21	2.36
C			
Co			
cation sum	0.00	6.38	6.42
ideal cations	0.00	6.50	6.50
name	Unidentified Mineral	Illite	Illite

analyses	Quartz	Unidentified Mineral	Mica
wt%	11MR1091(99.4m)_prof1	11MR1091(99.4m)_prof1	11MR1091(99.4m)_prof1
SiO2	80.53	73.43	53.55
TiO2	4.45	0.13	0.98
Al2O3	6.86	14.28	24.81
Cr2O3			
Fe2O3			
FeO	3.69	3.12	5.59
Mn2O3			
MnO	0.00	0.00	0.01
MgO	0.05	0.04	0.08
CaO	0.03	0.06	0.11
Na2O	0.50	1.26	2.03
K2O	0.81	1.08	1.57
SO3	0.01	0.00	0.00
CoO	0.07	0.02	0.03
P2O5	0.04	0.02	0.02
Cu2O	-0.01	0.00	0.00
CO2	0.00	0.00	0.00
H2O			
total wt%	97.04	93.45	88.79
oxy	2.00		12.00
adapting Fe3+, Mn3+ and H2O	11MR1091(99.4m)_prof1	11MR1091(99.4m)_prof1	11MR1091(99.4m)_prof1
wt%			
SiO2			
TiO2			
Al2O3			
Cr2O3			
Fe2O3			
FeO			
Mn2O3			
MnO			
MgO			
CaO			
Na2O			
K2O			
H2O			
CO2			
CoO			
total wt%			
oxy			
mineral formulae (oxides)	11MR1091(99.4m)_prof1	11MR1091(99.4m)_prof1	11MR1091(99.4m)_prof1
Si			3.67
Ti			0.05
Al			2.00
Cr			0.00
Fe3+			0.00
Fe2+			0.32
Mn3+			0.00
Mn2+			0.00
Mg			0.01
Ca			0.01
Na			0.27
K			0.14
OH			2.29
C			
Co			
cation sum			6.47
ideal cations	1.00		6.50
name	Quartz with impurities	Unidentified Mineral	Fe-rich illite

analyses	Mica	Mica	Mica
wt%	11MR1091(99.4m)_prof1	11MR1091(99.4m)_prof1	11MR1091(99.4m)_prof1
SiO2	48.49	43.34	49.58
TiO2	0.26	1.28	0.88
Al2O3	24.71	22.92	25.81
Cr2O3			
Fe2O3			
FeO	7.53	18.92	9.21
Mn2O3			
MnO	0.01	0.02	0.00
MgO	0.10	0.09	0.11
CaO	0.14	0.10	0.15
Na2O	2.18	2.37	2.83
K2O	2.22	1.83	2.24
SO3	0.02	0.00	0.00
CoO	0.27	0.21	0.26
P2O5	0.08	0.11	0.07
Cu2O	0.02	0.01	0.04
CO2	0.00	0.00	0.00
H2O			
total wt%	86.05	91.19	91.17
oxy			
adapting Fe3+, Mn3+ and H2O			
wt%	11MR1091(99.4m)_prof1	11MR1091(99.4m)_prof1	11MR1091(99.4m)_prof1
SiO2			
TiO2			
Al2O3			
Cr2O3			
Fe2O3			
FeO			
Mn2O3			
MnO			
MgO			
CaO			
Na2O			
K2O			
H2O			
CO2			
CoO			
total wt%			
oxy			
mineral formulae (oxides)	11MR1091(99.4m)_prof1	11MR1091(99.4m)_prof1	11MR1091(99.4m)_prof1
Si	3.51	3.19	3.74
Ti	0.01	0.07	0.05
Al	2.11	1.99	2.29
Cr	0.00	0.00	0.00
Fe3+	0.00	0.00	0.00
Fe2+	0.45	1.16	0.58
Mn3+	0.00	0.00	0.00
Mn2+	0.00	0.00	0.00
Mg	0.01	0.01	0.01
Ca	0.01	0.01	0.01
Na	0.30	0.34	0.41
K	0.21	0.17	0.22
OH	2.41	2.45	2.51
C			
Co			
cation sum	6.61	6.94	7.31
ideal cations	6.50	7.00	7.00
name	illite	Muscovite	illite

analyses	Unidentified mineral	Unidentified mineral	Unidentified mineral
wt%	11MR1094(73.5m)1	11MR1094(73.5m)-FeO(1um)	11MR1094(73.5m)2
SiO2	19.61	37.19	0.65
TiO2	0.17	1.08	0.06
Al2O3	2.73	2.07	3.76
Cr2O3			
Fe2O3			
FeO	4.00	51.61	9.37
Mn2O3			
MnO	46.11	0.05	51.97
MgO	0.47	0.02	0.55
CaO	0.50	0.01	0.40
Na2O	0.14	0.03	0.11
K2O	1.04	0.22	0.54
SO3	0.02	0.02	0.04
CoO	0.66	0.21	0.65
P2O5	0.21	0.01	0.32
Cu2O	0.19	0.03	0.12
CO2	0.00	0.00	0.00
H2O			
total wt%	75.85	92.55	68.53
oxy			
adapting Fe3+, Mn3+ and H2O	11MR1094(73.5m)1	11MR1094(73.5m)-FeO(1um)	11MR1094(73.5m)2
wt%			
SiO2			
TiO2			
Al2O3			
Cr2O3			
Fe2O3			
FeO			
Mn2O3			
MnO			
MgO			
CaO			
Na2O			
K2O			
H2O			
CO2			
CoO			
total wt%			
oxy			
mineral formulae (oxides)	11MR1094(73.5m)1	11MR1094(73.5m)-FeO(1um)	11MR1094(73.5m)2
Si			
Ti			
Al			
Cr			
Fe3+			
Fe2+			
Mn3+			
Mn2+			
Mg			
Ca			
Na			
K			
OH			
C			
Co			
cation sum			
ideal cations			
name	Unidentified mineral	Unidentified mineral	Unidentified mineral

analyses	Unidentified mineral	Unidentified mineral	Unidentified mineral
wt%	11MR1094(73.5m)2	11MR1094(73.5m)2	11MR1094(73.5m)3
SiO2	18.68	2.36	4.15
TiO2	0.05	0.05	0.07
Al2O3	2.53	3.56	4.88
Cr2O3			
Fe2O3			
FeO	5.85	6.18	2.39
Mn2O3			
MnO	49.33	55.17	44.60
MgO	0.56	0.58	0.62
CaO	0.42	0.42	0.27
Na2O	0.08	0.05	0.05
K2O	0.59	0.80	1.33
SO3	0.00	0.01	0.00
CoO	0.82	0.91	0.41
P2O5	0.12	0.23	0.20
Cu2O	0.17	0.17	0.28
CO2	0.00	0.00	0.00
H2O			
total wt%	79.19	70.47	59.23
oxy			
adapting Fe3+, Mn3+ and H2O	11MR1094(73.5m)2	11MR1094(73.5m)2	11MR1094(73.5m)3
wt%			
SiO2			
TiO2			
Al2O3			
Cr2O3			
Fe2O3			
FeO			
Mn2O3			
MnO			
MgO			
CaO			
Na2O			
K2O			
H2O			
CO2			
CoO			
total wt%			
oxy			
mineral formulae (oxides)	0.00	0.00	0.00
Si			
Ti			
Al			
Cr			
Fe3+			
Fe2+			
Mn3+			
Mn2+			
Mg			
Ca			
Na			
K			
OH			
C			
Co			
cation sum			
ideal cations			
name	Unidentified mineral	Unidentified mineral	Unidentified mineral

analyses	Unidentified mineral	Unidentified mineral	Unidentified mineral
wt%	11MR1094(73.5m)3	11MR1094(73.5m)3	11MR1094(73.5m)3
SiO2	0.37	6.25	1.39
TiO2	0.06	0.03	0.04
Al2O3	3.88	2.76	2.65
Cr2O3			
Fe2O3			
FeO	2.55	1.93	2.94
Mn2O3			
MnO	46.00	59.05	39.48
MgO	0.64	0.90	0.38
CaO	0.36	0.91	0.21
Na2O	0.06	0.11	0.05
K2O	1.12	1.53	1.26
SO3	0.01	0.01	-0.01
CoO	0.72	0.68	0.44
P2O5	0.17	0.09	0.15
Cu2O	0.25	0.18	0.19
CO2	0.00	0.00	0.00
H2O			
total wt%	56.19	74.41	49.18
oxy			
adapting Fe3+, Mn3+ and H2O			
wt%			
SiO2			
TiO2			
Al2O3			
Cr2O3			
Fe2O3			
FeO			
Mn2O3			
MnO			
MgO			
CaO			
Na2O			
K2O			
H2O			
CO2			
CoO			
total wt%			
oxy			
mineral formulae (oxides)	11MR1094(73.5m)3	11MR1094(73.5m)3	11MR1094(73.5m)3
Si			
Ti			
Al			
Cr			
Fe3+			
Fe2+			
Mn3+			
Mn2+			
Mg			
Ca			
Na			
K			
OH			
C			
Co			
cation sum			
ideal cations			
name	Unidentified mineral	Unidentified mineral	Unidentified mineral

analyses	Unidentified mineral	Unidentified mineral	Unidentified mineral
wt%	11MR1094(73.5m)3	11MR1094(73.5m)3	11MR1094(73.5m)3zoom photo
SiO2	1.43	0.30	26.16
TiO2	0.05	0.04	0.05
Al2O3	2.59	4.71	1.71
Cr2O3			
Fe2O3			
FeO	3.03	2.84	3.37
Mn2O3			
MnO	40.40	41.18	33.36
MgO	0.35	0.67	0.33
CaO	0.22	0.36	0.25
Na2O	0.06	0.04	0.04
K2O	1.28	0.43	0.44
SO3	0.01	0.02	0.00
CoO	0.43	0.61	0.32
P2O5	0.10	0.22	0.23
Cu2O	0.20	0.25	0.14
CO2	0.00	0.00	0.00
H2O			
total wt%	50.15	51.67	66.40
oxy			
adapting Fe3+, Mn3+ and H2O	11MR1094(73.5m)3	11MR1094(73.5m)3	11MR1094(73.5m)3zoom photo
wt%			
SiO2			
TiO2			
Al2O3			
Cr2O3			
Fe2O3			
FeO			
Mn2O3			
MnO			
MgO			
CaO			
Na2O			
K2O			
H2O			
CO2			
CoO			
total wt%			
oxy			
mineral formulae (oxides)	11MR1094(73.5m)3	11MR1094(73.5m)3	11MR1094(73.5m)3zoom photo
Si			
Ti			
Al			
Cr			
Fe3+			
Fe2+			
Mn3+			
Mn2+			
Mg			
Ca			
Na			
K			
OH			
C			
Co			
cation sum			
ideal cations			
name	Unidentified mineral	Unidentified mineral	Unidentified mineral

analyses	Unidentified mineral	Unidentified mineral	Unidentified mineral
wt%	11MR1094(73.5m)3zoom photo	11MR1094(73.5m)3zoom photo	11MR1094(73.5m)4
SiO2	0.31	0.33	52.39
TiO2	0.04	0.04	0.72
Al2O3	5.55	2.40	1.34
Cr2O3			
Fe2O3			
FeO	3.62	3.86	40.37
Mn2O3			
MnO	43.93	49.22	1.29
MgO	0.53	0.69	0.02
CaO	0.16	0.42	0.01
Na2O	0.02	0.08	0.01
K2O	1.56	0.53	0.15
SO3	0.00	0.01	0.00
CoO	0.59	0.64	0.16
P2O5	0.18	0.18	0.00
Cu2O	0.14	0.22	0.01
CO2	0.00	0.00	0.00
H2O			
total wt%	56.62	58.62	96.47
oxy			
adapting Fe3+, Mn3+ and H2O	11MR1094(73.5m)3zoom photo	11MR1094(73.5m)3zoom photo	11MR1094(73.5m)4
wt%			
SiO2			
TiO2			
Al2O3			
Cr2O3			
Fe2O3			
FeO			
Mn2O3			
MnO			
MgO			
CaO			
Na2O			
K2O			
H2O			
CO2			
CoO			
total wt%			
oxy			
mineral formulae (oxides)	11MR1094(73.5m)3zoom photo	11MR1094(73.5m)3zoom photo	11MR1094(73.5m)4
Si			
Ti			
Al			
Cr			
Fe3+			
Fe2+			
Mn3+			
Mn2+			
Mg			
Ca			
Na			
K			
OH			
C			
Co			
cation sum			
ideal cations			
name	Unidentified mineral	Unidentified mineral	Unidentified mineral

analyses	Unidentified mineral	Unidentified mineral	Unidentified mineral
wt%	11MR1094(73.5m)4Fe-MnO	11MR1094(73.5m)4Fe-MnO	11MR1094(73.5m)4Fe-MnO
SiO2	54.80	17.97	27.60
TiO2	0.74	1.16	0.72
Al2O3	1.34	4.32	5.93
Cr2O3			
Fe2O3			
FeO	40.20	46.85	37.04
Mn2O3			
MnO	1.24	6.69	3.09
MgO	0.03	0.01	0.05
CaO	0.03	0.07	0.04
Na2O	0.06	0.04	0.05
K2O	0.15	0.18	0.18
SO3	-0.01	0.03	0.03
CoO	0.23	0.14	0.28
P2O5	0.02	0.19	0.02
Cu2O	0.01	0.04	0.00
CO2	0.00	0.00	0.00
H2O			
total wt%	98.83	77.70	75.04
oxy			
adapting Fe3+, Mn3+ and H2O	11MR1094(73.5m)4Fe-MnO	11MR1094(73.5m)4Fe-MnO	11MR1094(73.5m)4Fe-MnO
wt%			
SiO2			
TiO2			
Al2O3			
Cr2O3			
Fe2O3			
FeO			
Mn2O3			
MnO			
MgO			
CaO			
Na2O			
K2O			
H2O			
CO2			
CoO			
total wt%			
oxy			
mineral formulae (oxides)	11MR1094(73.5m)4Fe-MnO	11MR1094(73.5m)4Fe-MnO	11MR1094(73.5m)4Fe-MnO
Si			
Ti			
Al			
Cr			
Fe3+			
Fe2+			
Mn3+			
Mn2+			
Mg			
Ca			
Na			
K			
OH			
C			
Co			
cation sum			
ideal cations			
name	Unidentified mineral	Unidentified mineral	Unidentified mineral

analyses	Unidentified mineral	Unidentified mineral	Unidentified mineral
wt%	11MR1094(73.5m)4Fe-MnO	11MR1094(73.5m)4MnO	11MR1094(73.5m)4MnO
SiO2	26.91	90.43	76.04
TiO2	1.13	0.03	0.20
Al2O3	0.52	1.46	4.39
Cr2O3			
Fe2O3			
FeO	59.42	1.13	2.07
Mn2O3			
MnO	3.25	6.65	10.94
MgO	0.04	0.17	0.33
CaO	0.03	0.08	0.15
Na2O	0.01	0.07	0.16
K2O	0.00	0.34	0.74
SO3	-0.01	0.01	0.00
CoO	0.31	0.25	0.11
P2O5	0.00	0.01	0.04
Cu2O	0.05	0.02	0.00
CO2	0.00	0.00	0.00
H2O			
total wt%	91.67	100.65	95.17
oxy			
adapting Fe3+, Mn3+ and H2O	11MR1094(73.5m)4Fe-MnO	11MR1094(73.5m)4MnO	11MR1094(73.5m)4MnO
wt%			
SiO2			
TiO2			
Al2O3			
Cr2O3			
Fe2O3			
FeO			
Mn2O3			
MnO			
MgO			
CaO			
Na2O			
K2O			
H2O			
CO2			
CoO			
total wt%			
oxy			
mineral formulae (oxides)	11MR1094(73.5m)4Fe-MnO	11MR1094(73.5m)4MnO	11MR1094(73.5m)4MnO
Si			
Ti			
Al			
Cr			
Fe3+			
Fe2+			
Mn3+			
Mn2+			
Mg			
Ca			
Na			
K			
OH			
C			
Co			
cation sum			
ideal cations			
name	Unidentified mineral	Unidentified mineral	Unidentified mineral

analyses	Unidentified mineral	Unidentified mineral	Unidentified mineral
wt%	11MR1094(73.5m)4MnO	11MR1094(73.5m)4a	11MR1094(73.5m)4a
SiO2			
TiO2	50.85	57.96	53.60
Al2O3	0.34	0.55	0.41
Cr2O3	11.65	14.11	11.48
Fe2O3			
FeO			
Mn2O3	7.37	5.84	19.10
MnO			
MgO	7.72	5.94	0.17
CaO	0.06	0.12	0.10
Na2O	0.10	0.04	0.03
K2O	0.16	0.42	0.38
SO3	0.94	2.45	1.83
CoO	0.05	0.04	0.03
P2O5	0.34	0.31	0.15
Cu2O	0.12	0.13	0.33
CO2	0.01	0.00	0.02
H2O	0.00	0.00	0.00
total wt%			
oxy	79.70	87.92	87.63
adapting Fe3+, Mn3+ and H2O	11MR1094(73.5m)4MnO	11MR1094(73.5m)4a	11MR1094(73.5m)4a
wt%			
SiO2			
TiO2			
Al2O3			
Cr2O3			
Fe2O3			
FeO			
Mn2O3			
MnO			
MgO			
CaO			
Na2O			
K2O			
H2O			
CO2			
CoO			
total wt%			
oxy			
mineral formulae (oxides)	11MR1094(73.5m)4MnO	11MR1094(73.5m)4a	11MR1094(73.5m)4a
Si			
Ti			
Al			
Cr			
Fe3+			
Fe2+			
Mn3+			
Mn2+			
Mg			
Ca			
Na			
K			
OH			
C			
Co			
cation sum			
ideal cations			
name	Unidentified mineral	Unidentified mineral	Unidentified mineral

analyses	Unidentified mineral	Unidentified mineral	Unidentified mineral
wt%	11MR1094(73.5m)5	11MR1094(73.5m)5	11MR1094(73.5m)6MnSi
SiO2			
TiO2	19.54	56.46	6.20
Al2O3	0.33	0.69	0.06
Cr2O3	9.15	5.86	3.99
Fe2O3			
FeO			
Mn2O3	4.71	17.79	5.34
MnO			
MgO	35.49	1.00	53.40
CaO	0.73	0.07	0.92
Na2O	0.36	0.03	0.76
K2O	0.15	0.17	0.09
SO3	0.39	1.03	0.41
CoO	0.02	0.05	0.02
P2O5	0.48	0.10	0.66
Cu2O	0.07	0.37	0.12
CO2	0.11	0.00	0.16
H2O	0.00	0.00	0.00
total wt%			
oxy	71.53	83.62	72.10
adapting Fe3+, Mn3+ and H2O	11MR1094(73.5m)5	11MR1094(73.5m)5	11MR1094(73.5m)6MnSi
wt%			
SiO2			
TiO2			
Al2O3			
Cr2O3			
Fe2O3			
FeO			
Mn2O3			
MnO			
MgO			
CaO			
Na2O			
K2O			
H2O			
CO2			
CoO			
total wt%			
oxy			
mineral formulae (oxides)	11MR1094(73.5m)5	11MR1094(73.5m)5	11MR1094(73.5m)6MnSi
Si			
Ti			
Al			
Cr			
Fe3+			
Fe2+			
Mn3+			
Mn2+			
Mg			
Ca			
Na			
K			
OH			
C			
Co			
cation sum			
ideal cations			
name	Unidentified mineral	Unidentified mineral	Unidentified mineral

analyses	Unidentified mineral	Unidentified mineral	Unidentified mineral
wt%	11MR1094(73.5m)6MnSi	11MR1094(73.5m)7	11MR1094(73.5m)8
SiO2			
TiO2	43.89	10.09	33.24
Al2O3	0.16	0.02	0.17
Cr2O3	9.17	1.30	13.37
Fe2O3			
FeO			
Mn2O3	6.41	5.90	33.42
MnO			
MgO	15.80	20.44	0.32
CaO	0.20	0.27	0.15
Na2O	0.16	0.14	0.07
K2O	0.29	0.03	0.33
SO3	1.67	0.07	1.36
CoO	0.02	0.03	0.04
P2O5	0.41	0.26	0.13
Cu2O	0.11	0.10	0.64
CO2	0.05	0.12	0.02
H2O	0.00	0.00	0.00
total wt%			
oxy	78.33	38.77	83.27
adapting Fe3+, Mn3+ and H2O	11MR1094(73.5m)6MnSi	11MR1094(73.5m)7	11MR1094(73.5m)8
wt%			
SiO2			
TiO2			
Al2O3			
Cr2O3			
Fe2O3			
FeO			
Mn2O3			
MnO			
MgO			
CaO			
Na2O			
K2O			
H2O			
CO2			
CoO			
total wt%			
oxy			
mineral formulae (oxides)	11MR1094(73.5m)6MnSi	11MR1094(73.5m)7	11MR1094(73.5m)8
Si			
Ti			
Al			
Cr			
Fe3+			
Fe2+			
Mn3+			
Mn2+			
Mg			
Ca			
Na			
K			
OH			
C			
Co			
cation sum			
ideal cations			
name	Unidentified mineral	Unidentified mineral	Unidentified mineral

analyses	Unidentified mineral	Unidentified mineral	Unidentified mineral
wt%	11MR1094(73.5m)8	11MR1094(73.5m)9	11MR1094(73.5m)1-(1um)
SiO2			
TiO2	33.92	53.37	10.74
Al2O3	0.22	0.64	0.40
Cr2O3	15.70	13.38	2.14
Fe2O3			
FeO			
Mn2O3	30.90	17.09	5.82
MnO			
MgO	0.28	0.80	39.05
CaO	0.12	0.11	0.62
Na2O	0.06	0.08	0.55
K2O	0.34	0.29	0.06
SO3	1.88	1.68	0.18
CoO	0.05	0.02	0.03
P2O5	-0.03	0.19	0.76
Cu2O	0.63	0.26	1.24
CO2	0.03	0.07	0.15
H2O	0.00	0.00	0.00
total wt%			
oxy	84.11	87.96	61.75
adapting Fe3+, Mn3+ and H2O	11MR1094(73.5m)8	11MR1094(73.5m)9	11MR1094(73.5m)1-(1um)
wt%			
SiO2			
TiO2			
Al2O3			
Cr2O3			
Fe2O3			
FeO			
Mn2O3			
MnO			
MgO			
CaO			
Na2O			
K2O			
H2O			
CO2			
CoO			
total wt%			
oxy			
mineral formulae (oxides)	11MR1094(73.5m)8	11MR1094(73.5m)9	11MR1094(73.5m)1-(1um)
Si			
Ti			
Al			
Cr			
Fe3+			
Fe2+			
Mn3+			
Mn2+			
Mg			
Ca			
Na			
K			
OH			
C			
Co			
cation sum			
ideal cations			
name	Unidentified mineral	Unidentified mineral	Unidentified mineral

analyses	Mica	Mica	Mica
wt%	11MR1091(94m)_Mn-prof	11MR1091(94m)_Mn-prof	11MR1091(94m)_Mn-prof
SiO2	44.73	50.69	61.26
TiO2	0.08	0.41	0.78
Al2O3	33.40	17.15	18.00
Cr2O3			
Fe2O3			
FeO	2.30	4.45	3.23
Mn2O3			
MnO	0.07	0.53	1.31
MgO	0.63	0.13	0.21
CaO	0.04	0.04	0.05
Na2O	1.03	0.71	1.00
K2O	8.14	1.75	2.88
SO3	0.03	0.00	0.02
CoO	0.18	0.17	0.15
P2O5	0.00	0.00	-0.01
Cu2O	-0.01	-0.03	0.00
CO2	0.00	0.00	0.00
H2O			
total wt%	90.62	76.00	88.88
oxy	11.00	12.00	12.00
adapting Fe3+, Mn3+ and H2O	11MR1091(94m)_Mn-prof	11MR1091(94m)_Mn-prof	11MR1091(94m)_Mn-prof
wt%			
SiO2			
TiO2			
Al2O3			
Cr2O3			
Fe2O3			
FeO			
Mn2O3			
MnO			
MgO			
CaO			
Na2O			
K2O			
H2O			
CO2			
CoO			
total wt%			
oxy			
mineral formulae (oxides)	11MR1091(94m)_Mn-prof	11MR1091(94m)_Mn-prof	11MR1091(94m)_Mn-prof
Si	3.12	4.01	4.15
Ti	0.00	0.02	0.04
Al	2.75	1.60	1.44
Cr	0.00	0.00	0.00
Fe3+	0.00	0.00	0.00
Fe2+	0.13	0.29	0.18
Mn3+	0.00	0.00	0.00
Mn2+	0.00	0.04	0.08
Mg	0.07	0.02	0.02
Ca	0.00	0.00	0.00
Na	0.14	0.11	0.13
K	0.72	0.18	0.25
OH	2.33	2.33	2.26
C			
Co			
cation sum	6.94	6.27	6.28
ideal cations	7.00	6.50	7.00
name	Muscovite	illite	illite

analyses	Mica	Unidentified mineral	Unidentified Chlorite
wt%	11MR1091(94m)_Mn-prof	11MR1091(94m)_Mn-prof	11MR1091(94m)_Mn-prof
SiO2	45.20	34.75	28.29
TiO2	0.06	0.35	0.15
Al2O3	27.06	14.82	25.04
Cr2O3			
Fe2O3			
FeO	2.20	2.86	3.24
Mn2O3			
MnO	9.32	27.93	20.74
MgO	0.56	0.68	0.49
CaO	0.13	0.20	0.13
Na2O	1.59	0.97	1.84
K2O	5.71	2.45	3.91
SO3	0.01	0.02	0.01
CoO	0.27	0.96	0.98
P2O5	-0.01	0.01	0.07
Cu2O	0.05	0.08	0.05
CO2	0.00	0.00	0.00
H2O			
total wt%	92.16	86.09	84.94
oxy	11MR1091(94m)_Mn-prof	11MR1091(94m)_Mn-prof	11MR1091(94m)_Mn-prof
adapting Fe3+, Mn3+ and H2O			
wt%			
SiO2			
TiO2			
Al2O3			
Cr2O3			
Fe2O3			
FeO			
Mn2O3			
MnO			
MgO			
CaO			
Na2O			
K2O			
H2O			
CO2			
CoO			
total wt%			
oxy			
mineral formulae (oxides)	11MR1091(94m)_Mn-prof	11MR1091(94m)_Mn-prof	11MR1091(94m)_Mn-prof
Si	3.21		
Ti	0.00		
Al	2.26		
Cr	0.00		
Fe3+	0.00		
Fe2+	0.13		
Mn3+	0.00		
Mn2+	0.56		
Mg	0.06		
Ca	0.01		
Na	0.22		
K	0.52		
OH	2.37		
C			
Co			
cation sum	6.97		
ideal cations	7.00		
name	Muscovite	Unidentified mineral	Unidentified Chlorite

analyses	Unidentified mineral	Unidentified mineral	Unidentified mineral
wt%	11MR1091(94m)_Mn-prof	11MR1091(94m)_Mn-prof	11MR1091(94m)_Mn-prof
SiO2	19.37	6.17	21.81
TiO2	0.13	0.21	0.33
Al2O3	17.21	5.68	10.45
Cr2O3			
Fe2O3			
FeO	4.12	4.62	3.94
Mn2O3			
MnO	36.83	53.67	40.32
MgO	0.69	0.51	0.41
CaO	0.17	0.17	0.16
Na2O	0.93	0.29	0.76
K2O	3.62	1.36	2.22
SO3	0.02	-0.01	-0.03
CoO	1.38	0.74	0.79
P2O5	0.08	0.22	0.23
Cu2O	0.13	0.08	0.07
CO2	0.00	0.00	0.00
H2O			
total wt%	84.68	73.70	81.47
oxy			
adapting Fe3+, Mn3+ and H2O	11MR1091(94m)_Mn-prof	11MR1091(94m)_Mn-prof	11MR1091(94m)_Mn-prof
wt%			
SiO2			
TiO2			
Al2O3			
Cr2O3			
Fe2O3			
FeO			
Mn2O3			
MnO			
MgO			
CaO			
Na2O			
K2O			
H2O			
CO2			
CoO			
total wt%			
oxy			
mineral formulae (oxides)	11MR1091(94m)_Mn-prof	11MR1091(94m)_Mn-prof	11MR1091(94m)_Mn-prof
Si			
Ti			
Al			
Cr			
Fe3+			
Fe2+			
Mn3+			
Mn2+			
Mg			
Ca			
Na			
K			
OH			
C			
Co			
cation sum			
ideal cations			
name	Unidentified mineral	Unidentified mineral	Unidentified mineral

analyses	Unidentified mineral	Unidentified mineral	Unidentified mineral
wt%	11MR1091(94m)_Mn-prof	11MR1091(94m)_Mn-prof	11MR1091(94m)_Mn-prof
SiO2	29.67	42.36	15.55
TiO2	0.31	0.47	0.37
Al2O3	13.17	10.52	11.25
Cr2O3			
Fe2O3			
FeO	2.58	3.11	2.86
Mn2O3			
MnO	33.82	29.03	45.15
MgO	0.83	0.55	0.63
CaO	0.27	0.24	0.28
Na2O	0.86	0.77	0.68
K2O	2.56	1.88	2.50
SO3	0.04	-0.01	0.01
CoO	0.80	0.57	0.78
P2O5	0.11	0.12	0.32
Cu2O	0.10	0.08	0.07
CO2	0.00	0.00	0.00
H2O			
total wt%	85.13	89.68	80.45
oxy			
adapting Fe3+, Mn3+ and H2O	11MR1091(94m)_Mn-prof	11MR1091(94m)_Mn-prof	11MR1091(94m)_Mn-prof
wt%			
SiO2			
TiO2			
Al2O3			
Cr2O3			
Fe2O3			
FeO			
Mn2O3			
MnO			
MgO			
CaO			
Na2O			
K2O			
H2O			
CO2			
CoO			
total wt%			
oxy			
mineral formulae (oxides)	11MR1091(94m)_Mn-prof	11MR1091(94m)_Mn-prof	11MR1091(94m)_Mn-prof
Si			
Ti			
Al			
Cr			
Fe3+			
Fe2+			
Mn3+			
Mn2+			
Mg			
Ca			
Na			
K			
OH			
C			
Co			
cation sum			
ideal cations			
name	Unidentified mineral	Unidentified mineral	Unidentified mineral

analyses	Unidentified mineral	Unidentified mineral	Unidentified mineral
wt%	11MR1091(94m)_Mn-prof	11MR1091(94m)_Mn-prof	11MR1091(94m)_Mn-prof
SiO2	58.74	18.80	68.22
TiO2	0.20	0.32	0.11
Al2O3	3.94	10.14	4.71
Cr2O3			
Fe2O3			
FeO	1.80	2.76	1.15
Mn2O3			
MnO	25.10	43.12	18.42
MgO	0.29	0.61	0.20
CaO	0.12	0.18	0.05
Na2O	0.25	0.78	0.22
K2O	0.97	2.38	1.08
SO3	0.00	-0.01	0.00
CoO	0.44	0.77	0.53
P2O5	0.09	0.15	0.02
Cu2O	0.03	0.08	0.01
CO2	0.00	0.00	0.00
H2O			
total wt%	91.96	80.10	94.72
oxy			
adapting Fe3+, Mn3+ and H2O	11MR1091(94m)_Mn-prof	11MR1091(94m)_Mn-prof	11MR1091(94m)_Mn-prof
wt%			
SiO2			
TiO2			
Al2O3			
Cr2O3			
Fe2O3			
FeO			
Mn2O3			
MnO			
MgO			
CaO			
Na2O			
K2O			
H2O			
CO2			
CoO			
total wt%			
oxy			
mineral formulae (oxides)	11MR1091(94m)_Mn-prof	11MR1091(94m)_Mn-prof	11MR1091(94m)_Mn-prof
Si			
Ti			
Al			
Cr			
Fe3+			
Fe2+			
Mn3+			
Mn2+			
Mg			
Ca			
Na			
K			
OH			
C			
Co			
cation sum			
ideal cations			
name	Unidentified mineral	Unidentified mineral	Unidentified mineral

analyses	Unidentified mineral	Unidentified mineral	Unidentified mineral
wt%	11MR1091(94m)_Mn-prof	11MR1091(94m)_Mn-prof	11MR1091(94m)_Mn-prof
SiO2	59.01	46.14	69.09
TiO2	0.17	0.70	0.12
Al2O3	9.45	8.26	6.94
Cr2O3			
Fe2O3			
FeO	3.38	7.91	6.39
Mn2O3			
MnO	15.54	24.78	11.44
MgO	0.28	0.54	0.23
CaO	0.11	0.14	0.06
Na2O	0.64	0.40	0.50
K2O	1.49	0.95	1.26
SO3	-0.01	0.01	0.00
CoO	0.97	1.52	0.66
P2O5	0.01	0.00	0.01
Cu2O	0.07	0.12	0.10
CO2	0.00	0.00	0.00
H2O			
total wt%	91.12	91.48	96.78
oxy			
adapting Fe3+, Mn3+ and H2O	11MR1091(94m)_Mn-prof	11MR1091(94m)_Mn-prof	11MR1091(94m)_Mn-prof
wt%			
SiO2			
TiO2			
Al2O3			
Cr2O3			
Fe2O3			
FeO			
Mn2O3			
MnO			
MgO			
CaO			
Na2O			
K2O			
H2O			
CO2			
CoO			
total wt%			
oxy			
mineral formulae (oxides)	11MR1091(94m)_Mn-prof	11MR1091(94m)_Mn-prof	11MR1091(94m)_Mn-prof
Si			
Ti			
Al			
Cr			
Fe3+			
Fe2+			
Mn3+			
Mn2+			
Mg			
Ca			
Na			
K			
OH			
C			
Co			
cation sum			
ideal cations			
name	Unidentified mineral	Unidentified mineral	Unidentified mineral

analyses	Unidentified mineral	Unidentified mineral	
wt%	11MR1091(94m)_Mn-prof	11MR1091(94m)_Mn-prof	
SiO2	57.80	70.10	
TiO2	0.24	0.24	
Al2O3	16.33	11.67	
Cr2O3			
Fe2O3			
FeO	4.56	4.02	
Mn2O3			
MnO	0.38	0.15	
MgO	0.16	0.11	
CaO	0.03	0.04	
Na2O	0.92	0.92	
K2O	2.54	1.62	
SO3	0.00	-0.01	
CoO	0.21	0.34	
P2O5	-0.05	-0.01	
Cu2O	0.02	0.00	
CO2	0.00	0.00	
H2O			
total wt%	83.15	89.19	
oxy			
adapting Fe3+, Mn3+ and H2O	11MR1091(94m)_Mn-prof	11MR1091(94m)_Mn-prof	
wt%			
SiO2			
TiO2			
Al2O3			
Cr2O3			
Fe2O3			
FeO			
Mn2O3			
MnO			
MgO			
CaO			
Na2O			
K2O			
H2O			
CO2			
CoO			
total wt%			
oxy			
mineral formulae (oxides)	11MR1091(94m)_Mn-prof	11MR1091(94m)_Mn-prof	
Si	4.18		
Ti	0.01		
Al	1.39		
Cr	0.00		
Fe3+	0.00		
Fe2+	0.28		
Mn3+	0.00		
Mn2+	0.02		
Mg	0.02		
Ca	0.00		
Na	0.13		
K	0.23		
OH	2.41		
C			
Co			
cation sum	6.03		
ideal cations	6.40		
name	illite	Unidentified mineral	

	Average Muscovite	Average Al-illite Hydromica	Average Illite
analyses	43.76	46.31	52.32
wt%	0.68	0.38	0.69
SiO2	28.97	27.25	22.32
TiO2			
Al2O3			
Cr2O3	7.64	6.80	6.62
Fe2O3			
FeO	2.20	0.02	0.16
Mn2O3	0.31	0.23	0.16
MnO	0.09	0.07	0.08
MgO	2.04	1.53	1.52
CaO	4.82	4.77	2.94
Na2O	0.01	0.01	0.01
K2O	0.18	0.24	0.20
SO3	0.06	0.14	0.05
CoO	0.01	0.00	0.00
P2O5	0.00	0.00	0.00
Cu2O			
CO2	90.75	87.74	87.07
H2O	11.00	11.00	12.00
total wt%			
oxy			
adapting Fe3+, Mn3+ and H2O			
wt%			
SiO2			
TiO2			
Al2O3			
Cr2O3			
Fe2O3			
FeO			
Mn2O3			
MnO			
MgO			
CaO			
Na2O			
K2O			
H2O			
CO2			
CoO			
total wt%			
oxy			
mineral formulae (oxides)			
Si	3.12	3.34	3.76
Ti	0.04	0.02	0.04
Al	2.43	2.31	1.89
Cr			
Fe3+			
Fe2+	0.47	0.41	0.38
Mn3+			
Mn2+	0.11		0.01
Mg	0.03	0.03	0.02
Ca	0.01	0.01	0.01
Na	0.28	0.21	0.21
K	0.44	0.44	0.27
OH	2.36	2.40	2.46
C			
Co			
cation sum	6.94	6.76	6.58
ideal cations	7.00	7.00	6.28

	Average Cryptomelane		
analyses			
wt%			
SiO2	0.08		
TiO2	0.01		
Al2O3	0.65		
Cr2O3			
Fe2O3			
FeO	0.96		
Mn2O3			
MnO	72.36		
MgO	0.06		
CaO	0.29		
Na2O	0.64		
K2O	2.24		
SO3	0.00		
CoO	0.45		
P2O5	0.51		
Cu2O	0.02		
CO2			
H2O			
total wt%	78.27		
oxy	16.00		
adapting Fe3+, Mn3+ and H2O			
wt%			
SiO2	0.08		
TiO2	0.01		
Al2O3	0.64		
Cr2O3			
Fe2O3	0.17		
FeO	0.19		
Mn2O3	76.49		
MnO	6.46		
MgO	0.07		
CaO	0.29		
Na2O	0.66		
K2O	2.27		
H2O	-0.01		
CO2			
CoO			
total wt%	87.33		
oxy	16.00		
mineral formulae (oxides)			
Si	0.01		
Ti	0.00		
Al	0.13		
Cr			
Fe3+	0.01		
Fe2+	0.16		
Mn3+	9.66		
Mn2+	0.88		
Mg	0.01		
Ca	0.05		
Na	0.21		
K	0.49		
OH	0.00		
C			
Co			
cation sum	11.24		
ideal cations	6.33	9.00	

Average Formulas	
Muscovite	$(K_{0.44},Na_{0.28})(Al_2)(Si_{3.12}Al_{0.43})(O_{10})(OH)_2$
All-illite Hydromica	$(K_{0.44}Na_{0.21})(Al_{2.31}Si_{3.34}Fe^{2+}{}_{0.41})O_{10}(OH)_{2.5}$
Illite	$(K_{0.15}Na_{0.27})(Al_{1.66}Si_{3.88}Fe^{2+}{}_{0.38})O_{10}(OH)_2$
Crytptomelane	$(K_{0.49},Na_{0.21})(Mn_7{}^{4+},Mn^{2+}{}_{0.88}Al_{0.13},Fe^{2+}{}_{0.16},Fe^{3+}{}_{0.01},Mg_{0.01})O_{16}(OH)_{14}$